Methods for the Investigation of Transonic Buffet

Thesis submitted in accordance with the requirements of
the University of Liverpool for the degree of Doctor in Philosophy
by

Panagiotis Belesiotis (BEng (Hons), MSc (University of Liverpool))

November 2022

Abstract

Transonic buffet is an unsteady shock-wave/boundary-layer interaction phenomenon, encountered in large civil or military aircraft at edge-of-the-envelope conditions. The interaction of the unsteady aerodynamic loads with the elastic wing structure can pose a risk of structural failure and thus the absence of any structural vibration or buffeting at cruise conditions is a certification requirement by regulatory authorities. A thorough understanding of the mechanisms that govern the phenomenon is of paramount importance in order to face the engineering challenges that are associated with designing future wings that push the limits of the flight envelope. This present work aims to address the interaction of the phenomenon with wing vibration and to investigate the effect of transient growth on aerofoil transonic buffet. This is achieved by performing three different but related studies. The first one focuses on harmonically exciting the flow at steady and unsteady conditions. It is found that in contrast to aerofoil shock-buffet, that demonstrates full synchronisation to the excitation for certain combinations of excitation frequency and amplitude, the harmonic excitation of the wing only affects the high-frequency behaviour of the phenomenon associated with a global mode, while the low frequency behaviour remains unaffected. For the second study, a coupled fluid-structure simulation was carried out at unsteady conditions. This revealed that, while the initial linear structural response depends on the buffet frequency for all modes, this only holds for structural modes with natural frequencies close to that of buffet in the nonlinear part of the response. A dependence on their respective wind-off structural frequency and the first bending mode is found for lower frequency structural modes in the nonlinear part of the response. For the last study, transient growth analysis is applied at a supercritical aerofoil in steady and unsteady conditions. To the best of the author's knowledge, this is the first transient growth study on an aerofoil in transonic flow subject to shock buffet. Modest growth of optimal initial perturbations is observed. A quartic dependence of the maximum energy attained on the angle of attack is found for pre-onset conditions. These findings will help advance the understanding of the underlying physics of transonic buffet and ultimately inform future wing design.

Acknowledgements

This work is dedicated to everyone that has supported me throughout this journey, directly or indirectly, near or far.

Firstly, I would like to thank my academic supervisor Dr. Sebastian Timme and my industrial supervisor Murray Cross for providing me with this opportunity. Their guidance, ideas, patience and knowledge were of utmost importance to this work and are truly appreciated. I particularly wish to thank Dr. Sebastian Timme for encouraging me to keep on pushing and strive for perfection.

I would like to express my sincere gratitude to Prof. Vassilis Theofilis for inspiring me to dive into the exotic world of fluid mechanics and for his continuous mentorship. Our fruitful discussions were always key to my research and my personal development.

I would also like to take this opportunity to thank my examiners, Prof. Vassilis Theofilis and Prof. Dorian Jones for stimulating and pleasant VIVA.

On a personal level I would like to thank:

My mother, Betty Belesioti, my grandma, Mary Belesioti, my uncle, Kostas Belesiotis and my girlfriend Elena Karakashevska for always believing in me. Your continuous unconditional love and support made all this possible. I hope I made you all proud.

All my friends and colleagues in the office at the University. In special, Dr. Helio Quintanilha Jr, who I met first in my PhD, for being a great friend and for his knowledge and suggestions in the transient growth work. Dr. Nicolas Cerulus, Dr. Luke Masini and Suyash Sharma for making the workplace a pleasant space to conduct research. In particular I would like to thank Suyash Sharma for encouraging me to work on GPU parallel programming.

Dr. Ahmed Makarem, Dr. Ali Aboulatta and Dr. Francis Baumont De Oliveira for their comradery from our undergraduate to the PhD years.

My friends from Greece and the U.K. for always being there for me. In special I would like to thank Stathis Pantazis for providing me with useful insight in programming challenges.

M & S for supplying snacks that fuel research.

This project was funded by Airbus.

Declaration

I confirm that the thesis is my own work, that I have not presented anyone else's work as my own and that full and appropriate acknowledgement has been given where reference has been made to the work of others.

Panagiotis Belesiotis
November 2022

List of Publications

Conferences

- Belesiotis-Kataras, P., Timme, S., "Aeroelastic Coupling Effects in Globally Unstable Transonic Wing Flow," Presented at the AIAA Scitech 2021 Virtual Event, 2021. https://doi.org/10.2514/6.2021-0611

- Belesiotis-Kataras, P., Timme, S., "Harmonic Forcing Amplitude Effects in Globally Unstable Transonic Wing Flow," Presented at the AIAA Scitech 2020 Forum, Orlando FL, 2020. https://doi.org/10.2514/6.2020-1985

- De Aguiar Quintanilha Junior, H. R., Belesiotis-Kataras, P., Theofilis, V., Hanifi, A.,"Nonmodal stability analysis of the HIFiRE-5 elliptic cone model flow in different flight altitudes," Presented at the 58th IACAS, Tel-Aviv & Haifa, Israel, 2018.

- Belesiotis-Kataras, P., Timme, S., "Numerical Study of Incipient Transonic Shock Buffet on Large Civil Aircraft Wings," Presented at the RAeS Applied Aerodynamics Conference 2018, Bristol, United Kindom, 2018.

In Preparation

- Belesiotis, P., Timme, S. , De Aguiar Quintanilha Junior, H. R., Theofilis, V., "Transient Growth Analysis of Transonic Flow over Aerofoils," .

Table of Contents

List of Figures

List of Tables

List of Symbols

A	=	Jacobian matrix
a	=	speed of sound
$\boldsymbol{b}$	=	harmonic excitation vector
$\mathcal{C}$	=	damping matrix
$\mathcal{C}$	=	shifted matrix
C_D	=	drag coefficient
C_f	=	skin friction coefficient
C_L	=	lift coefficient
C_m	=	pitching moment coefficient
C_P	=	pressure coefficient
c_p, c_v	=	coefficients of specific heat at constant pressure and volume
$\mathcal{D}$	=	unitary eigenvector matrix
e	=	internal energy
E	=	total energy
$\mathcal{F}$	=	Cholesky factor
F_c, F_v	=	convective and viscous fluxes
f	=	frequency ($= 1/T$)
$\boldsymbol{f}_a$	=	vector of aerodynamic forces
f_{v1}	=	near wall damping function in Spalart–Allmaras turbulence model
G	=	energy gain
H	=	total enthalpy
H	=	Hessenberg matrix
h	=	specific enthalpy
I	=	identity matrix
i	=	imaginary unit ($= \sqrt{-1}$)

J	=	fluid Jacobian matrix ($= \partial \boldsymbol{R}_f / \partial \boldsymbol{q}$)
K	=	stiffness matrix
K_t	=	turbulent kinetic energy
$\mathcal{K}$	=	modal stiffness matrix
$\mathcal{L}$	=	linear operator
l_{ref}	=	reference length
M	=	mass matrix
M_∞	=	freestream Mach number
$\mathcal{M}$	=	modal mass matrix
$\boldsymbol{n}$	=	unit normal vector
P	=	pressure
Pr	=	Prandtl number
Q	=	Arnoldi decomposition matrix
q	=	heat flux
$\boldsymbol{q}$	=	vector of aerodynamic variables
$\boldsymbol{q}, \dot{\boldsymbol{q}}$	=	vectors of unknowns and corresponding temporal derivatives
$\boldsymbol{q}_0$	=	amplitude of forced sinusoidal motion
$\boldsymbol{R}$	=	residual vector
R	=	universal gas constant
$\mathcal{R}$	=	Ritz eigenvalues matrix
Re	=	chord Reynolds number
S	=	strain-rate tensor
St	=	Strouhal number
$\mathcal{S}$	=	shear tensor
T	=	temperature
t	=	time
$\boldsymbol{u}$	=	vector of Cartesian velocity components
V	=	volume matrix
$\boldsymbol{x}$, $\dot{\boldsymbol{x}}$	=	vectors of grid location and velocity
y^+	=	dimensionless wall distance

Greek Symbols

α	=	freestream angle of attack
γ	=	ratio of specific heats
δ	=	Kronecker delta
δ^*	=	boundary layer displacement thickness
$\dot{\boldsymbol{\epsilon}}$	=	rate of deformation (strain–rate) tensor
ϵ	=	increment
ζ	=	eigenvalue shift
ζ	=	structural damping ratio
η	=	nondimensional wing span
$\boldsymbol{\eta}$, $\dot{\boldsymbol{\eta}}$	=	vectors of generalised coordinates and velocities
κ	=	thermal conductivity
Λ	=	diagonal eigenvalue matrix
$\boldsymbol{\lambda}$	=	second viscosity
λ	=	eigenvalue
μ, μ_t	=	dynamic viscosity and turbulent (eddy) viscosity
μ	=	independent/bifurcation parameter
$\widetilde{\nu}$	=	intermediate variable of Spalart–Allmaras turbulence model
ρ	=	density
σ	=	real part of eigenvalue (growth rate)
τ	=	stress tensor
Φ	=	source term
ξ	=	normal mode
Ξ	=	matrix of mode shapes
Ψ	=	propagator operator
Ω	=	control volume
ω	=	imaginary part of eigenvalue (frequency)
ω^*	=	reduced frequency and eigenvalue's imaginary part

Subscripts

E	=	energy norm
f	=	fluid
i, j	=	Cartesian coordinates
l	=	laminar
max	=	maximum
s	=	structural
OIC	=	optimal initial condition
ORE	=	optimal response
ref	=	reference value
t	=	turbulent
∞	=	freestream value
0	=	mean value or initial value
2	=	Euclidean norm

Acronyms

AR	=	Aspect Ratio
ARA	=	Aircraft Research Association
BUCOLIC	=	BUffet COntroL of transonIC Wings
ARPACK	=	ARnoldi PACKage
CFL	=	Courant–Friedrichs–Lewy number
CFD	=	Computational Fluid Dynamics
CMM	=	Coordinate Measurement Machine
CPU	=	Central Processing Unit
CRM	=	Common Research Model
DDES	=	Delayed Detached Eddy Simulation
DES	=	Detached Eddy Simulation
DLR	=	German Aerospace Center
		(Deutsches Zentrum für Luft- und Raumfahrt)
DNS	=	Direct Numerical Simulation
DPW	=	Drag Prediction Workshop
EAS	=	equivalent airspeed
ESDU	=	Engineering Sciences Data Unit
ETW	=	European Transonic Windtunnel
EVP	=	eigenvalue problem
FEM	=	Finite Element Model
FS	=	FlowSimulator
FSI	=	Fluid Structure Interaction
IRAM	=	Implicitly Restarted Arnoldi Method
IVP	=	initial value problem
LCO	=	limit–cycle oscillation
LES	=	Large Eddy Simulation
LFD	=	Linearised Frequency-Domain
MAC	=	mean aerodynamic chord
NASA	=	National Aeronautics and Space Administration
NS	=	Navier–Stokes
NTF	=	National Transonic Facility

ONERA	=	French National Aerospace Centre
		(Office National d'É et de Recherches Aérospatiales)
RANS	=	Reynolds–averaged Navier–Stokes
RMS	=	Root-Mean Square
PPF	=	Plane Poiseuille flow
PSD	=	Power Spectral Density
ROM	=	Reduced-Order Model
SA	=	Spalart–Allmaras
SWBLI	=	Shock Wave Boundary Layer Interaction
STD	=	standard deviation
SVD	=	Singular Value Decomposition
TS	=	Tollmien–Schlichting
TWT	=	Transonic Wind Tunnel
URANS	=	Unsteady Reynolds–averaged Navier–Stokes
ZDES	=	Zonal Detached Eddy Simulation

Chapter 1

Introduction

1.1 Background

In recent years, technological strides have solidified the use of computational tools in the design phase of an aircraft. More specifically, advancements in the ability of Computational Fluid Dynamics (CFD) tools to deal with complex geometries in high-speed flows have significantly decreased the time and funds spent during the development of new aircraft, allowing extensive analysis of new designs before the prototyping and wind tunnel testing phase. Reynolds–averaged Navier–Stokes (RANS) simulations have been the main industry workhorse producing robust results with acceptable accuracy for typical operational conditions [2]. Depending on their role, all aircraft operate within certain limits that define the maximum or minimum airspeeds and altitudes for steady, level and unaccelerated flight as shown in figure 1.1. The area defined by those boundaries is called the operational flight envelope and the achievable airspeed range for each altitude, referred to as the flight corridor [1]. The minimum airspeed and maximum service ceiling are defined by stall speed and cabin pressurisation limits, respectively, although the maximum airspeed part of the envelope is limited by different factors that depend on the type of the aircraft. While the doghouse plot of figure 1.1 showcases the boundaries at each altitude, the flight envelope in figure 1.2 showcases the constraints posed by structural limits. The envelope formed by plotting the load factor n (lift to weight ratio) against the equivalent airspeed (EAS) of an aircraft is commonly referred to as V-n diagram and it marks the structural limits for each flight corridor, that the airplane has been designed to operate within [17]. In a typical commercial flight, the aircraft will generally go through the phases of take-off, climb,cruise, descent, approach and landing. For example, in phases that involve the deployment of high-lift devices (flaps) at low EAS (e.g. take-off and landing), the operating limits for the maximum

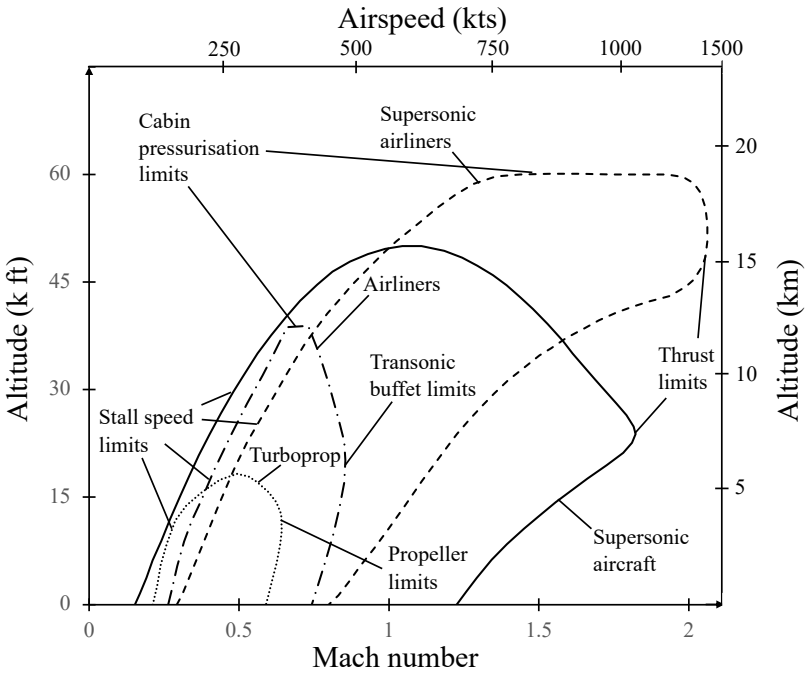

FIGURE 1.1. Operational flight envelopes for different aircraft types showing achievable airspeeds and altitudes, along with limiting factors. Adapted from [1].

supported load factor are found on the left of the envelope. In addition, as shown for a representative transport aircraft in figure 1.2, distinct complex flow physics that hinder the accuracy of simulations are encountered at these different phases and consequently at different parts of the flight envelope. To ensure maximum aerodynamic safety and efficiency, the cruise point and in general the normal operational range of the aircraft is kept away from these extreme conditions. A case of special interest is found at the high-speed and high-load part of the envelope, where the unsteady separated flow dynamics become progressively more complex as the Mach number increases. Seen from the point of view of a wing, as the cruise speed is increased to transonic conditions, the accelerated body of air on the suction side creates a local supersonic area, characterised by the standing shockwave located closer to the trailing edge, marking the end of that region. The existence of a shockwave, close to the thin boundary layer, formed by the no-slip condition at the wing surface, gives rise to a phenomenon referred to as shock-wave/boundary-layer interaction (SWBLI) and is a critical factor in aircraft performance [18, 19]. The stagnation pressure losses across the shock, the drag contributions of which are termed as *wave drag*, compound with the existing viscous drag. Moreover, the adverse pressure gradient introduced by the localised pressure increase at the shock, thickens the boundary layer therefore making it even more sensitive to pressure changes. Transonic interactions are of particular interest when compared to other SWBLIs due to the existence of steady subsonic flow behind the shockwave. As opposed to supersonic flow, this flow regime does not support discontinuities such as shockwaves and changes of flow conditions are gradual, while the surrounding flow must

satisfy both the supersonic and subsonic constraints posed by the governing equations. Consequently, this dictates the shock structure in terms of strength, shape and location by forward feeding the downstream conditions,since the subsonic region is sensitive to downstream disturbances propagating upstream [20]. For certain combinations of high Mach number and high angle of attack, this interaction can lead to a self-excited, self-sustained oscillation referred to as *transonic buffet*. Separated flow due to these oscillations results in additional pressure drag and the overall shock-buffet dynamics can excite the wing structure. This structural response is called *buffeting* and can result in e.g. an increase in fuel consumption and emissions associated with the drag penalty, poorer aerodynamic performance, and a general degrading of the handling qualities of the aircraft. Looking again at figures 1.1 and 1.2, the limits of these conditions can be seen marked as buffet boundary. To date, shock buffet is mitigated by limiting the flight envelope of the aircraft, allowing a 30% margin from the cruise point to buffet onset in the design process [21].

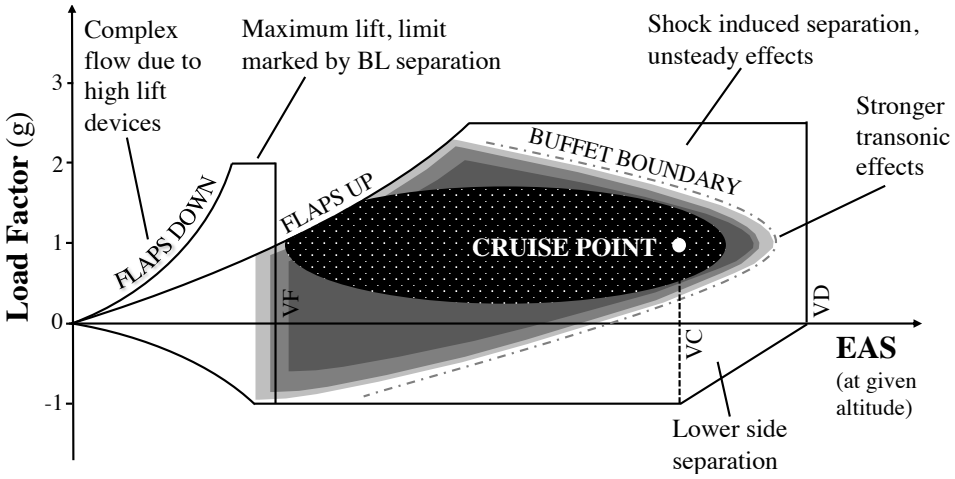

FIGURE 1.2. Flight envelope diagram for a typical large civil aircraft. VF, VC and VD indicate stall, cruise and dive velocities, respectively. The contours indicate level of confidence in CFD flow solutions and the dotted area indicates the normal operational range. Adapted from [2].

Designing the wings of future aircraft requires pushing the limits of the flight envelope since overcoming the engineering challenges posed at edge-of-the-envelope conditions is inextricably linked with understanding the physics that govern the phenomena encountered in said regimes. While extensive research has been done on transonic shock buffet since its discovery, the majority of the literature concerns the two-dimensional behaviour of the phenomenon observed on aerofoils and rectangular wings. Conversely, research on the complex aerodynamics of swept wing shock buffet is limited, compared to the work done for the two-dimensional case, and a unified explanation of the underlying flow mechanisms remains elusive [22]. This motivates extensive investigation of the phenomenon from industry and academia as more sophisticated wing designs enter service.

1.2 Aerofoil Shock Buffet

The first photographic evidence of transonic shock buffet was published in 1947 in the work of Hilton and Fowler, where rapid shockwave oscillations were observed on an aerofoil for an increasing Mach number [23]. Depending on the aerofoil shape, two shock buffet types were observed, one on biconvex aerofoils, referred to as *Type I*, and one on supercritical profiles referred to as *Type II*. Shock buffet *Type I* is characterized by a fixed frequency limit cycle oscillation (LCO) of the shockwave, in which the shock weakens as it moves upstream before reversing due to the reattachment of the separated flow close to the trailing edge. These oscillations occurred over approximately 20% of the chord and were in a 180° phase difference for the upper and lower surface. Following the investigations of McDevitt [24], Mabey [25, 26] and Gibb [27] a model successfully describing *Type I* shock buffet using the local Mach number as an onset predictor was developed by the last two.

The experimental work of Tijdeman [28], using trailing edge deflections on an aerofoil, played a vital role in classifying the different types of oscillations for *Type II* shock buffet, separating them in three distinct types. *Type A* shock buffet is characterised by a sinusoidal shock oscillation at a phase shift to the flap excitation. The shock increases in strength as it moves upstream and equally weakens during the downstream excursion. Similarly to *Type A*, *Type B* shock buffet, which occurs for a lower Mach number compared to *A*, demonstrates a sinusoidal response with only difference being the disappearance of the shock during the downstream motion. Finally, for *Type C* shock buffet, following the peak strength of the shock, which is achieved at a point during the upstream motion, the shock weakens again before radiating from the leading edge towards the oncoming flow. In an effort to characterise the nature of the upper surface separation for *Type II* shock buffet, two different models, namely *Model A* and *Model B*, shown in figure 1.3, depending on the location of the onset of the separation, referred to as the separation bubble, were proposed following the work Pearcey [29,30], Pearcey and Holder [31] and Pearcey et. al [3]. For *Model A*, a separation bubble first appears at the base of the shock and then extends towards the trailing edge causing large separation, referred to as bubble bursting, as the angle of attack increases, whereas in *Model B* trailing edge separation is also present or imminent. Additionally, three variants of the latter model were identified depending on the cause of the trailing edge separation. The model that was developed, used the pressure divergence of the trailing edge as an indicator to predict the shock buffet onset and defined a critical Mach number or angle of attack for which the separation bubble would burst, if present.

While the model for *Type I* was successful in describing the governing physics of shock buffet on biconvex aerofoils, discrepancies would arise between different approaches aiming to explain *Type II* shock buffet. In addition, due to the relevance of

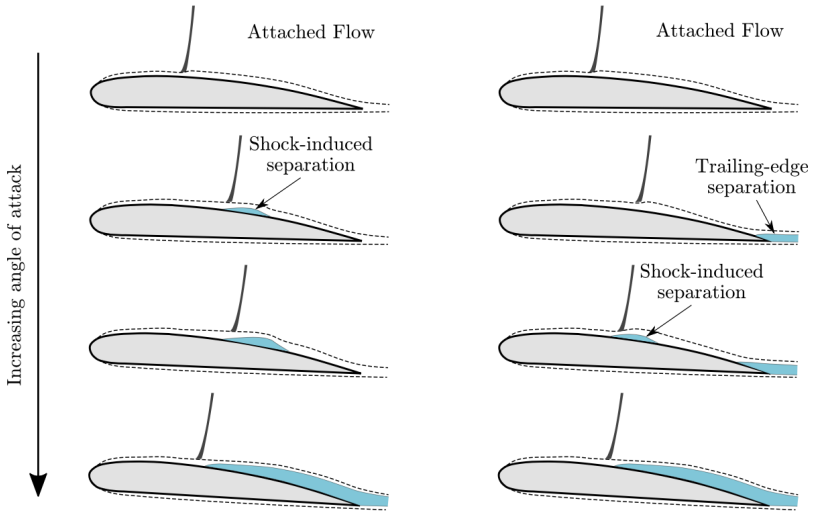

FIGURE 1.3. Different types of upper surface flow separation for increasing incidence that lead to *Type II* shock buffet, proposed by Pearcey et. al [3]. Separation initially appearing at the shock foot characterises *Model A* (left) whereas trailing-edge separation along with the shock-induced separation distinguishes *Model B* (right). Reproduced with permission and adapted from [4].

Type II shock buffet to industrial applications, the literature presented herein focuses on conditions and geometries pertinent to civil transport aircraft.

Early experiments of Roos were instrumental in demonstrating the differences of shock buffet between symmetrical and supercritical aerofoils. While the shock buffet dynamics were similar in both test cases, the difference in geometry resulted in a reduced tendency to develop buffeting fluctuations for increasing Mach number, and in general a smaller periodicity in lift and pressure fluctuations for the supercritical aerofoil [32]. Similar lift and pressure fluctuations were found in the experiments of Lee and Ohman [33] and Lee et al. [34]. These resulted in the formulation of the most well known model to describe *Type II* shock buffet that was based on the principle that the phenomenon frequency is governed by an acoustic wave-propagation mechanism [5] shown in figure 1.4. Essentially, in the first phase, pressure waves travelling downstream through the separated shear layer reach the trailing edge. In the second phase, pressure waves start propagating upstream above the separated shear layer in order to satisfy the Kutta condition. Finally, the energy exchange resulting from the interaction of these upstream waves with the shock, completes the feedback loop required to sustain the oscillations.

Over the following years, multiple experimental campaigns that aimed to study the nature of shock buffet reported similar results of low frequency oscillations (i.e. Strouhal numbers in the range of $0.05-0.08$) [35]. Experimental results agreeing with Lee's model further supported that the sound waves generated at the trailing-edge are responsible for the shock movement and that the trailing edge conditions are directly affected by

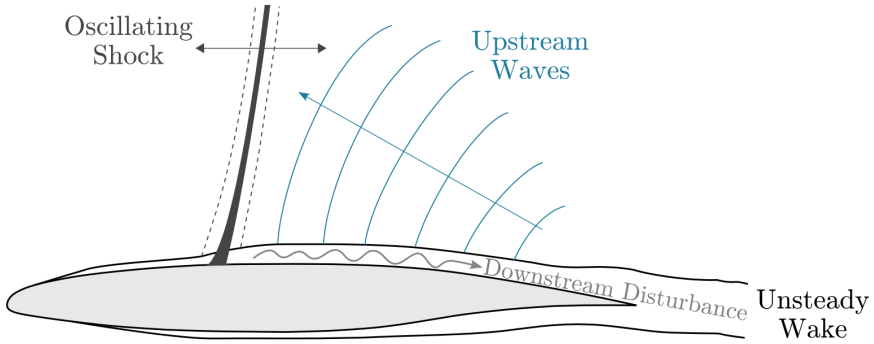

FIGURE 1.4. Wave-propagation feedback model for the self-sustained shock oscillations proposed by Lee [5], reproduced with permission and adapted from [4].

the shock position [35–37]. On the other hand, evidence that additional disturbances that travel along the lower surface, apart from those approaching the shock from the upper surface, was found in the extensive experimental campaign of Jacquin et al. [38] as well as in the work of Hartmann et al. [39]. The additional discrepancies that resulted when the upstream wave propagation velocity was sought, led to the proposal of a modification of the model from the former, that better agreed with experimental results. This can also be seen in numerical studies since some simulations produced results in good agreement with Lee's model [40, 41], whereas subsequent studies by Garnier and Deck [42] showed large discrepancies stemming from the sensitivity of the model to aerofoil geometry changes. This led to the hypothesis that the underlying complex flow dynamics prohibit the creation of an accurate generalised model [22].

A different approach to explaining the mechanism governing the phenomenon was made in the recent years by Crouch [11, 43, 44], who postulated that the unsteady oscillations can be explained by analysing the system from a stability theory perspective. Indeed, it was shown that the onset of the instability occurs when one of the least stable eigenvalues crosses the imaginary axis into the unstable half-plane, establishing a Hopf bifurcation. By considering small perturbations, the RANS equations were linearised and solved around a steady converged state, revealing a marginal eigenvalue that would become unstable when incidence was increased above a certain value. A comparison of the critical angle of attack calculated using global stability theory with the experimental results of McDevitt and Okuno [45] on the same aerofoil, demonstrated good agreement of results. This approach was further supported by the work of Sartor et al. [14] where it was shown that most of the eigenspectrum, resulting from the eigendemposition of the Jacobian matrix, remains unchanged for different angles of attack, except for the eigenvalue located in the proximity of the buffet frequency. Moreover, a closer examination of the spatial structure of the eigenmode associated with the unstable eigenvalue, shows that while the mode is mostly energetic within the shock, a contribution located in the mixing layer suggests that the shock displacement directly

influences the contraction and expansion of the separation bubble. Lastly, in addition to the global mode associated with the low frequency oscillations, medium frequency motions in the mixing layer and above the separated region suggest that there is an additional presence of a broadband unsteadiness related to the Kelvin–Helmholtz instability. By comparing the global stability approach of Crouch to Lee's model, different descriptions of the phenomenon dynamics arise. Specifically, Crouch states that the origin of the pressure perturbations is located at the shock foot. These perturbations will then move in the wall normal direction along the shock before propagating upstream after reaching the top of the shock as well as through the boundary layer with less intensity. Simultaneously, the downstream excursion of the shock intensifies the perturbations before they travel around the trailing edge and along the lower surface towards the leading edge. Nevertheless, both approaches describe the same phenomenon from a different perspective. This is also supported from the fact that the corrected acoustic feedback model suggested by Jacquin et al. [38] incorporates the qualitative flow features described by Crouch et al. [43].

On the numerical side, different techniques have been used to simulate transonic shock buffet on aerofoils. The first studies [46–48] on symmetric aerofoils aimed to assess the potential of unsteady RANS (URANS) simulations to capture the intricate shock buffet dynamics. Once the efficacy of URANS methods was validated with experimental results, subsequent simulation campaigns focused on supercritical aerofoils [41, 49, 50]. Additionally, RANS simulations also demonstrated the ability to capture the mean flow quantities [14, 50]. While these approaches proved to be capable of predicting the shock buffet flow features, they also demonstrated a high sensitivity to simulation parameters such as the choice of turbulence model, numerical scheme and the spatial and temporal discretisation. This encouraged studies that assessed the effect of the variation of the aforementioned parameters [51–54]. It is important to mention that since the shock motion is characterised by a low frequency, the timescales in which it exists are much longer than these of the shear layer eddies. Therefore, even if the small turbulent structures cannot be fully resolved due to the inherent averaging of RANS simulations, the basic flow physics can be computed with fair accuracy [14, 43]. Nevertheless, scale-resolving simulations ranging from detached-eddy simulations (DES), employing the zonal DES [55] and the delayed DES (DDES) [56], to large-eddy simulations (LES) [42, 57] allowed a more detailed look of the flow mechanisms in place. Even though direct numerical simulations (DNS) are computationally prohibitive for the high Reynolds numbers encountered at typical commercial transonic flight conditions, recent work by Zauner et al. [58], focused on a moderate Reynolds number of 5×10^5. Apart from the complex SWBLI observed, a higher lift oscillation frequency at a Strouhal number of approximately 0.1 was found. Lastly, studies on laminar aerofoils showed that in these conditions, the shock oscillations occur at much higher frequencies (approximately two

orders of magnitude higher) but at lower amplitudes (6% of chord length compared to 20% for turbulent cases) [59, 60].

Most numerical and experimental studies on the topic of transonic shock buffet over the years have focused on elucidating the governing physics of the phenomenon as well as predicting its onset. Focusing on classifying the flow features, shock buffet studies utilized rigid aerofoils and wings, excluding the effects of any interactions with the elastic wing structure. One of the first studies that looked further into fluid-structure interaction in unsteady periodic flows scrutinised the flow around an elastically suspended circular cylinder [61]. The lock-in behaviour observed, namely the synchronisation of the vortex shedding frequency to the natural vibration frequency of the structure (or the frequency that the structure is excited at) resulting in oscillations of increased amplitude, was attributed to resonance due to vortex induced vibration [62]. While additional studies on aerofoils speculated that a resonance mechanism is excited by shock buffet, the asymmetric nature of the lock-in boundaries [63] being shifted towards higher frequencies [64, 65], could not be fully explained by the resonance idea. More specifically, both single and two degree-of-freedom (pitch and pitch-and-heave) aerofoil systems did not demonstrate significant oscillations for lower forcing frequencies but increased amplitudes were observed for higher frequencies [64]. It is also important to mention that lock-in was observed when the excitation amplitude was above some threshold. In addition, experimental studies on flexible swept wings showed that at high-speed conditions, where a strong shock-wave/boundary-layer interaction is present, there was a strong fluid-structure coupling, with the frequency of the aeroelastic response following that of the oscillating flow field and not a structural eigenmode [66]. Reduced order models (ROMs) have shown the potential to efficiently capture the behaviour of nonlinear aeroelastic systems in incompressible and transonic conditions [67]. In the work of Gao et al. [68], a two-dimensional aeroelastic ROM showed that many characteristics such as coupling frequency can be predicted through a linear stability analysis. The same study also showed that the synchronisation of the aerodynamic and structural systems, leading to a limit-cycle oscillation, was related to an unstable coupled fluid mode. This was scrutinised recently showing that the buffet onset is reduced by an elastic structure and the fluid-structure interaction can destabilise an originally stable fluid mode [69].

1.3 Finite Wing Shock Buffet

Early efforts to investigate transonic shock buffet on wings involved both flight [70] and wind-tunnel tests [71, 72]. Despite the hypothesis that aerofoil shock buffet is mainly a two-dimensional phenomenon, small discrepancies between the behaviour of aerofoil and wing shock buffet that emerged even for rectangular wings with constant cross sec-

tion questioned its validity [38]. In the experiments of Roos [72] on a high aspect ratio swept wing, while the convection frequency of the pressure fluctuations was consistent with his earlier experiments on aerofoils, large scale unsteadiness concentrated closer to the wingtip was observed. Additionally, the oscillations appeared to be occurring at a higher frequency and were broadband in nature (Strouhal numbers based on mean aerodynamic chord ranging from 0.2 to 0.6), as opposed to the distinct frequency found for aerofoils. This behaviour was consistent with the findings of subsequent experimental studies of Benoit and Legrain [73] who showed that the organised flow fluctuations observed at transonic speeds do not follow through at buffet onset. Differences were also found regarding the location of the origin of the unsteadiness after introducing sweep. The narrowband pressure undulations for unswept wings originated at the root and extended further outboard with increasing incidence, in contrast to the swept wing case where the unsteadiness first emerges at the wingtip before propagating towards the root. The effects of different Mach number and Reynolds number on swept wings were investigated in the recent experiments of Dandois [74]. It was shown that for increasing Reynolds number, the buffet onset is marginally delayed, regardless of the angle of attack, while as the Mach number increases, the onset occurs at smaller incidences combined with an aft displacement of the the shock location. Moreover, it was highlighted that a secondary high frequency instability (Strouhal numbers ranging between 1 and 4) related to that of Kelvin–Helmholtz, coexists along the buffet instability, something previously observed for aerofoils [14]. Furthermore, experiments over a wide range of angles of attack by Koike et al. [75] on the NASA Common Research Model (CRM) revealed three distinct behaviours for increasing incidence. For angles of attack below 3° small intensity fluctuations are present but the shock is mainly stationary. As the incidence is increased between 3° and 5.5°, oscillations become more evident, with the spectral content agreeing with earlier findings of Roos [72] and Dandois [74] (Strouhal numbers of approximately 0.3). Finally, for angles of attack above 5.5°, low broadband frequency aperiodic shock motions are observed at the same frequency, similar to the findings of Benoit and Legrain [73].

As the equipment and techniques used in wind tunnel tests became more sophisticated, more thorough analyses were possible with prime example the application of pressure sensitive paint (PSP) which allowed a more detailed insight on the complex flow features. Even though the first studies using the aforementioned paint suffered from issues related to the luminescence intensity of the paint [76] or the videographic equipment [66], the experimental campaigns by Lawson et al. [77] on the RBC12 half-wing model and Sugioka et al. [78] on an 80% scale model of the CRM, using fast-response and dynamic PSP (DPSP) respectively, successfully produced a plethora of valuable results. In addition to the paint, conventional instrumentation in order to assess the accuracy of the buffet onset indicators put forth by ESDU [79] was performed for the

RBC12. Consistent results were found for predicting structural buffeting onset using wing root strain divergence, root mean square (RMS), breaks in the lift curve and trailing edge pressure divergence apart from axial force divergence and pitching moment break. The response frequency coincided with that of the broadband pressure oscillations at Strouhal numbers ranging between 0.05 and 0.15, something that would broaden to 0.08 and 0.5, when the incidence was increased. Finally, in an attempt to distinguish general shock buffet characteristics and case dependent ones, Paladini et al. [80] analysed and compared four different experimental databases from wind tunnel tests on swept wings. Similarly to experiments not included in the analysis, consistent Strouhal numbers ranging between 0.2 and 0.3 were found.

On the numerical side, Brunet and Deck [81] employed the zonal DES method to simulate shock buffet on a half-wing model previously studied experimentally [82]. Apart from the successfully predicted time-averaged separation area and outboard unstable region, three-dimensional acoustic pressure waves radiating upstream were observed. Good correlation of mean and RMS pressure distribution with the experiment was found. More recently, Ishida et al. [83] performed a zonal DES simulation on the CRM, obtaining overall good agreement with experimental results, albeit with the shock front located further upstream. Using the same RBC12 geometry studied by Lawson et al. [77], Sartor and Timme performed both steady and unsteady RANS [84] and DDES [6] simulations using different turbulence closures and discretization schemes. Their results further established the outboard shock motions as a characteristic of wing shock buffet. More specifically, the area of this unsteadiness first appears close to the wingtip and extends inboard as the angle of attack is increased, shown in figure 1.5. In addition, as the unsteady shock motion extends to spanwise stations of larger chord, the dominant frequency becomes broadband. A comparison of the two computational methods, demonstrated the ability of the URANS to reproduce the dominant flow features, even though DDES appeared to be more consistent with experimental results regarding the shock location. Extending their work, Sartor and Timme also studied the effect of Mach number ranging from 0.76 to 0.84 [85]. It was found that an increase in Mach number decreases the onset angles of attack. Moreover, for high Mach numbers, the unsteadiness observed was confined to the separated areas, whereas the standard deviation of the lift oscillations plateaued soon after onset. Conversely, in the low Mach number case, even though the separated area was smaller, large amplitude pressure undulations extending across the upper wing surface were observed.

Simulations on infinite-swept wings using URANS by Iovnovich and Raveh [86] focused on investigating the effects of different sweep angles and aspect ratios (AR). This allowed to quantify the sweep angles above which, three-dimensional effects dominate the phenomenon. Indeed, for sweep angles less that 20°, the flow behaviour resembles

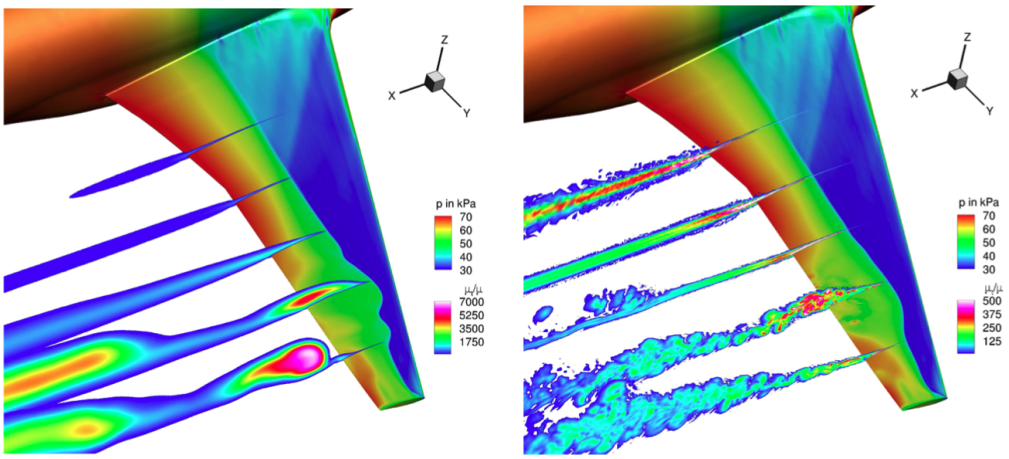

(a) URANS (b) DDES

FIGURE 1.5. Instantaneous values of eddy-viscosity ratio for the RBC12 half-wing model at design conditions, reproduced with permission and adapted from [6].

that observed on aerofoils where the oscillations are limited in the chordwise direction. Separation bubbles along with a wavy front appear when the sweep angle is increased between 20° and 40°, while pressure waves start to propagate outboard. The term *buffet cells* was used to describe these outboard running pressure perturbations coupled with the separation bubbles. In addition, an increase in sweep angle resulted in an increased oscillation frequency but decreased the amplitude. Stall due to the shock-induced separation is observed for sweep angles above 40°. It is worth pointing out here that modern large aircraft wings have a typical sweep angle of about 30°. Regarding AR effects, a wing tip vortex interaction with the spanwise shock oscillations occurs for ARs ranging between 3 and 4, something that diminishes for higher AR values. Recently, topological similarities between buffet cells and stall cells suggest that the two phenomena share common flow physics [87]. Infinite wings pose an interesting case for stability analysis since their concept allows for a problem formulation that is inhomogeneous in two spatial directions while periodic boundaries can be imposed in the third direction, referred to as biglobal analysis [88]. Recent application of biglobal analysis on infinite wings [89–91] have demonstrated that a three-dimensional mode that is damped for straight wings, becomes oscillatory when a sweep angle in introduced, correlating the *buffet cells* mentioned earlier to an aerodynamic mode. This mode co-exists with the characteristic shock buffet mode. Similar findings of spanwise-periodic modes were also reproduced in the triglobal (three inhomogeneous directions) [92] and resolvent [93] studies of He and Timme on infinite swept wings.

For aircraft wings, earlier linearised-aerodynamic computations by Timme and Thormann [94] on the RBC12 showed that the unsteadiness may be attributed to an unstable aerodynamic mode, analogous to the two-dimensional global instability found for aerofoils and explained above. Indeed, a global analysis of the CRM by Timme [95]

revealed an unstable eigenvalue post shock buffet onset, linking the associated eigenmode to *buffet cells*. Furthermore, the additional modes that are present and stable, yet have a small decay rate, explain the characteristic broadband frequency of wing shock buffet. In both studies the eigenvalue computations of the large fluid Jacobian were achieved by using preconditioned iterative methods since direct methods for eigenvalue computations would require excessive amounts of memory for such matrix dimensions. This has recently shown the potential to extend global analysis to even larger systems that stem from a fluid-structure coupling [9], an area where literature is extremely limited especially in the case of wing shock buffet flow.

Finally, while most studies on wings focus on the global instability associated with the localised outboard broadband oscillations, an additional phenomenon of inboard running spanwise waves, has been observed in most wind tunnel studies [74, 77, 96] that occurs at much lower frequencies. This phenomenon was exclusive to wind tunnel results until recently, where a long-wavelength mode was found from a biglobal analysis of an infinite wing [89]. Evidence of that behaviour on finite wings was also seen in the harmonic structural excitation studies mentioned earlier [94], where a resonant peak of the dynamic derivatives was found for a low excitation frequency. The spatial pattern associated with the response to that forcing was shown to be dominated by the shock dynamics. Moreover, dynamic mode decomposition and proper orthogonal decomposition performed on data from RANS/DDES and zonal DES simulations on RBC12 [97] and CRM [98] respectively, revealed a low frequency inboard propagating mode apart from the global instability. The absence of a global instability at the vicinity of that low frequency, could suggest that pseudo-resonance due to the non-normality of the Navier–Stokes equations (or a convective instability) is responsible for that behaviour. A resolvent analysis of a coupled fluid-structure CRM model [99] revealed a small gain amplification around that low-frequency range. Nevertheless, work on that characteristic behaviour of shock buffet remains limited, therefore the possibility that wind tunnel noise can exploit the receptivity of the shock to upstream and/or downstream perturbations [100], cannot be ruled out.

1.4 Aim & Objectives of Work and Thesis Outline

The aim of this project is the investigation of the interaction of transonic buffet with wing vibration in the case of swept wings and the role of the amplification of optimal disturbances in the case of aerofoils. While most literature focuses on the pure aerodynamic behaviour of the phenomenon, real aircraft wings are inherently elastic structures and therefore a thorough scrutiny of the phenomenon calls for multi-disciplinary simulations. Simultaneously, the study of transonic buffet on aerofoils in environments with

high external disturbance levels, such as wind tunnels, motivates the scrutiny of the potential effect these can have on the flow behaviour. The present work aims to contribute in the understanding of the transonic buffet phenomenon by addressing these gaps in the literature that will ultimately help designing the wings of the future.

This thesis will address three principal objectives to fulfil the aforementioned aim. First, a linearised-aerodynamics analysis, commonly used for flutter analysis is used to compare the effect of different wing designs on shock buffet. This is then extended to a time-accurate study on one of the geometries, to examine how larger amplitude excitations at frequencies in the vicinity of shock buffet affect the unstable flow. Secondly, a state-of-the-art nonlinear coupled fluid-structure simulation is carried out alongside an unsteady RANS (URANS) simulation to assess the effect of aeroelastic coupling on the flow response. Finally, nonmodal stability analysis on a supercritical aerofoil aims to showcase the effect of the amplification of optimal disturbances on two-dimensional shock buffet and set the foundation of transient growth analysis in steady turbulent conditions.

The present thesis is organised as follows. Chapter 2 outlines the theoretical background along with implementation details. The governing equations are presented along with their formulations for the linearised frequency domain analysis, time-accurate simulations, modal and nonmodal analysis. The characteristics of the geometries used in the different studies along with relevant numerical and experimental data as well as steady-states are described in Chapter 3. Moving on to the results, Chapter 4 focuses on the effect of harmonic excitation, initially by comparing the linearised-aerodynamic response of two different aircraft, namely the RBC12 and the NASA Common Research Model (CRM), followed by an extension of the same approach to the nonlinear regime for the former geometry. An assessment of the fluid-structure interaction (FSI) compared to fluid-only simulation, first one to the authors knowledge on aircraft wings at shock buffet conditions, is presented for the CRM in Chapter 5. Modal and nonmodal stability analysis results, using a finite-volume industrial code, are validated against previous work in the incompressible regime for a cylinder in Chapter 6. This is then followed by the application of the method on the supercritical aerofoil OAT15A at pre- and post-onset conditions. Lastly, in Chapter 7, a summary with the key findings from all the studies conducted herein is presented along with recommendations for future work.

Chapter 2

Theory and Methods

2.1 Introduction

In recent decades, Computational Fluid Dynamics (CFD) has been widely accepted in the aeronautical industry as a powerful and mature tool at least for parts of the flight envelope pertaining to cruise conditions. While a complete replacement of wind tunnel and flight testing is still improbable, CFD provides important complementary utilities to the traditional methods and can guide new designs. Especially nowadays, the developments in high performance computing allow the extensive use of CFD in the design phase. In this chapter the theoretical background along with any associated formulations are presented.

2.2 Equations of fluid motion

The dynamical behaviour of a viscous fluid is governed by the Navier–Stokes equations. The equations are derived by applying three fundamental laws of nature, namely:

- Conservation of mass, known as the continuity equation
- Newton's second law about conservation of momentum
- First law of thermodynamics about conservation of energy

The governing equations for a compressible and viscous fluid in differential dimensional form can be written with the aid of tensor notation described in Appendix A as

$$
\begin{aligned}
\frac{\partial \rho}{\partial t} + \frac{\partial}{\partial x_i}(\rho u_i) &= 0 \\
\frac{\partial}{\partial t}(\rho u_i) + \frac{\partial}{\partial x_j}(\rho u_j u_i) &= -\frac{\partial P}{\partial x_i} + \frac{\partial \tau_{ij}}{\partial x_j} \\
\frac{\partial}{\partial t}(\rho E) + \frac{\partial}{\partial x_j}(\rho u_j H) &= \frac{\partial}{\partial x_j}(\rho u_i \tau_{ij}) - \frac{\partial q_j}{\partial x_j}
\end{aligned}
\tag{2.1}
$$

where x_i symbolises Cartesian coordinates ($x_1 = x, x_2 = y, x_3 = z$), t the time, u_i the velocity vector ($u_1 = u, u_2 = v, u_3 = w$), ρ the density, E and H the total energy and enthalpy, respectively, P the static pressure, T the static temperature and τ_{ij} the viscous stress tensor. Fourier's law of heat conduction is used for modelling the heat flux q_j which is defined as $q_j = -\kappa(\partial T/\partial x_j)$ for a fluid with thermal conductivity κ. The total energy E and enthalpy are given by

$$
E = e + \frac{|u_i|^2}{2} \qquad \text{and} \qquad H = h + \frac{|u_i|^2}{2} \tag{2.2}
$$

where e is the internal energy and h the enthalpy per unit mass. The viscous stress tensor is defined as

$$
\tau_{ij} = 2\mu S_{ij} + \boldsymbol{\lambda}\frac{\partial u_k}{\partial x_k}\delta_{ij} = 2\mu S_{ij} - \left(\frac{2\mu}{3}\right)\frac{\partial u_k}{\partial x_k}\delta_{ij} \tag{2.3}
$$

after using the Stokes hypothesis [101] that dynamic viscosity μ is related to the second viscosity $\boldsymbol{\lambda}$ according to $\boldsymbol{\lambda} = -\frac{2}{3}\mu$. This relation is know as bulk viscosity. The second term in equation (2.3) ($\frac{\partial u_k}{\partial x_j}$), represents the velocity divergence, existing only for compressible flows, and δ_{ij} is the Kronecker delta. The components of the strain-rate tensor S_{ij} are

$$
S_{ij} = \frac{1}{2}\left(\frac{\partial u_i}{\partial x_j} + \frac{\partial u_j}{\partial x_i}\right) \tag{2.4}
$$

The Navier–Stokes equations for a three dimensional flow field consist of five simultaneous equations for the five conservative variables $\rho, \rho u, \rho v, \rho w, \rho E$. Specifically, their solution involves seven unknown variables namely: ρ, u, v, w, E, P and T. While there are constitutive relations for non-perfect gases, the thermodynamic relations that describe a perfect gas are used herein. The equation of state and the thermodynamic relationships for such a gas are given by

$$P = \rho RT \qquad \text{where} \qquad R = c_p - c_v, \;\; \gamma = \frac{c_p}{c_v} \tag{2.5}$$

where R is the specific gas constant, c_p and c_v the specific heat coefficients at constant pressure and volume respectively and γ the specific heat capacity ratio. For air, these values are $R = 287$ J/(kg $\cdot$ K) and $\gamma = 1.4$. Additionally, the variation of dynamic viscosity is related to temperature according to Sutherland's law defined as

$$\mu = \mu_0 \left(\frac{T}{T_0}\right)^{3/2} \frac{T_0 + S}{T + S} \tag{2.6}$$

where $S = 110.4$ K is the Sutherland temperature constant, $\mu_0 = 1.716 \times 10^{-5}$ kg/(m$\cdot$s) and $T_0 = 273.15$ K are the reference dynamic viscosity and temperature respectively. Finally, the thermal conductivity κ is given by

$$\kappa = c_p \frac{\mu}{Pr} \tag{2.7}$$

where a Prandlt number of $Pr = 0.72$ and is assumed to be valid throughout the entire flow field.

2.2.1 Favre- and Reynolds-Averaged Navier–Stokes equations

Despite the technological strides in the ever increasing capabilities of modern supercomputers, a direct numerical simulation (DNS) of the Navier–Stokes equations still remains prohibitive, in terms of computational resources, for industrially relevant cases and is applicable only to simple flow problems at low Reynolds numbers in the order of $10^4 - 10^5$. This is due to the increasing difficulty of solving the equations when the geometry in question is complex and the resulting flow is turbulent. When this is combined with the increasing number of grid points to achieve sufficient spatial resolution that scale as $Re^{9/4}$ and the CPU-time as Re^3 [102] it becomes evident that the solution of such a system is not viable in an industrial context. Therefore, models that only approximate the effects of turbulence are needed [102]. One of these approximations are the Reynolds–averaged Navier–Stokes equations, presented by Reynolds in 1895 [103]. This is based on the decomposition of the flow into a mean and a fluctuating part, which for e.g. pressure P can be written as

$$P = \overline{P} + \epsilon P' \tag{2.8}$$

where $\overline{P}$ symbolises the mean state and $\epsilon P'$ the small fluctuation. There are three main methods to average the variables for the mean part of the Reynolds decomposition, namely time averaging, spatial averaging and ensemble averaging. Time averaging is appropriate for most engineering applications that demonstrate, on average, stationary turbulent flows and is used consistently herein. In cases where turbulence is, on average, uniform in all directions, spatial averaging is employed. This is achieved by using a volume integral averaged over all spatial coordinates such as

$$u_i = \lim_{V\to\infty} \frac{1}{V} \int\int\int_V u_i \, dV \tag{2.9}$$

Ensemble averaging is used for flows that decay with time and the mean is obtained by averaging the measurements of a variable from N identical experiments. Therefore, the mean value in the n^{th} experiment, can be expressed as

$$u_i = \lim_{N\to\infty} \frac{1}{N} \sum_{n=1}^{N} {u_i}^n \tag{2.10}$$

where ${u_i}^n$ is the n^{th} measurement. In the present work, where compressible flow is assumed, the density (mass) weighted (or Favre) decomposition is applied in addition to the time average. For example, the average of the velocity components are obtained from

$$u_i = \frac{1}{\overline{\rho}} \lim_{\Delta t\to\infty} \frac{1}{\Delta t} \int_t^{t+\Delta t} \rho u_i \, dt \tag{2.11}$$

where $\overline{\rho}$ is the Reynolds-averaged density and Δt is a time interval. Similarly to equation (2.8) the Favre decomposition reads

$$u_i = \tilde{u}_i + u_i'' \tag{2.12}$$

By applying equation (2.8) to density and pressure and (2.12) to the rest of the flow variables and substituting in equation (2.1) we arrive at the Favre- and Reynolds-averaged Navier–Stokes equations

$$
\begin{aligned}
\frac{\partial \overline{\rho}}{\partial t} + \frac{\partial}{\partial x_i}(\overline{\rho}\tilde{u}_i) &= 0 \\
\frac{\partial}{\partial t}(\overline{\rho}\tilde{u}_i) + \frac{\partial}{\partial x_j}(\overline{\rho}\tilde{u}_j\tilde{u}_i) &= -\frac{\partial \overline{P}}{\partial x_i} + \frac{\partial}{\partial x_j}(\tilde{\tau}_{ij} - \overline{\rho}\widetilde{u_i'' u_j''}) \\
\frac{\partial}{\partial t}(\overline{\rho}\tilde{E}) + \frac{\partial}{\partial x_j}(\overline{\rho}\tilde{u}_j\tilde{H}) &= \frac{\partial}{\partial x_j}\left(\kappa\frac{\partial \tilde{T}}{\partial x_j} - \overline{\rho}\widetilde{u_j'' h''} + \widetilde{\tau_{ij} u_i''} - \overline{\rho}\widetilde{u_j'' K_t}\right) \\
&\quad + \frac{\partial}{x_j}[\tilde{u}_i(\tilde{\tau}_i j - \overline{\rho}\widetilde{u_i'' u_j''})]
\end{aligned}
\tag{2.13}
$$

The trailing term in the momentum and energy equations is the Favre-averaged Reynolds-stress tensor given by

$$
\tau_{ij}^F = -\overline{\rho}\widetilde{u_i'' u_j''} \tag{2.14}
$$

In addition, K_t denotes the turbulent kinetic energy [104], the definition of which, along with its Favre decomposition, is given by

$$
K_t = \frac{1}{2}\overline{(u_i')^2} \qquad\qquad \overline{\rho}\tilde{K}_t = \frac{1}{2}\overline{\rho}\widetilde{(u_i')^2} \tag{2.15}
$$

allowing to express the energy and enthalpy terms of equation (2.13) as

$$
\overline{\rho}\tilde{E} = \overline{\rho}\tilde{e} + \frac{1}{2}\overline{\rho}\tilde{u_i}^2 + \frac{1}{2}\overline{\rho}\widetilde{(u_i')^2} = \overline{\rho}\tilde{e} + \frac{1}{2}\overline{\rho}\tilde{u_i}^2 + \overline{\rho}\tilde{K}_t \tag{2.16}
$$

$$
\overline{\rho}\tilde{H} = \overline{\rho}\tilde{h} + \frac{1}{2}\overline{\rho}\tilde{u_i}^2 + \frac{1}{2}\overline{\rho}\widetilde{(u_i')^2} = \overline{\rho}\tilde{h} + \frac{1}{2}\overline{\rho}\tilde{u_i}^2 + \overline{\rho}\tilde{K}_t \tag{2.17}
$$

Furthermore, for transonic and supersonic flows, it is valid to assume that the contributions of the molecular diffusion $\frac{\partial}{\partial x_j}(\widetilde{\tau_{ij} u_i''})$ and turbulent transport $\frac{\partial}{\partial x_j}(\overline{\rho}\widetilde{u_j'' K_t})$ terms of the mean turbulent kinetic energy $\tilde{K}_t$ are negligible and therefore are omitted from equations (2.13) [104]. To solve the Favre- and Reynolds-averaged Navier–Stokes equations (2.13), six components of the Favre-averaged Reynolds-stress tensor and three components of the turbulent heat-flux vector need to be supplied.

The Boussinesq hypothesis [105] assumes that the turbulent shear stress is proportional to the mean rate of strain by a factor μ_t which is termed as eddy viscosity. Using this assumption, the viscous stress tensor of the Favre- and Reynolds-averaged

Navier–Stokes equations is formed similarly to equation (2.3) and can be written as

$$\tau_{ij}^{F} = -\overline{\rho}\widetilde{u_i'' u_j''} = 2\mu_t \tilde{S}_{ij} - \left(\frac{2\mu_t}{3}\right)\frac{\partial \tilde{u}_k}{\partial x_k}\delta_{ij} - \frac{2}{3}\overline{\rho}\tilde{K}\delta_{ij} \tag{2.18}$$

The implication of the eddy-viscosity approach on the dynamic viscosity coefficient μ of equation (2.3) is simply its replacement by the sum of a laminar and turbulent component $\mu = \mu_l + \mu_t$. The former is calculated using equation (2.6) whereas the latter is provided by the turbulence model and depends on the type of closure. The classical Reynolds analogy is used to model the turbulent heat-flux vector as

$$\overline{\rho}\widetilde{u_j'' h''} = -\kappa_t \frac{\partial \tilde{T}}{\partial x_j} \tag{2.19}$$

where the turbulent thermal conductivity coefficient κ_t is computed by solving equation (2.7) using the turbulent dynamic viscosity μ_t and the turbulent Prandtl number Pr_t which, similarly to its laminar counterpart, is assumed to be constant within the flow field. Herein, the value of $Pr_t = 0.9$ is assumed.

2.2.2 Spalart-Allmaras Turbulence Model

A large variety of turbulence models have been developed aiming to introduce the minimum amount of complexity while capturing the essence of the relevant physics [104]. Usually, different models are classified depending on their complexity. There are principally five classes, namely, algebraic (or zero-equation), one-equation, multiple-equation, second-order closures and large-eddy simulation. The Spalart–Allmaras (SA) is a first-order one-equation turbulence model developed based on empirical results, dimensional analysis, Galilean invariance and selective dependence on the molecular viscosity [106]. It is frequently used for turbulent wall-bounded flows with adverse pressure gradients in aerospace applications. Essentially, a transport equation is employed for computing an eddy-viscosity variable $\hat{\nu}$ that in return is used to calculate the turbulent eddy viscosity according to

$$\mu_t = f_{v1}\rho\hat{\nu} \tag{2.20}$$

where f_{v1} is function that is applied as a postprocessing step to capture the viscous damping effects close to the wall and therefore better approximate the variation of the velocity parallel to the wall which has a quartic profile in the viscous sub-layer [107]. This is achieved by multiplying the eddy-viscosity variable $\hat{\nu}$, which varies linearly with

the distance from the wall, with a function that has a cubic behaviour given by

$$f_{v1} = \frac{\chi^3}{\chi^3 + c_{v1}^3} \qquad \text{where} \qquad \chi = \frac{\hat{\nu}}{\nu_l} \text{ and } c_{v1} = 7.1 \tag{2.21}$$

where ν_l is the laminar kinematic viscosity given by $\nu_l = \mu_l/\rho$.

The transport equation that is solved for the eddy-viscosity in conservation form is

$$\begin{aligned} \frac{\partial \hat{\nu}}{\partial t} + \frac{\partial}{\partial x_j}(\rho \hat{\nu} u_j) = & \underbrace{c_{b1}\mathcal{S}\rho\hat{\nu}}_{\text{Production}} + \underbrace{\frac{1}{\sigma}\left[\frac{\partial}{\partial x_j}\rho(\nu_l + \hat{\nu}) + c_{b2}\rho\left(\frac{\partial \hat{\nu}}{\partial x_j}\right)^2\right]}_{\text{Diffusion}} \\ & - \underbrace{c_{w1} f_w \rho \left(\frac{\hat{\nu}}{d}\right)^2}_{\text{Near-wall Destruction}} \end{aligned} \tag{2.22}$$

The production term assumes that the generation of turbulence is proportional to the shear rate $\mathcal{S}$ of the mean velocity gradient. The diffusion term, frequently found in transport equations, contains a nonlinear term $(\frac{\partial \hat{\nu}}{\partial x_j})^2$ which was added to control the spreading of the wake at the edge of a turbulent region. For this reason, the diffusion part often appears in literature as a combination of a linear part and a source term to ensure that the original diffusion term remains linear and the source term is treated explicitly. The final and negative term represents the destruction of turbulence at the wall. This is achieved by using the inviscid blocking of pressure fluctuations in the unsteady turbulent field away from the wall and the viscous damping very close to the wall, depending on the distance denoted as d [106]. Additionally, in equations (2.21) and (2.22), terms c and f represent constants and auxiliary functions, respectively, and can be found in [106]. The negative SA model uses a modified transport equation to deal with negative $\hat{\nu}$ solutions and to address issues with underresolved grids and non-physical transient states [108]. Finally, the SA model, similarly to other one-equation models [109], tends to underpredict flow separation and produce inaccuracies in cases of post-shock reattachment in adverse pressure gradients as well as shear flows [106]. Nevertheless, the ability of the model to capture the adverse pressure gradient introduced by the shockwave, renders it appropriate for modelling transonic buffet and is used consistently in the present work. For more detailed information about turbulence and the differences between turbulence models the reader is referred to the book by Wilcox [104].

2.3 Finite Volume Formulation

The analytical solution to the Navier–Stokes equations becomes strenuous for complex flow problems and therefore a discretization of the physical space is required. Finite volume discretization directly uses the conservation laws as equations (2.13) can be integrated over finite control volumes. By using the time-dependent velocity and coordinate vectors $\boldsymbol{u}$ and $\boldsymbol{x}$ defined as

$$\underbrace{\boldsymbol{u}(\boldsymbol{x}(t),t) = [u(\boldsymbol{x},t), v(\boldsymbol{x},t), w(\boldsymbol{x},t)]}_{\text{Velocity Field}} \quad \text{and} \quad \underbrace{\boldsymbol{x}(t) = [x(t), y(t), z(t)]}_{\text{Grid Deformation}} \tag{2.23}$$

equations (2.13) can be expressed in conservative arbitrary Lagrangian-Eulerian form for a physical domain $\Omega(t) \subset \mathbb{R}^3$ with a boundary $\partial\Omega(t)$ as

$$\frac{\partial}{\partial t}\int_{\Omega(t)} \boldsymbol{q}_f \,\mathrm{d}\Omega + \int_{\partial\Omega(t)} (F_c \cdot n - F_v \cdot n - \boldsymbol{q}_f \dot{\boldsymbol{x}} \cdot n)\,\mathrm{d}S = \int_{\Omega(t)} \Phi \,\mathrm{d}\Omega \tag{2.24}$$

where n is the unit normal vector and $\boldsymbol{q}_f$ is the state vector, containing the conservative variables and the eddy-viscosity as

$$\boldsymbol{q}_f = [\rho, \rho\boldsymbol{u}, \rho E, \rho\hat{\nu}]^T \tag{2.25}$$

and Φ is the source term, which comprises all volume sources including the additional terms from the turbulence model on the right-hand side of equation (2.22). The directed surface elements of the boundary $\partial\Omega(t)$ are described by $\mathrm{d}S = n\partial\Omega(t)$. The convective and viscous flux vectors are denoted by F_c and F_v, respectively. In a typical simulation, equation (2.24) is solved for each control volume Ω. By applying the method of lines, equation (2.24) can be written as a system of coupled ordinary differential equations in time

$$\frac{\mathrm{d}V\boldsymbol{q}_f}{\mathrm{d}t} = -\boldsymbol{R}_f(\boldsymbol{q}_f, \boldsymbol{x}, \dot{\boldsymbol{x}}) \tag{2.26}$$

where V represents the volume matrix. The complete spatial discretization including the source term, $\boldsymbol{R}_f$, is termed as the residual and it is a nonlinear function of the conservative variables $\boldsymbol{q}_f$. In numerical methods, $\boldsymbol{R}_f$ is a measure of iterative error, and decreases as a more accurate solution is found.

2.4 Linearised Frequency Domain Analysis

The Linearised Frequency Domain (LFD) method is presented next. The detailed formulation and implementation can be found in [110]. By considering that an unsteady motion has a small amplitude, we can separate the variables from equation (2.23) into a mean state and a time-dependent small perturbation as

$$\boldsymbol{q}_f = \overline{\boldsymbol{q}}_f + \epsilon \boldsymbol{q}'_f(t) \qquad \text{and} \qquad \boldsymbol{x} = \overline{\boldsymbol{x}} + \epsilon \boldsymbol{x}'(t), \quad \epsilon \ll 1 \tag{2.27}$$

Substituting this into equation (2.26) and linearising about the mean state (discarding all terms beyond $\mathcal{O}(\epsilon)$), we can obtain the time-dependent linear equation for the flow perturbation

$$V\frac{\mathrm{d}\boldsymbol{q}'_f}{\mathrm{d}t} + \overline{\boldsymbol{q}}_f\frac{\mathrm{d}V}{\mathrm{d}t} + \boldsymbol{R}_f(\overline{\boldsymbol{q}}_f, \overline{\boldsymbol{x}}, \overline{\dot{\boldsymbol{x}}}) + \frac{\partial \boldsymbol{R}_f}{\partial \boldsymbol{q}_f}\boldsymbol{q}'_f + \frac{\partial \boldsymbol{R}_f}{\partial \boldsymbol{x}}\boldsymbol{x}' + \frac{\partial \boldsymbol{R}_f}{\partial \dot{\boldsymbol{x}}}\dot{\boldsymbol{x}}' = 0 \tag{2.28}$$

where the steady state $\boldsymbol{R}_f(\overline{\boldsymbol{q}}_f, \overline{\boldsymbol{x}}, \overline{\dot{\boldsymbol{x}}})$ is assumed to be negligibly small. Additionally, if we assume that the solutions to the perturbations are periodic with a frequency ω, they can be expressed as a Fourier series

$$\boldsymbol{q}'_f(t) = \sum_{n_h=1}^{\infty} \hat{\boldsymbol{q}}_f e^{in_h\omega t} \qquad \text{and} \qquad \boldsymbol{x}'(t) = \sum_{n_h=1}^{\infty} \hat{\boldsymbol{x}} e^{in_h\omega t}, \;\; \hat{\boldsymbol{q}}_f, \hat{\boldsymbol{x}} \in \mathbb{C} \tag{2.29}$$

which for a first harmonic excitation and response ($n_h = 1$) and after some re-arranging allow to recast equation (2.28) as

$$\left(i\omega^* V + \frac{\partial \boldsymbol{R}_f}{\partial \boldsymbol{q}_f}\right)\hat{\boldsymbol{q}}_f = -\left[\frac{\partial \boldsymbol{R}_f}{\partial \boldsymbol{x}} + i\omega^*\left(\frac{\partial \boldsymbol{R}_f}{\partial \dot{\boldsymbol{x}}} + \overline{\boldsymbol{q}}_f\frac{\partial V}{\partial \boldsymbol{x}}\right)\right]\hat{\boldsymbol{x}} \tag{2.30}$$

since it can be shown that the temporal derivative of the volume matrix $\frac{\mathrm{d}V}{\mathrm{d}}$ is only dependent on the grid-node location. The reduced frequency is defined as

$$\omega^* = \frac{2\pi f l_{\mathrm{ref}}}{U_\infty} \tag{2.31}$$

where U_∞ and l_{ref} are the freestream velocity and the reference length, respectively. The $\frac{\partial \boldsymbol{R}_f}{\partial \boldsymbol{x}}$ and $\frac{\partial \boldsymbol{R}_f}{\partial \dot{\boldsymbol{x}}}$ terms on the right-hand side of equation (2.30) denote the changes

in the residual due to mesh deformation and mesh point velocities, respectively. These matrices along with $\frac{\partial V}{\partial \boldsymbol{x}}$ are not explicitly built since only the result of the matrix vector product with the complex valued $\hat{\boldsymbol{x}}$ is required. Since the latter grid deformation is predetermined, these terms are evaluated using central finite differences in a standard LFD simulation. Lastly, the flux Jacobian $\frac{\partial \boldsymbol{R}_f}{\partial \boldsymbol{q}_f} = A_{ff}$ has been obtained in the context of the discrete adjoint method by analytically differentiating the TAU code [111] and will be used in the following sections.

2.5 Global Stability Analysis

If no external excitation is included, and we are interested in the stability of the flow to small amplitude disturbances, the decomposition reads

$$\boldsymbol{q}_f = \overline{\boldsymbol{q}}_f + \epsilon \boldsymbol{q}'_f(t), \qquad \epsilon \ll 1 \tag{2.32}$$

Substituting this into equation (2.26) and applying a Taylor expansion around the equilibrium point, while neglecting $\mathcal{O}(\epsilon^2)$ and higher order terms, we arrive at

$$\frac{\mathrm{d}V \boldsymbol{q}'_f}{\mathrm{d}t} + \boldsymbol{R}_f(\overline{\boldsymbol{q}}_f) + \frac{\partial \boldsymbol{R}_f}{\partial \boldsymbol{q}_f} \boldsymbol{q}'_f = 0 \tag{2.33}$$

Similar to the LFD analysis, we assume that the steady state $\boldsymbol{R}_f(\overline{\boldsymbol{q}}_f)$ is negligibly small. Considering a periodic solution with a complex frequency λ which is inhomogenous in three spatial directions, the system is transferred to the frequency domain

$$\boldsymbol{q}'_f(x,y,z,t) = \sum_{n_h=1}^{\infty} \hat{\boldsymbol{q}}_f(x,y,z) e^{i n_h \lambda t} \qquad \hat{\boldsymbol{q}}_f \in \mathbb{C} \tag{2.34}$$

leading to a system of the form

$$\left(i\lambda V + \frac{\partial \boldsymbol{R}_f}{\partial \boldsymbol{q}_f} \right) \hat{\boldsymbol{q}}_f = 0 \tag{2.35}$$

This allows the system to be written as a matrix eigenvalue problem i.e.

$$J \hat{\boldsymbol{q}}_f = \lambda \hat{\boldsymbol{q}}_f \qquad \text{where} \qquad J = -\frac{\partial \boldsymbol{R}_f}{\partial \boldsymbol{q}_f} \tag{2.36}$$

where $\hat{\boldsymbol{q}}_f$ and λ are the eigenvector and eigenvalue respectively. The eigenvalue is of the form $\lambda = \sigma + \omega i$ with σ describing the growth or decay rate and ω the angular oscillation frequency. Systems governed by the Navier–Stokes equations are usually described by fold and Hopf bifurcations. Specifically, the system is considered globally unstable when an eigenvalue of the Jacobian matrix resulting from the system discretization has a positive growth rate σ for given flow conditions [88]. Since the resulting J is large and sparse, direct solution methods for eigenvalue computation require vast amounts of memory and therefore one has to result to iterative methods.

Krylov methods are projection processes that create subspaces spanned by vectors of the form $p(J)u$ where p is a polynomial according to

$$\mathcal{K}_m(J, u) = span\{u, Ju, J^2u, ..., J^{m-1}u\} \tag{2.37}$$

The Arnoldi iteration [112] is an eigenvalue algorithm used to approximate a few relevant eigenvalues and eigenvectors of a large matrix of size $n \times n$, by projecting the matrix into a Krylov subspace of size m where $n > m$. Herein, n is given by the product of the number of the state vector variables times the number of discretization points. By using the Gram–Schmidt procedure, the resulting subspace has an orthonormal basis, allowing the original matrix to be expressed as

$$\underset{(n\times n)}{J}\ \underset{(n\times m)}{Q} = \underset{(n\times m)}{Q}\ \underset{(m\times m)}{H} \tag{2.38}$$

where Q is a matrix containing the orthonormalised vectors as columns and H is an upper Hessenberg matrix. The considerably smaller size of H allows the employment of standard methods for computing its eigenvalues. The eigenvalues and eigenvectors of H are termed the Ritz eigenvalues and eigenvectors, respectively, and they converge to the eigenvalues and eigenvectors of J as the size of the Krylov subspace increases. Nevertheless, since the resulting matrices of the decomposition are dense, methods to keep the subspace size to a minimum without affecting the accuracy of the approximation were developed to complement the Arnoldi decomposition. The implicitly restarted Arnoldi method (IRAM) [113] uses the QR decomposition of the Hessenberg matrix in order to create a polynomial that essentially filters out the unwanted (or spurious) parts of the spectrum. While the original Arnoldi method is very successful in finding eigenvalues that have large magnitude and are well separated, its limitations become

evident when applied to problems where the physically relevant eigenvalues are small in magnitude and clustered. To tackle this problem, spectral transformation methods need to be used. The shift-invert strategy is used to search for eigenvalues in specific parts of the spectrum, defined by the user specified shift ζ. In contrast to equation (2.36), the transformed problem that is solved is

$$\mathcal{C}\hat{\boldsymbol{q}}_f = \mu\hat{\boldsymbol{q}}_f \quad \text{where } \mathcal{C} = (J - \zeta I)^{-1} \text{ and } \mu = \frac{1}{\lambda - \zeta} \tag{2.39}$$

from which it can be seen that the largest eigenvalues of $\mathcal{C}$ correspond to the smallest eigenvalues of J close to the shift ζ. Matrix $\mathcal{C}$ does not need to be formed explicitly, since only its action on a vector needs to be approximated. This is achieved by using an iterative solver, leading us to the so called inner-outer iterative methods. The choice of the inner iterative solver is case-dependent. For more information regarding iterative methods the reader is referred to [114].

2.6 Global Nonmodal Stability Analysis

Global stability analysis deems a system stable or unstable according to the concept of Lyapunov stability. This implies that when a system in equilibrium is perturbed, it will either return to its original state if deemed stable and conversely depart from that state if deemed unstable. In both scenarios, an infinite time horizon is allowed for the system to return to that equilibrium state. Consequently, the local fluid processes that are characterised by many time scales in fluid systems cannot be thoroughly examined [7]. Therefore, to assess the stability of the system over a finite time interval, the transient energy amplification of an initial condition over that time interval needs to be measured. Mathematically, the maximum optimal energy amplification optimised over all initial conditions can be written as

$$G(t) = \max_{\boldsymbol{q}'_{f_0}} \frac{E(\boldsymbol{q}'_f(t))}{E(\boldsymbol{q}'_{f_0})} \tag{2.40}$$

where $E(\boldsymbol{q}'_f(t))$ is the time-dependent energy of the perturbation $\boldsymbol{q}'_f$. In order to calculate the energy of linear perturbations for a given time, we need to recast equation (2.36) as an initial value problem of the form

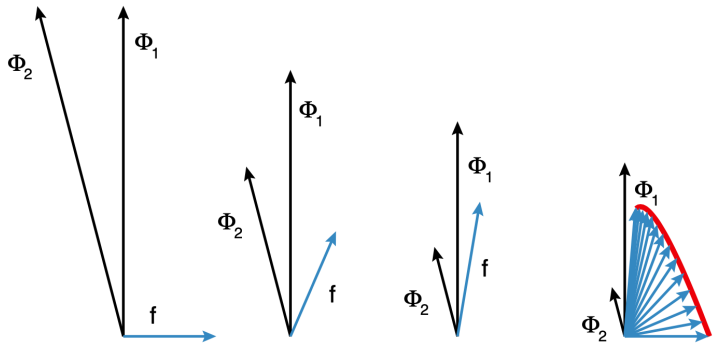

FIGURE 2.1. Geometric interpretation of transient growth (taken from [7]).

$$\frac{\partial}{\partial t}\boldsymbol{q}'_f = J\boldsymbol{q}'_f \tag{2.41}$$

where the exact solution can be written by using the matrix exponential [115, 116]

$$\boldsymbol{q}'_f(t) = \boldsymbol{q}'_f(0)e^{Jt} = \boldsymbol{q}'_f(0)\Psi(t) \tag{2.42}$$

where Ψ is known as the propagator operator [117]. In the case of a normal matrix or operator, the eigenvalues resulting from the global stability analysis would be adequate to describe the energy evolution of a perturbation since it would decrease or increase monotonically for a stable or unstable system, respectively. Linear operators resulting from the discretization of the Reynolds–Averaged Navier–Stokes equations demonstrate high non-normality, and can therefore sustain transient energy growth at short times before decaying, even for a stable system. This can be better interpreted geometrically, as shown in figure 2.1. When two eigenvectors of a system Φ_1 and Φ_2 are non-orthogonal, the superposition during their decay can produce transient growth in the norm of the vector f, that denotes their difference [118].

Transient energy growth

To measure the transient growth of a perturbation, a relation between the energy norm $\|\cdot\|_E$ and the standard (Euclideian) L_2-norm $\|\cdot\|_2$ is needed. For a vector this is given by

$$\begin{aligned} E(\boldsymbol{q}'_f) = \|\boldsymbol{q}'_f\|_E &= \langle \boldsymbol{q}'_f, \boldsymbol{q}'_f \rangle_E = {\boldsymbol{q}'_f}^H \mathcal{Q}\boldsymbol{q}'_f \\ &= {\boldsymbol{q}'_f}^H \mathcal{F}^H\mathcal{F}\boldsymbol{q}'_f = \langle \mathcal{F}\boldsymbol{q}'_f, \mathcal{F}\boldsymbol{q}'_f \rangle_2 = \|\mathcal{F}\boldsymbol{q}'_f\|_2 \end{aligned} \tag{2.43}$$

where $\mathcal{Q}$ is a weighting matrix that is positive definite and therefore has a Cholesky decomposition as $\mathcal{Q} = \mathcal{F}^H\mathcal{F}$. In the incompressible regime, this norm is a direct mea-

surement of the kinetic energy of the perturbation [13,119] something not as straightforward for compressible cases. In the case of the latter, the norm proposed by Mack [120] and Chu [121] has been used in recent literature where compressible flows are examined [15, 122]. However, since there are no studies on transient growth in steady turbulent flows to the authors knowledge, the norm used in other studies at similar conditions [90] or ones that also deal with pseudospectra analysis [123] at similar flow regimes is adapted herein [14, 93]. This assumes $\mathcal{Q} = V$ where V is the volume matrix from equation (2.26). The equivalent of equation (2.43) in the case of a matrix $\mathcal{L}$ is given by

$$\|\mathcal{L}\|_E = \max_{\boldsymbol{q}'_{f_0}} \frac{\|\mathcal{L}\boldsymbol{q}'_f\|_E}{\|\boldsymbol{q}'_f\|_E} = \max_{\boldsymbol{q}'_{f_0}} \frac{\|\mathcal{F}\mathcal{L}\mathcal{F}^{-1}\boldsymbol{q}'_f\|_2}{\|\mathcal{F}\boldsymbol{q}'_f\|_2} = \|\mathcal{F}\mathcal{L}\mathcal{F}^{-1}\|_2 \tag{2.44}$$

demonstrating that in the case of matrices, the Cholesky factor $\mathcal{F}$ relates the energy norm to the L_2-norm [7]. Having defined the energy norm, we arrive at the equation for the gain function $G(t)$ by substituting equation (2.42) into (2.40)

$$G(t) = \max_{\boldsymbol{q}'_{f_0}} \frac{\|\boldsymbol{q}'_f(t)\|_E^2}{\|\boldsymbol{q}'_{f_0}\|_E^2} = \max_{\boldsymbol{q}'_{f_0}} \frac{\|\boldsymbol{q}'_{f_0} e^{Jt}\|_E^2}{\|\boldsymbol{q}'_{f_0}\|_E^2} = \|e^{Jt}\|_E^2 = \|\mathcal{F}\Lambda\mathcal{F}^{-1}\|_2^2 \tag{2.45}$$

where

$$\Lambda = diag(e^{-i\lambda t_1}, e^{-i\lambda t_2}, ..., e^{-i\lambda t_n}) \tag{2.46}$$

The maximum gain optimised over all initial conditions for a given time t is obtained by the square of the largest singular value, after the singular value decomposition (SVD) of equation (2.45) [124, 125]. For a matrix $\mathcal{C} = \mathcal{F}\Lambda\mathcal{F}^{-1}$ the singular value decomposition has the form

$$\mathcal{C}V = U\Sigma \tag{2.47}$$

where V and U are unitary matrices and Σ is a diagonal matrix containing the singular values in descending order, i.e. $\sigma_1 \geq \sigma_2 \geq \ldots \sigma_N$ and therefore the maximum gain is given by ${\sigma_1}^2$. Apart from the gain at each time of interest, the associated optimal transient growth modes, namely the optimal initial condition (denoted OIC) and optimal response (denoted ORE), need to be obtained. These are given by extracting the principal column vectors of V and U, respectively, and expressing them in the eigenvector basis by the use of the Cholesky factor as

$$v_{OIC} = \mathcal{F}v_1 \qquad \text{and} \qquad u_{ORE} = \mathcal{F}u_1 \tag{2.48}$$

In summary, to calculate the gain and the associated optimal transient growth modes for a given time, the computational steps are as follows. Firstly, provided that an eigenvalue decomposition of the Jacobian has been obtained (usually with some iterative method), a Cholesky decomposition of the weighting matrix given by the inner product definition is performed. In practice, this is achieved by performing an SVD once, using the orthonormal (since they result from the Gram-Schmidt orthogonalization of the Arnoldi method) eigenvectors from the eigendecomposition of the Jacobian along with the weighting matrix. Since the latter is positive definite then that SVD simplifies to the Cholesky decomposition. Secondly, by using the Cholesky factors, an SVD of the matrix exponential is computed for each time of interest. Finally, the gain and the optimal transient growth modes are obtained from the matrices of the factorization.

Computation of the matrix exponential

There are different approaches for the calculation of the matrix exponential [115, 116] as part of the transient growth computation. The most straightforward approach, would be to evaluate equation (6.1) for each point in time using time-stepping. In the context of transient growth, the system is marched forward in time using the linear operator J followed by a backwards in time integration using the adjoint J^* until convergence [126, 127]. While this method converges to the maximum $G(t)$ for each point in time, it is unknown when that maximum will occur. Therefore, even when only the transient behaviour is sought, one has to integrate for long time intervals multiple times. The benefit of avoiding matrix-forming methods is outweighed by the computational time that also increases with the complexity of the flow and consequently the method presented next is used in the present work. Details of a time-stepping approach developed in this work but not implemented due to long running times can be found in Appendix B. The eigenvalue decomposition of the matrix can be used for the computation of the matrix exponential according to

$$e^{Jt} = e^{\mathcal{D}\Lambda\mathcal{D}^{-1}} = \mathcal{D}e^{\Lambda t}\mathcal{D}^{-1} \tag{2.49}$$

where $\mathcal{D}$ is a unitary matrix containing the corresponding eigenvectors and Λ is given in equation 2.46. In comparison to the time-stepping approach, this method allows for the evaluation of multiple timesteps after an eigenvalue decomposition that is performed once. Nevertheless, the definition of an appropriate subspace size requires increasing the size until the addition of extra modes has a negligible effect on the gain output. Furthermore, in the case of a large and sparse J it is straightforward to employ the decomposition from equation 2.38 in order to create a smaller yet representative system that can be solved with direct methods. The approximation to the matrix exponential

using the Arnoldi decomposition can be written as

$$e^{Jt} \approx Qe^{Ht}Q^H = Q\mathcal{U}e^{\mathcal{R}t}\mathcal{U}^{-1}Q^H \tag{2.50}$$

where $\mathcal{U}$ and $\mathcal{R}$ are the matrices of the Ritz eigenvectors and Ritz eigenvalues respectively [118]. Nevertheless, when using software such as MATLAB or libraries like SciPy, that are based on IRAM, to compute a subset of the eigenspectrum, the output obtained is the eigenvalues and the associated right eigenvectors, instead of the orthonormal basis and the Hessenberg matrix i.e. the product $Q\mathcal{U}$ and $\mathcal{R}$ instead of Q and H in equation (2.50). This has a direct implication on the eigendecomposition of the matrix in equation (2.49). Assume the eigendecomposition of a normal (or symmetric) matrix A of the form $A = \mathcal{D}\Lambda\mathcal{D}^{-1}$. It is straightforward to deduce that the columns of $\mathcal{D}$ are the right eigenvectors of A and the rows of $\mathcal{D}^{-1}$ are the left eigenvectors, respectively. In that case, the right eigenvectors are sufficient to complete the decomposition, since for such matrices $\mathcal{D}^{-1} = \mathcal{D}^T$ or $\mathcal{D}^{-1} = \mathcal{D}^*$ for complex eigenvectors, since the global modes form an orthogonal basis. Conversely, this is not the case for nonnormal matrices which have nonorthogonal eigenvectors. To overcome this difficulty, a dual basis is introduced which is made with the inclusion of the adjoint modes [128]. Together with the global modes these form a bi-orthogonal basis, where two vectors d and d' that represent a global and an adjoint mode, respectively, have the condition $\langle d_i \ , \ {d_j}' \rangle = \delta_{ij}$. In addition, it is known that the right eigenvectors of the adjoint matrix correspond to the left eigenvectors of the original matrix and vice versa. Hence, if the complete set of eigenvectors was to be used then the adjoint eigenvectors could also be computed by inverting the square matrix of right eigenvectors or by computing the left eigenvectors of the original matrix, apart from directly operating on the adjoint matrix. Herein, since IRAM only computes a subset of the right eigenvectors which in return form a rectangular matrix, one needs to operate on the adjoint matrix to be able to form the bi-orthogonal basis. Therefore, to form the correct eigendecomposition with iterative methods in equation (2.50), the term $\mathcal{U}^{-1}Q^H$ is substituted with the transposed right eigenvectors of J^*.

2.7 Coupled Aeroelastic Formulation

Structural dynamics and can be described by a mass-spring-damper model. The second order differential equations of motion that govern this system are given by

$$M\ddot{\boldsymbol{x}} + D\dot{\boldsymbol{x}} + K\boldsymbol{x} = \boldsymbol{f}_a(t) \tag{2.51}$$

where M,D and K denote the mass, damping and stiffness matrices, respectively, and $\boldsymbol{f}_a$ is the generalised aerodynamic force vector. Since the structural coordinates $\boldsymbol{x}$ resulting

from a finite element model (FEM) are in the order of several hundreds of thousands, the structural behaviour used herein is modelled using a modal structural approach. This is achieved by computing the eigenvalues and eigenvectors of equation (2.51) while neglecting the damping and aerodynamic forcing terms. As a result, the physical coordinates $\boldsymbol{x}$ of the linear structural model relate to the mode shapes and modal amplitudes as

$$\boldsymbol{x}(t) = \Xi\boldsymbol{\eta}(t) \tag{2.52}$$

where $\Xi = [\boldsymbol{\xi}_1, \boldsymbol{\xi}_2, \ldots, \boldsymbol{\xi}_m]$ is the matrix containing the m leading normal mode shapes chosen based on frequency of physical relevance. Substituting equation (2.52) in (2.51) and neglecting structural damping yields the equations of the structural system in modal coordinates as

$$\Xi^T M \Xi\ddot{\boldsymbol{\eta}} + \Xi^T K \Xi\boldsymbol{\eta} = \Xi^T \boldsymbol{f}_a \tag{2.53}$$

Equation (2.53) can be rewritten as a first order ordinary differential equation as

$$\frac{\mathrm{d}\boldsymbol{q}_s}{\mathrm{d}t} = -\boldsymbol{R}_s(\boldsymbol{q}_s, \boldsymbol{q}_f) \tag{2.54}$$

where $\boldsymbol{q}_s = [\boldsymbol{\eta}^T, \dot{\boldsymbol{\eta}}^T]^T$. The structural residual vector $\boldsymbol{R}_s$ is

$$\boldsymbol{R}_s(\boldsymbol{q}_s, \boldsymbol{q}_f) = \begin{bmatrix} 0 & I \\ -\mathcal{M}^{-1}\mathcal{K} & 0 \end{bmatrix} \boldsymbol{q}_s + \begin{pmatrix} 0 \\ \Xi^T \boldsymbol{f}_a \end{pmatrix} \tag{2.55}$$

allowing the transformation of equation (2.54) into the frequency domain as

$$(A_{ss} - i\omega^* I)\hat{\boldsymbol{q}}_s = \hat{\boldsymbol{b}}_s \tag{2.56}$$

where the structural Jacobian matrix is defined as

$$A_{ss} = \begin{bmatrix} 0 & I \\ -\mathcal{M}^{-1}\mathcal{K} & 0 \end{bmatrix} \tag{2.57}$$

and $\hat{\boldsymbol{b}}_s = (0, \Xi^T \hat{\boldsymbol{f}}_a)^T$ is the aerodynamic harmonic excitation projected onto the structural modes and $\mathcal{M} = \Xi^T M \Xi$, $\mathcal{K} = \Xi^T K \Xi$. If we consider that the structural excitation in equation (2.26) is given by equation (2.54), then we obtain

$$\frac{\mathrm{d}V\boldsymbol{q}_f}{\mathrm{d}t} = -\boldsymbol{R}_f(\boldsymbol{q}_f, \boldsymbol{q}_s) \tag{2.58}$$

which when coupled with equation (2.26) yields

$$\frac{\mathrm{d}V\boldsymbol{q}}{\mathrm{d}t} = -\boldsymbol{R}(\boldsymbol{q}) \tag{2.59}$$

where $\boldsymbol{q} = [\boldsymbol{q}_f^T, \boldsymbol{q}_s^T]^T$ is the state vector for both the aerodynamic and structural system. The diagonal cell volume has been padded with an identity matrix for the modal structural degrees of freedom, but the same symbol V is used for ease of notation. By linearising around the equilibrium point using a Taylor expansion, we arrive at

$$V\frac{\mathrm{d}\boldsymbol{q}}{\mathrm{d}t} + \boldsymbol{R}(\boldsymbol{q}) + \frac{\partial \boldsymbol{R}}{\partial \boldsymbol{q}}\boldsymbol{q} = 0 \tag{2.60}$$

where $\boldsymbol{R}(\boldsymbol{q})$ is the coupled steady state residual and the term $\boldsymbol{q}\frac{\mathrm{d}V}{\mathrm{d}t}$ is part of the coupled Jacobian $\frac{\partial \boldsymbol{R}}{\partial \boldsymbol{q}}$ for brevity. By assuming harmonic response, equation (2.60) can be transferred to the frequency domain, yielding

$$\left(\frac{\partial \boldsymbol{R}}{\partial \boldsymbol{q}} - i\omega^* V\right)\boldsymbol{q} = \hat{\boldsymbol{b}} \tag{2.61}$$

where $\hat{\boldsymbol{b}}$ is the forcing term. Finally, matrix A can be written as

$$A = \begin{bmatrix} \frac{\partial \boldsymbol{R}_f}{\partial \boldsymbol{q}_f} & \frac{\partial \boldsymbol{R}_f}{\partial \boldsymbol{q}_s} \\ \frac{\partial \boldsymbol{R}_s}{\partial \boldsymbol{q}_f} & \frac{\partial \boldsymbol{R}_s}{\partial \boldsymbol{q}_s} \end{bmatrix} = \begin{bmatrix} A_{ff} & A_{fs} \\ A_{sf} & A_{ss} \end{bmatrix} \tag{2.62}$$

where A_{ff} and A_{ss} are the fluid and structural Jacobians, respectively, and A_{sf} and A_{fs} are coupling matrices. The coupled system matrix in equation 2.62 is arranged in block matrix form, the dimensions of which are given by the number of unknowns of A_{ff} and A_{ss} $(n_f + n_s + 1)$. Consequently, the dimensions of A_{sf} and A_{fs} are such so the matrices are conformable [129]. Matrix A_{fs} illustrates the dependence of the fluid residual on the structural unknowns and is , whereas matrix A_{sf} describes how the structure responds to changes in the flowfield by projecting the generalised aerodynamic force onto the structural modes.

2.8 Practical Implementation Details

The finite-volume solver TAU [130], developed by the German Aerospace Centre (DLR) and employed both in industry and academia, is used for the simulations presented herein. The compressible, three-dimensional steady and unsteady RANS equations are solved in TAU for unstructured or hybrid grids. Different turbulence models are

available through the code, including one- and two-equation eddy viscosity models, second-order closures such as the Reynolds stress transport model as well as LES and DES models. Pre-processing, grid deformation and grid adaptation modules are also included the package [131]. The pre-processing module is used for constructing a dual grid of control volumes (cell-vertex scheme) from the initial grid which can be composed of tetrahedral, prismatic, hexahedral or pyramidal elements, and to allow mesh partitioning for parallel computations [132].

As mentioned earlier, the negative Spalart–Allmaras one-equation turbulence model is used consistently for closure in the studies of this thesis (in the cases where fully turbulent flow is assumed) and is discretised with a first-order upwind scheme. Previous work [6,11,56,91] has shown that the shock buffet phenomenon is sensitive to the change in eddy-viscosity levels that depend on the discretisation of the turbulence model and the turbulence model variant (in particular the use of a compressibility correction to the SA model [133]). Therefore, the current choice was selected as it has been shown in previous simulations that it captures shock buffet unsteadiness more accurately compared to a second-order scheme where shock-buffet was not present along with lower amplitude lift and drag signals [6]. The compressibility correction mentioned has also been added in previous work [11, 44], but is not used herein. This correction decreases the eddy-viscosity levels, which results in an earlier onset of the instability [134]. The Green–Gauss theorem is used for reconstructing the exact gradients used for viscous and source terms in the turbulence model. Regarding temporal discretisation, an implicit backward Euler solver with lower-upper Symmetric–Gauss–Seidel iterations [135] and local pseudo-time-stepping converges the non-linear flow equations to steady state. Additionally, geometric multigrid on three grid levels is employed to accelerate convergence. All steady solutions presented herein converged by at least ten orders of magnitude.

Implementation details of the LFD system are discussed next. Since the formation of the right-hand side in equation 2.30 using finite differences has been described, the solution of the linearised system following the formation of the hand-differentiated fluid Jacobian needs to be addressed. For the LFD analysis, the RANS equations (plus turbulence model) are first discretised in space and then linearised about the steady-state base flow. This approach, allows for the computation of the large but sparse matrix even for complex test cases. Due to the large size of the system, a direct matrix inversion method would require vast memory requirements, thus sparse iterative solvers need to be employed. Herein, a block incomplete lower-upper (ILU) factorization with zero fill-in preconditions the chosen Krylov sparse iterative linear solver; specifically a generalized conjugate residual solver with deflated restarting (GCRO-DR) is used, since it has demonstrated better performance than the generalised minimal residual approach

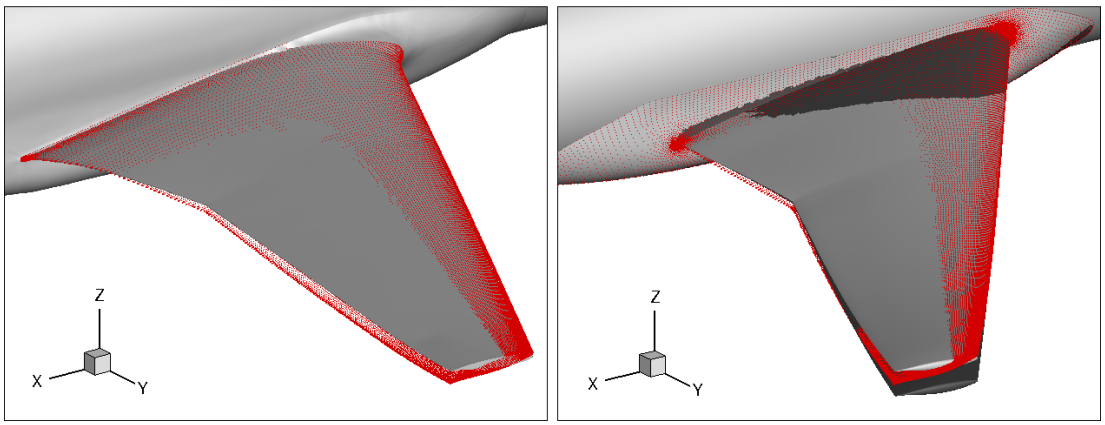

FIGURE 2.2. Illustration of wing deformation due to synthetic torsion mode for an amplitude factor of $\boldsymbol{q}_0 = 10$ for both aircraft test cases RBC12 (left) and CRM (right) with jig shape (dark gray) and statically deformed wing.

(GMRES) commonly used [136]. This solver has been scrutinised previously both for an aerofoil and a wing in edge-of-the-envelope flow conditions [110, 137]. For the LFD results presented herein, the grid is deformed according to a synthetic torsion mode shown in figure 2.2. The mode resembles a typical wing torsional deformation with the axis of rotation located approximately at the quarter-chord line but the mode itself is not based on a finite-element analysis of the actual wing structure. The deformation of the wing is zero at the root while increasing linearly towards the wing tip [94]. The maximum deflection is equal the amplitude factor $\boldsymbol{q}_0$, i.e. for $\boldsymbol{q}_0 = 1$ there will be a twist angle of 1° at the wing tip. The forced sinusoidal pitching motion is defined as

$$\boldsymbol{q}'(t) = \boldsymbol{q}_0 \sin(\omega^* t) \tag{2.63}$$

The FlowSimulator environment [138] is used for the unsteady time-marching simulations. This software enables computational fluid dynamics enhanced multidisciplinary simulations on massively parallel computing systems while providing a plug-in environment where different computational fluid dynamics tools and developer scripts can be utilised [139]. Specifically, in the case of the time-accurate harmonic forcing simulations, the FS Forced Motion module is employed. This technique, prescribes an elastic, time-dependent deformation of the wing (mode shape) in an unsteady CFD simulation, without performing a fluid-structure coupling step [140]. It is commonly used to force a test case using the shape of a known structural eigenmode at selected frequencies and magnitudes, for a certain number of periods. However, the mode shape does not necessarily need to result from a vibration analysis of a FEM model, such as the one in figure 2.2. For the harmonic forcing study conducted herein, the same synthetic torsion mode used for the LFD simulations was applied. The dual time-stepping com-

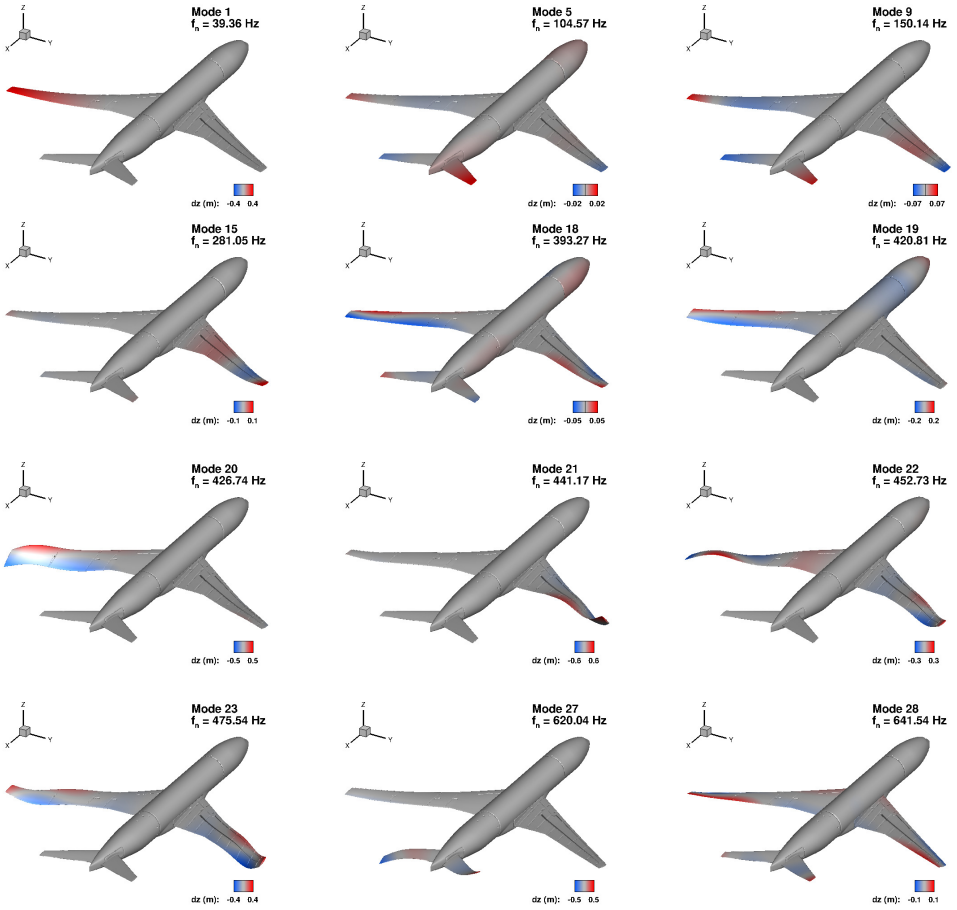

FIGURE 2.3. Representative normal mode shapes from wind-off vibration analysis, with mass-normalised eigenvectors scaled by a factor of 0.1 for visualisation purposes. Surface colours describe modal deformation in z-direction.

bined with the second-order backward differentiation formula for the integration of the aerodynamic equations employed in DLR-TAU is given by

$$\boldsymbol{R}^* = \boldsymbol{R}(\boldsymbol{q}, \boldsymbol{x}, \dot{\boldsymbol{x}}) + \frac{3(V\boldsymbol{q})^{n+1} - 4(V\boldsymbol{q})^n + (V\boldsymbol{w})^{n-1}}{2\Delta t} \tag{2.64}$$

where Δt is the time step. The discrete control volumes are time-dependent observing the geometric conservation law.

Finally, as mentioned in section 2.7, the structural deformations in the coupled aeroelastic simulation rely on a modal approach where a structural model is constructed by using an appropriate number of modes resulting from a vibration analysis of a FEM model. These are selected accordingly to be able to capture all dominant structural features such as first and second bending and torsion modes, tail modes and fuselage bending. A vacuum analysis that was performed on the FEM of the CRM, obtained the structural modes, 30 of which are kept for the aeroelastic study herein and are available at the CRM website [141]. Usually, these modes are have symmetrical shapes, but in

the present case, the different cut-outs made in each wing to fit various instrumentation resulted in a small weight imbalance between both sides and therefore in anti-symmetric structural modes at lower frequencies. Some representative modes and their frequencies are shown in figure 2.3, where the mass-normalised eigenvectors have been scaled by a factor of 0.1 for visualisation purposes. Generally, the coordinate systems describing the structural and the aerodynamic system are not the same, since one results from the FEM discretisation and the other from the CFD mesh points ($\boldsymbol{x} \neq \boldsymbol{x}_s$). Thus, a pre-processing step that interpolates the structural excitations Ξ onto the CFD surface mesh points is required to create the coordinate connection required to solve the coupled aeroelastic system in equation (2.59). Lastly, the coupled system is solved using a subiteration level scheme for the data exchange between the aerodynamic and structural system. Similar to the other time-marching simulations, the aerodynamic system is solved using equation (2.64) although now this is followed with the update of the structural system by using the Newmark-beta integration scheme [142].

Chapter 3

Test Cases

In this chapter the test cases used in the present work are introduced. Geometry and mesh size details are given alongside relevant experimental and numerical work information pertaining to shock buffet studies on these cases. The aerofoil test case is used in the transient growth study, whereas the half-wing models of the large civil aircraft cases are used in the harmonic forcing and fluid-structure interaction studies. Finally, the steady-states that are the starting point for all simulations and analyses conducted herein are presented.

3.1 ONERA OAT15A Aerofoil

Supercritical aerofoils were developed to improve drag divergence Mach numbers while maintaining acceptable performance of maximum lift and stall at low speeds [143]. The shape of such aerofoils is characterised by a larger leading edge, a flat middle section on the upper surface and highly cambered lower surface close to the trailing edge. Specifically, the effect of the flat section is a weakening of the shock that results in reduced wave drag [144].Additionally, the increased length of the flat section, allows for a more gradual deceleration of the airflow. This results in a relatively isentropic deceleration that consequently minimises the energy losses associated with the shockwave and further contributes to the reduction of wave drag [143]. The OAT15A supercritical aerofoil shown in figure 3.1 is a geometry extensively studied both experimentally and numerically. Specifically, wind tunnel tests have focused both on characterising the shock-buffet phenomenon on the geometry [38, 145], using precision methods such as high-speed schlieren cinematography and laser Doppler velocimetry alongside conven-

tional equipment, as well as investigating the potential of both active and passive flow control [146]. On the numerical side, various levels of turbulence modelling have been employed, namely URANS [49,55,147], ZDES [55,145] and LES [42] along with studies focusing on the stability and receptivity of shock buffet [14, 92]. The model, that was tested in the S3Ch ONERA transonic wind tunnel [38], has a 12.3% thickness-to-chord ratio, a span of 0.78 m and a chord of 0.23 m, resulting in an AR of approximately 3.4. The thickness of the trailing edge is 0.5% of the chord. In the experiments, transition of the boundary-layer was achieved by using a carborundum strip located at $X/c = 0.07$ on the upper and lower surfaces [38].

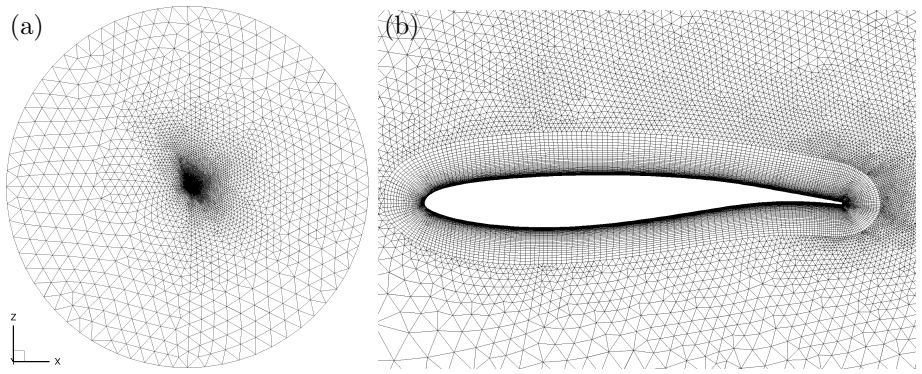

FIGURE 3.1. Farfield view (a) with radius of 100 chord lengths and approximately 35000 points and close-up (b) of the OAT15A aerofoil hybrid grid showing the structured mesh region close to the surface.

The aerofoil has the typical characteristics of a supercritical geometry, with a larger leading edge, a flat middle section on the upper surface and highly cambered lower surface close to the trailing edge. The two-dimensional circular domain shown in figure 3.1(a) has a radius of 100 chord lengths and is discretised by approximately 35000 points. No-slip boundary condition is imposed at the viscous walls. The hybrid mesh used, results in $y^+ < 1$ in the structured boundary-layer region shown in figure 3.1(b) whereas an unstructured mesh extends up to the farfield boundary. Although the wind tunnel tests [38] were run for different combinations of Mach numbers and angles of attack, the shock buffet conditions considered in numerical studies are for a Mach number of 0.73 and a Reynolds number of 3.2×10^6. At these conditions, a spectral bump first appears in the pressure fluctuations for an angle of attack of 3°. The shock buffet onset occurs for an incidence of 3.5°, even though the spectral content of the instability is evident when the angle of attack is at 3.25°. At these conditions the shock oscillates at a frequency of 69 Hz [14]. The base flow presented in figure 3.2 shows the lambda pattern of the shock formed where the end of the supersonic region coincides with the recirculation bubble.

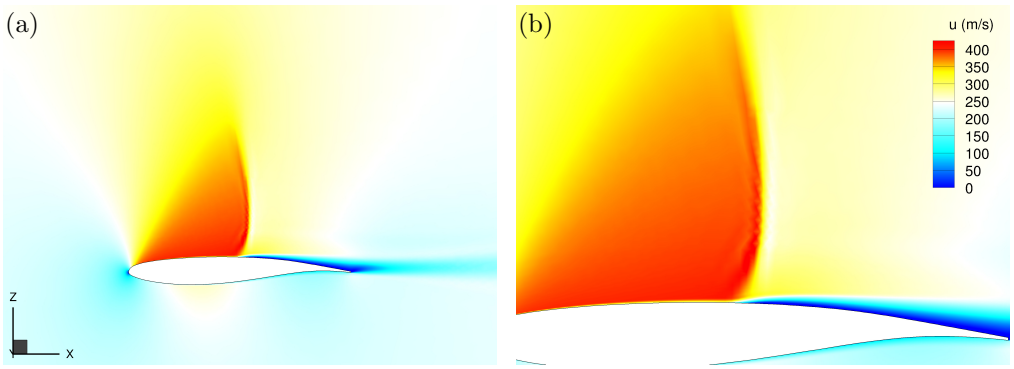

FIGURE 3.2. Streamwise velocity field of the OAT15A base flow (a) and close-up of the lambda shock (b), for buffet-onset angle of attack $\alpha = 3.5°$ at conditions: $Re = 3.2 \times 10^6$, $M_\infty = 0.73$

3.2 RBC12 Model

The RBC12 half-model, is a wing-fuselage model wind-tunnel model, representative of a typical commercial aircraft designed in the 1970/80s. The configuration has been extensively used for the investigation of shock buffet, especially as part of the European Clean Sky project BUCOLIC (BUffet COntroL of transonIC Wings) in the Aircraft Research Association (ARA) Transonic Wind Tunnel (TWT). To assess the efficacy

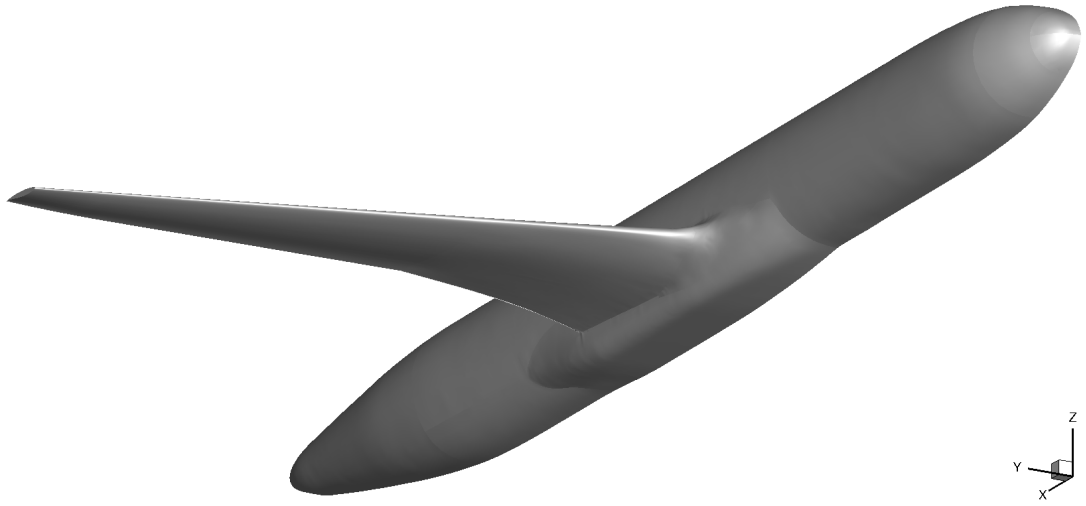

FIGURE 3.3. Computer-aided design model of the RBC12 half-wing configuration.

of different instrumentation in predicting the instability onset, a variety of equipment was used in the experimental campaigns including dynamic pressure sensitive paint that provided a plethora of valuable information on the flow characteristics [77, 96]. Passive flow control has also been investigated for the RBC12 [148]. Numerically, scale-resolving DDES simulations [97, 149] and RANS-based simulations [84] have shown excellent agreement with experimental data. Studies examining the effect of Mach

number on shock buffet [85] and the global stability of the phenomenon [94] have also been carried out. The model has a quarter-chord sweep angle of 25°, a reference area of

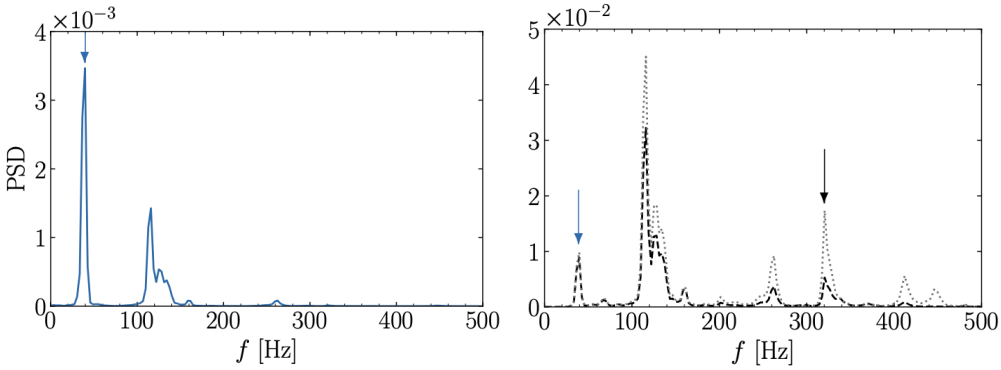

(a) Strain Gauge Response (b) Accelerometer Response

FIGURE 3.4. Wind-on frequency content of the structural response for the RBC12 wind tunnel model, reproduced with permission and adapted from [4]. The dashed and dotted vertical lines (- - - - and ·····) indicate responses from two different accelerometers located at different chordwise stations close to the wing tip.The first bending and first torsion modes are denoted by the blue and the black arrow, respectively.

0.29592 m^2, a mean aerodynamic chord (MAC) of 0.27889 m and a reference semi-span b of 1.0846 m, giving it an aspect ratio of 7.78. The model was mounted on a base plate of 0.019 m in thickness, something that is included in the semi-span length measurement of 1.104 m. The full aircraft dimensions in relation to the wind tunnel model are scaled by a factor of 17.5 and are shown in comparison to modern wide-body airlines in service in table 3.1. The geometry used in the simulations, shown in figure 3.3, was obtained from a combination of laser inspection and coordinate measurement machine (CMM) inspection [77]. The resulting unstructured computational mesh has about 2.7×10^6 points, generated using the Solar mesh generator following industry accepted guidelines. Far-field conditions are applied at a distance of 25 times the semi-span of the model and the symmetry boundary condition is applied along the centre plane.

TABLE 3.1. Characteristics of test cases compared to modern wide-body airliners.

Dimension	RBC12	CRM	A330neo	B777-300
Ref. Area, m^2	181.2	389.76	363.10	427.80
Span m	38.6	59.23	58	60.90
Ref. Chord, m	4.9	7.06	7.26	8.75
25% Chord Sweep, °	25	35	30	31.6
Aspect Ratio	7.78	9	9.26	8.67
Taper Ratio	0.25	0.275	0.251	0.149

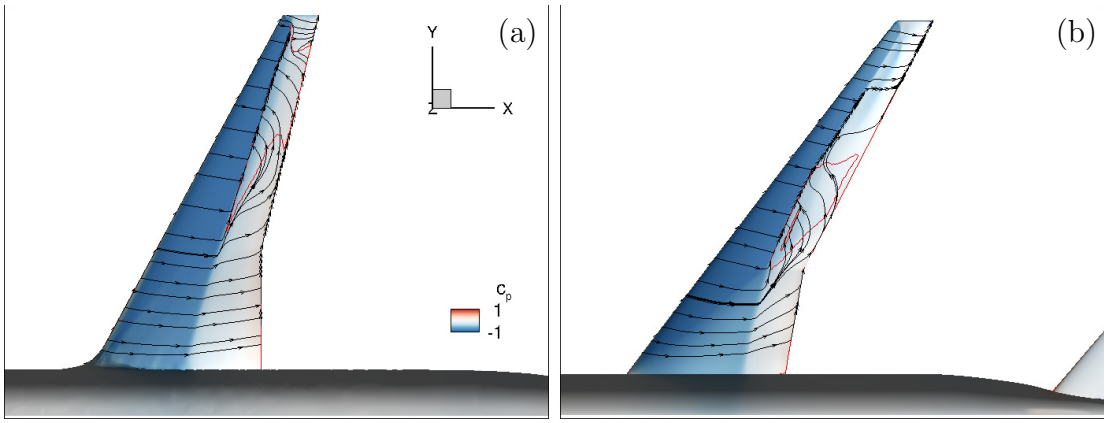

FIGURE 3.5. Steady-state surface pressure coefficient with friction lines for (a) RBC12 at $\alpha = 3°$ and (b) CRM at $\alpha = 3.7°$. The zero skin friction line is highlighted in red.

Amongst the different instrumentation placed on the model, strain gauge and accelerometer measurements were used to define the structural frequencies of the model both at design Mach number and wind-off conditions. At wind-off conditions, the first bending mode was identified at 38 Hz, with higher frequency bending modes reported at 125 and 155 Hz. Additionally, the first torsional modes were found at 328 Hz with the higher frequency, predominantly torsional, modes at 414 and 530 Hz. Similar frequencies to these are also obtained at design conditions for a Mach number of 0.8, a Reynolds number (based on MAC) of 3.75×10^6 and an angle of attack of 0°, as shown in the power spectral density (PSD) graph in figure 3.4. Furthermore, a higher harmonic of the first bending mode can be seen peak at 114 Hz as well as a small peak at 152 Hz associated with the fan passing frequency [77]. At these conditions, the shock buffet onset was reported at an angle of 3° [96]. The steady-state surface pressure distribution with highlighted values of zero skin friction for $\alpha = 3°$ is shown in figure 3.5(a). The separated area behind the shock front extends from the yehudi break towards the wingtip. At these conditions, the lift coefficient (C_L) is 0.57.

3.3 NASA Common Research Model

The NASA Common Research Model is a geometry that comes in various configurations and it was developed with the aim to provide a common testbed for industrial and academic research. These configurations range from variations in the wing geometry, such as high-lift, high-speed or laminar flow wing, to variations in the aircraft components, such as the inclusion of pylons and nacelles. It was first introduced as a blind test-case at the 4$^{\text{th}}$ American Institute of Aeronautics and Astronautics (AIAA) CFD Drag Prediction Workshop (DPW) and has since remained the focus test-case.

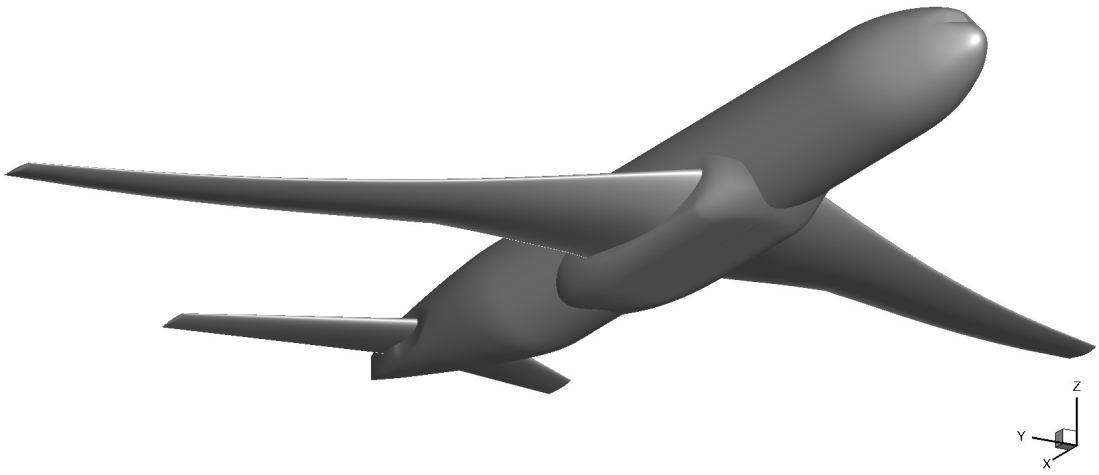

FIGURE 3.6. Computer-aided design model of the NASA CRM wing-body and horizontal tail configuration .

The large deviations of the 5^{th} and 6^{th} AIAA CFD DPW results from the experimental data were attributed to the exclusion of static deformation results. Therefore, to improve simulation accuracy, the static deformations measured in the European Transonic Windtunnel (ETW) were accounted for in the CFD model used herein [8, 150]. Wind tunnel campaigns and numerical simulations have been carried out for both the half-wing and full model versions of the aircraft, and an extensive list of the associated publications can be found on the NASA website [151]. In addition, global stability analysis [9, 95] and resolvent analysis [99] studies have also been conducted for the CRM test case.The model wing has a quarter-chord sweep angle of 35°, a reference area of 0.28 m^2, a mean aerodynamic chord (MAC) of 0.189 m and a reference semi-span b of 0.793 m, giving it an aspect ratio of 9 [152]. The full aircraft dimensions in relation to the wind tunnel model are scaled by a factor of 37.4 and their similarity to the characteristics of modern airlines can be seen in table 3.1. The computational mesh has about 6.2×10^6 points, previously generated using the Solar mesh generator just like the RBC12 and the hemispherical far-field boundary is located at a distance of approximately 100 semi-spans from the body. Once mirrored with respect to the fuselage centre plane, the full-span mesh, used in the aeroelastic study, is composed of approximately 12×10^6 points. Even though the model was run at different conditions in the ETW and the National Transonic Facility (NTF) wind-tunnel campaigns, the tests concerning the investigation of shock buffet focused on Mach numbers ranging from 0.25 to 0.87 and Reynolds numbers ranging from 2.9×10^6 to 30×10^6. For the simulation results presented herein, the focus is on a Mach number of 0.85 and a Reynolds number (based on MAC) of 5×10^6, conditions at which the shock buffet onset occurs at an incidence of approximately 3.7°. The steady-state surface pressure distribution with highlighted values of zero skin friction for $\alpha = 3.7°$ is shown in figure 3.5(b). In

contrast to the RBC12, the reverse-flow area behind the shock is smaller in size and located more inboard towards the yehudi break. At these conditions, the CRM has a lift coefficient (C_L) of about 0.6.

Chapter 4

Flow Response to Harmonic Forcing

In this chapter, the phenomenon of shock buffet is investigated by examining the flow response to harmonic forcing. Following the seminal work of Tijdeman [28], more recent studies on aerofoils [63, 64, 69, 153–155] have demonstrated that valuable lessons can be learned about shock buffet by examining the aeroelastic interactions of the phenomenon therefore motivating the study presented herein. In the case of aerofoil aeroelastic forcing, a "lock-in" phenomenon occurs where the flow response becomes fully synchronised with the excitation for certain combinations of excitation frequencies and excitation amplitudes, something that has also been observed experimentally [37]. The present study aims to contribute to the understanding of the phenomenon mechanisms by extending the effects of aeroelastic forcing to finite swept wings. Firstly, the effect of harmonic forcing is analysed for the two wing designs by using a frequency linearised approach, simultaneously demonstrating how different design philosophies affect the flow physics of the phenomenon. This is achieved by imposing a small structural excitation over a range of frequencies for both geometries and analysing their respective responses. The synthetic torsion mode, used consistently in this chapter for the harmonic excitation, has been presented in Chapter 2. The two aircraft models used, namely the RBC12 and the NASA Common Research Model, are representative of a 1970s and a modern airliner respectively, and have been presented in the previous chapter. Secondly, time-accurate harmonic forcing simulations for larger excitation amplitudes are carried out for the RBC12 for combinations of excitation frequencies and amplitudes. A discrete Fourier transformation allows for the closer examination of the frequency content of the resulting lift coefficient signal.

4.1 Linearised Response

In the first part of this chapter, the structural excitation imposed has a small amplitude and therefore the response is considered to be linear. The efficient solution of this problem using the linearised frequency domain (LFD) solver implemented in the DLR-TAU code allows for a sweep of excitation frequencies. In addition to the solution of the linearised harmonically excited system, complementary eigenvalue computation results are presented. Simulations are carried out for both pre and post-onset conditions. For the RBC12, the focus is on a Mach number of 0.8 and a Reynolds number of 3.75×10^6 with angles of attack ranging from 2° to 3.01° whereas a Mach number of 0.85 and a Reynolds number of 5×10^6 with angles of attack ranging from 3° to 3.6° are used for the NASA CRM. The second-order spatial discretisation uses the standard central scheme with artificial dissipation. While scalar dissipation is used for the RBC12, matrix dissipation is selected for the CRM. The steady-state solutions which are the starting point for the LFD simulations converged by at least ten orders of magnitude.The unsteady part is formed as a complex-valued amplitude function $\widehat{\boldsymbol{q}}$ in three-dimensional space times a time-dependent exponential function $e^{\lambda t}$ where t is the time and λ is either simple harmonic (i.e. $\lambda = i\omega$ with ω as angular frequency and i as the imaginary unit) for forced excitation or damped harmonic (i.e. $\lambda = \sigma + i\omega$ with σ as growth rate) for the eigenvalue computation. The implicitly restarted Arnoldi method [113], as implemented in the ARPACK library [156, 157], is used for the latter calculations. The baseline LFD solver is adapted to solve linear systems arising from the shift-and-invert spectral transformation within the Arnoldi iterations [95].

4.1.1 Results

Figure 4.1 presents the variation of the lift coefficient magnitude and phase for different angles of attack in pre-buffet conditions for a typical range of frequencies. The onset angle of attack, that has been observed both numerically and experimentally, is $\alpha = 3^\circ$ for the RBC12 and $\alpha = 3.7^\circ$ for the NASA CRM. The incidences examined, start from subcritical values, specifically $\alpha = 2^\circ$ for the RBC12 and $\alpha = 3^\circ$ for the CRM. At these conditions, the flow does not demonstrate any oscillations. As the incidence is increased, a first resonant peak appears for a Strouhal number of about 0.1 that reaches its local maximum when approaching the onset angle of attack. In this low-frequency range, the aerodynamic response leads the structural excitation in phase for increasing frequency until the peak in magnitude is reached. Similar response behaviour has been reported previously for aerofoils [158]. With buffet onset being imminent, minimal increases of the angle of attack result in a distinct behaviour on both wings at higher frequencies, as the structural excitation appears to excite the shock buffet dynamics. While the

lower frequency peak remains mostly unaffected, a strong amplification is observed in the higher frequency range with Strouhal numbers of about 0.3 to 0.7. Even though the two wing models suggest distinct steady states, cf. the distributed pressure loads in figure 3.5, the dynamic response of the integrated loads appear to be similar, supporting the idea that a general shock buffet mechanism is excited. However, scrutinising the distributed unsteady pressure distribution for the two wings in figure 4.2, regions of high unsteady response correspond with the reverse flow regions in the underlying steady flow field, and hence show differences accordingly. Note again that pre-buffet conditions are considered, where such steady states exist. Additionally, the distributed aerodynamic response due to the forced structural excitation, as seen in figure 4.2, shows spatial similarities to the self-excited shock-buffet unsteadiness on the rigid wing, as seen in figure 4.4. These distributed surface loads are discussed next.

Plots of the magnitude of the complex-valued unsteady surface pressure coefficient, for both the low- and high-frequency behaviours mentioned above, are presented in Figure 4.2. The low and high frequencies with the corresponding incidence shown are $St = 0.13$ and 0.5 at $\alpha = 3.0°$ for the RBC12 and $St = 0.09$ and 0.38 at $\alpha = 3.6°$ for the CRM, respectively. The low-frequency behaviour has not been understood entirely yet, or at least not conclusively analysed numerically, to the knowledge of the author. From an experimental point of view, a couple of studies have shown an interesting distinct flow behaviour of span-wise inboard propagation of waves along the shock front in the same lower frequency range [74, 148]. The present numerical studies demonstrate that the aerodynamic response in the lower frequency range is dominated by the shock wave dynamics and this behaviour is clearly noticeable for both models. At higher frequencies, which are linked to the shock buffet instability, high values of shock unsteadiness are more localised with a distinct flow pattern downstream at these span locations. For the RBC12, this behaviour is located towards the wing tip region corresponding to the most outboard region of reversed flow, cf. figure 3.5. For the CRM, on the other hand, this zone is shifted further inboard halfway between wing tip and crank.

Figures 4.3 and 4.4 present results from the eigenmode calculations. Three-dimensional spatial structures of the amplitude function $\widehat{\boldsymbol{q}}$ are visualised for both wing cases in figure 4.4, corresponding to the right-most eigenvalue in figure 4.3 at $\alpha = 3.0°$ for the RBC12 and $\alpha = 3.70°$ for the CRM, respectively. The figure shows the three-dimensional mode shape of the real part of the x-momentum component ($\widehat{\rho u}$) of the conservative field solution. Only the real part is shown since the imaginary part is 90° out-of-phase to allow, in this case, the span-wise outboard and stream-wise downstream propagation of the shock buffet cells. The figure also highlights how the three-dimensional buffet mode originates at the wing near the outermost station of the

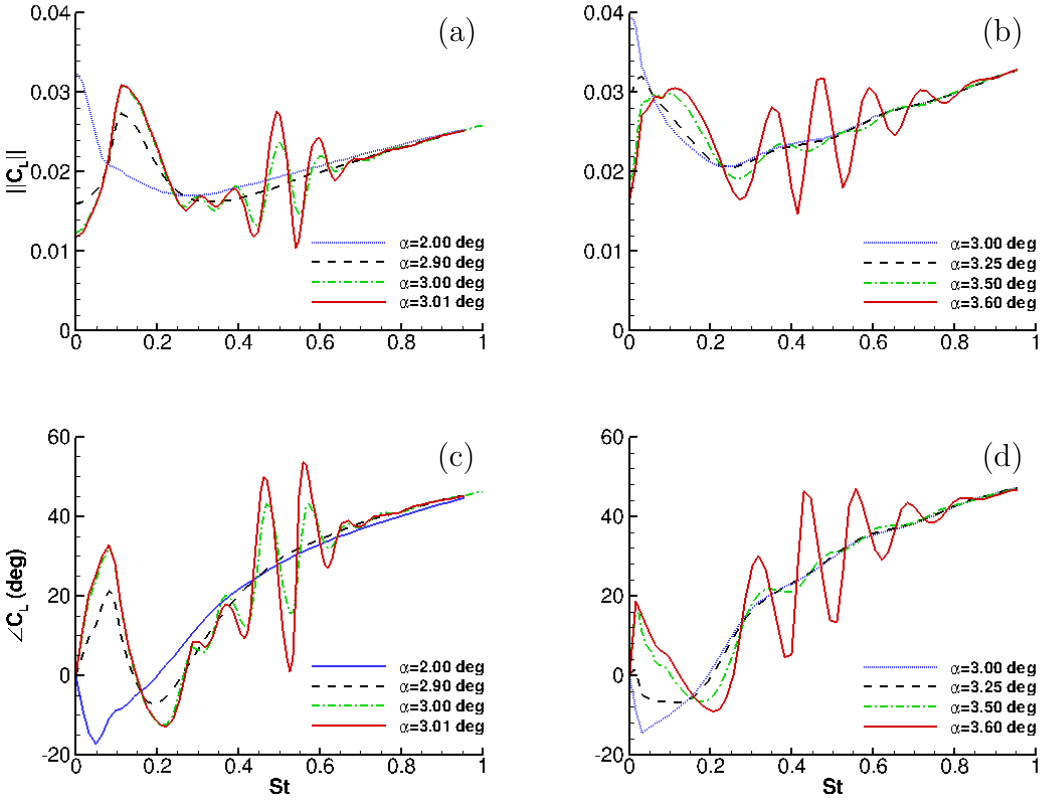

FIGURE 4.1. Frequency response of lift coefficient (C_L) showing magnitude and phase around buffet onset angle of attack for the RBC12 (a),(c) and CRM (b),(d).

reverse flow region in the underlying steady flow field, as indicated earlier. Looking at the spatial structures, and then at the migration of a set of eigenvalues towards the imaginary axis in figure 4.3, it becomes evident that the high-frequency behaviour is due to a bifurcation parameter, specifically angle of attack, above which an eigenvalue crosses into the unstable half-plane. In this study we restrict ourselves to the subcritical pre-buffet regime [95]. Frequencies and growth rates are similar near shock buffet onset for the two wing designs.

4.2 Time Accurate Response

In the second part of the harmonic forcing study, the time-accurate nonlinear equations are solved, therefore allowing larger excitation amplitudes. Since the solution of such systems is more computationally intensive compared to the previous linearised analysis, the structural excitation is carried out for selected frequencies. The angles of attack for the pre-onset and shock-buffet conditions are $\alpha = 3.0°$ and $\alpha = 3.1°$ respectively, with

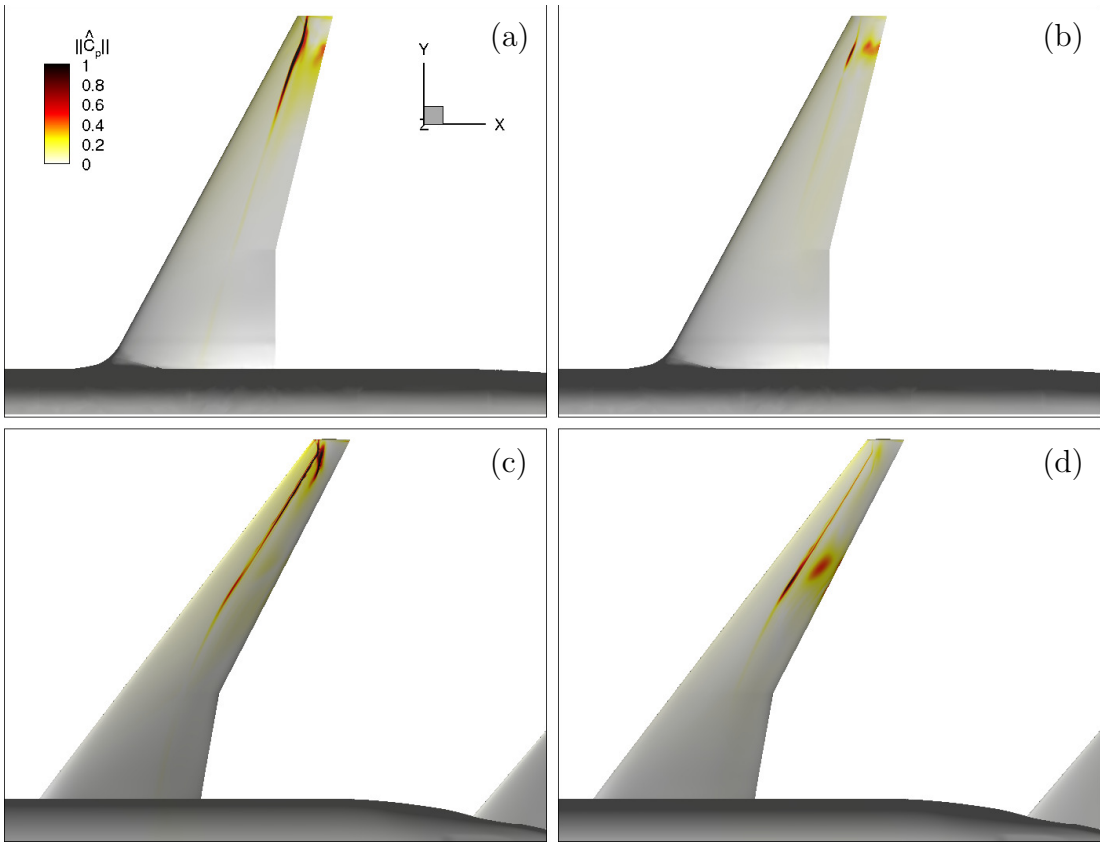

FIGURE 4.2. Magnitude of unsteady surface pressure coefficient for the RBC12 (a),(b) and CRM (c),(d). Plots of low-frequency behaviour (RBC12 $St = 0.13$, CRM $St = 0.1$) and high-frequency behaviour (RBC12 $St = 0.5$, CRM $St = 0.38$) can be found on the left and right, respectively. The angles of attack are $\alpha = 3°$ for the RBC12 and $\alpha = 3.6°$ for the CRM.

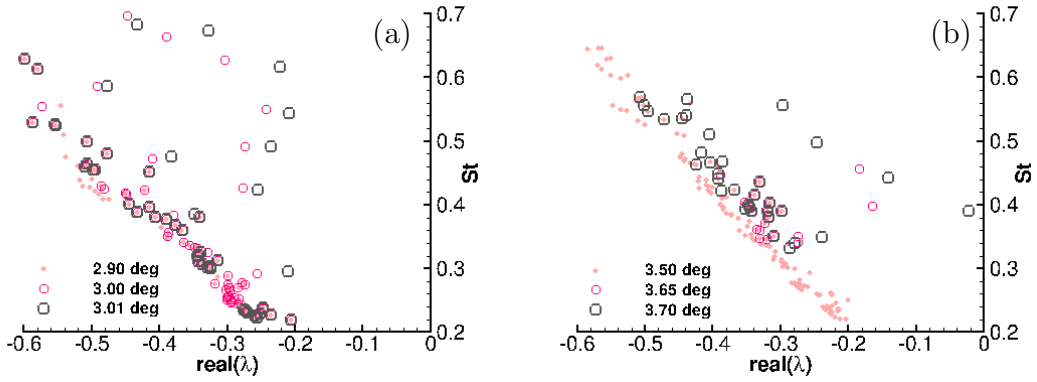

FIGURE 4.3. Eigenvalues of fluid Jacobian matrix for increasing angle of attack in the pre-buffet regime for (*a*) RBC12 and (*b*) CRM.

a Mach number of 0.8 and a chord Reynolds number of 3.75×10^6. Specifically, eight reduced frequencies ranging from $\omega^* = 0.5$ to $\omega^* = 4.0$ with 0.5 increments are used in the pre-onset regime. Four of these frequencies, namely $\omega^* = 0.5, 1.5, 2.5$ and 3.5 are further analysed at three different excitation amplitudes, namely $\boldsymbol{q}_0 = 10^{-5}, 10^{-3}$ and

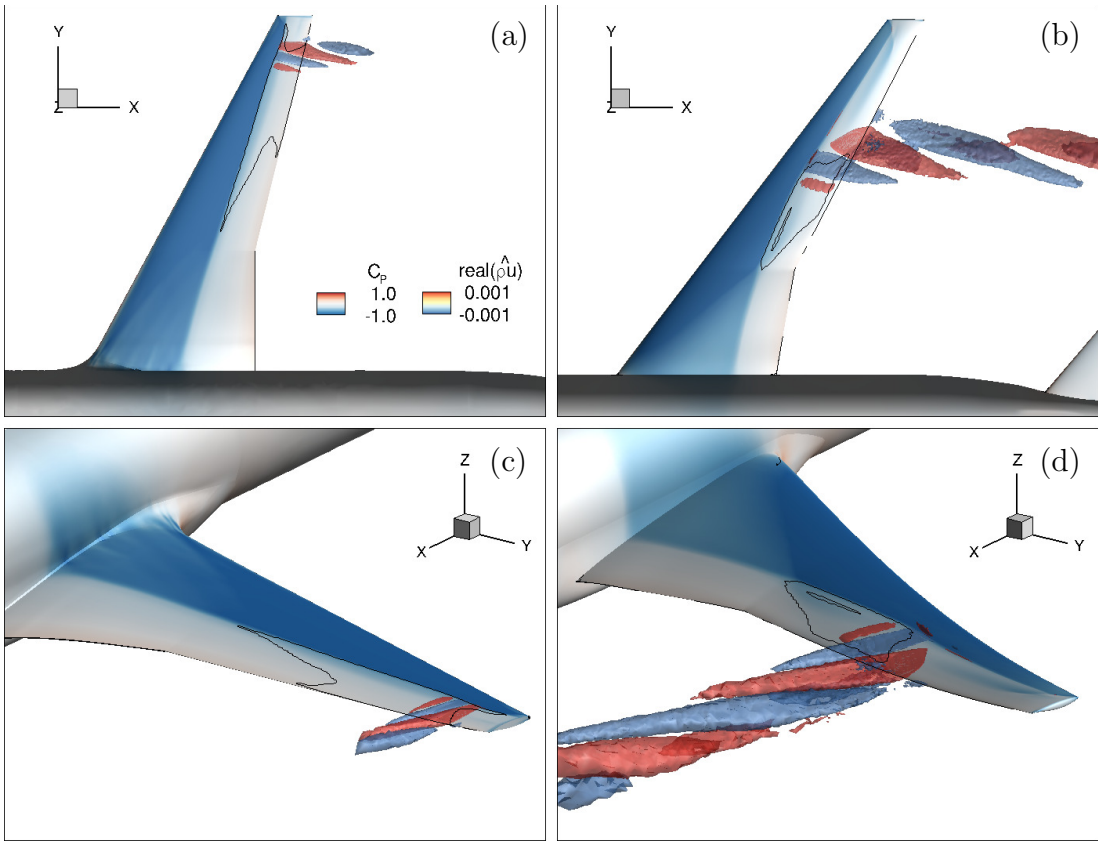

FIGURE 4.4. Spatial structure of the pre-onset three-dimensional buffet mode from global stability analysis showing iso-contour of real part of x-momentum $\widehat{\rho u}$ together with steady-state surface pressure and zero skin friction line for RBC12 at $\alpha = 3°$ (a),(c) and CRM at $\alpha = 3.7°$ (b),(d).

10^{-1}, to investigate amplitude variation at steady conditions.The reduced frequencies are related to the Strouhal number as $\omega^* = 2\pi St$. While the main purpose of the pre-onset simulations is for validation against the linearised results presented in the first part of this chapter, and therefore their frequencies are chosen to span a representative range, further scrutiny of their response gives useful insight in the shock buffet dynamics. Additionally, temporal convergence and mesh deformation checks are carried out for these conditions. For the unsteady regime, the reduced frequencies are chosen based on the shock buffet oscillation frequency. Since the latter is broadband in nature with the largest amplitude response being located around $\omega^* = 3.0$, the excitation frequencies are chosen to cover that range and are namely $\omega^* = 2.5, 3.0$ and 3.5. At these conditions, a wider range of excitation amplitudes is used for the examination of the unsteady flow response, namely $\boldsymbol{q}_0 = 10^{-3}, 10^{-2}, 10^{-1}, 1$ and 5. At each time step, the pseudo residual is iterated to an approximate steady state (residual order of 10^{-3}) before evaluating the next step. The physical time step follows from the excitation frequency and the chosen number of steps per cycle. For the pre-onset simulations, 1024 steps per cycle are used whereas 2048 steps are used for the simulations in a

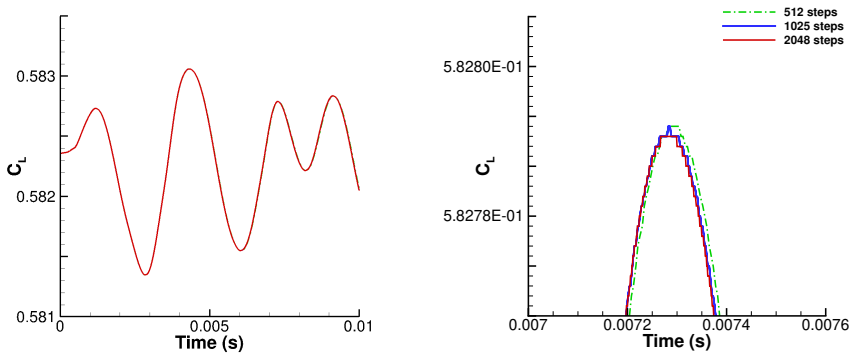

(a) Lift coefficient response

(b) Zoom in between $t = 0.007\ s$ and $t = 0.0076\ s$

FIGURE 4.5. Response of lift coefficient C_L over time for an excitation amplitude $q_0 = 1.0$ and frequency $\omega^* = 3.0$ post buffet onset ($\alpha = 3.1°$) for different timesteps per cycle of harmonic excitation. A closer view of the response is shown on the left.

globally unstable flow. The effect of using different number of timesteps per cycle in post-onset conditions can be seen in figure 4.5. The dynamic pressure along with the time variant pressure coefficient multiplied by the synthetic mode shape is referred to as the generalised aerodynamic force. Combined with the lift coefficient, they make up the integrated aerodynamic loads, used to project the surface flow solution onto the structural mode. These are computed once the flow equations have converged at the end of each physical time step. For the unsteady RANS simulations, together with the convergence criterion on the norm of the density residual (10^{-3}), a Cauchy criterion is applied for the drag coefficient with error tolerance 10^{-9} with a minimum of 150 inner iterations per real time step. In addition, for the non-linear time-marching simulations, different mesh deformation settings were used to permit the simulation of larger excitation amplitudes. Volume mesh deformations resulting from structural deformations are calculated applying the radial basis function (RBF) method. Radial Basis Functions are functions that change with distance from a location and are used in CFD mesh deformation as they can preserve the validity and quality of the mesh, even for large displacements, without being affected by mesh connectivity [159]. In the current case, thin plate spline interpolation is used to ensure smooth deformations even for the small wing deflections close to the fuselage in comparison to the overall larger deflection towards the wing tip. RBF requires the definition, amongst other parameters, of weighting radii. In the area defined by the full weight radius r_1, full deformation is applied, represented by a weighting of 1. The zero weight radius r_2 denotes a larger distance containing r_1. Within this radius, along the distance r_2 - r_1, the deformation weighting is linearly blended to the flow field from 1 to 0. The effect of the RBF settings, specifically different weighting radii, on the lift coefficient response is negligible, as shown for representative case in figure 4.6.

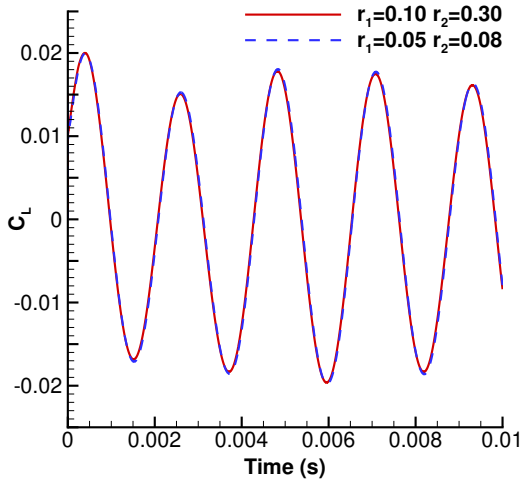

FIGURE 4.6. Response of lift coefficient C_L over time for an excitation amplitude $q_0 = 1.0$ and frequency $\omega^* = 3.0$ from simulations using different mesh deformation settings for radii r_1 and r_2.

4.2.1 Validation of Results

Unsteady time-marching results for different excitation frequencies for an amplitude factor of $q_0 = 0.001$ at pre-onset conditions computed using the FlowSimulator package of DLR-TAU were compared with the LFD results presented earlier for validation. Figure 4.9(a) shows the magnitude of the lift coefficient, $|C_L|$, at the respective fundamental frequencies of the excitation obtained from a discrete Fourier transform on the lift signal. Comparison of the results obtained from time-marching simulations with the LFD results shows that the two methods are in excellent agreement. The frequency response of the lift coefficient magnitude, calculated using the LFD method, shows a low frequency resonant peak between $\omega^* = 0.4$ and 1.6 along with higher frequency wiggles between $\omega^* = 2.6$ and 3.8. This behaviour is also found for the lower amplitude content from the time dependent simulations at four frequencies, shown in figure 4.9(b). There it can be seen that at pre-onset a lower frequency bump in the same range as the LFD reasonant peak is present, something that is consistent for all forcing frequencies. This shows that apart from forcing frequencies close to the buffet range around $\omega^* = 3$, lower frequencies can excite buffet dynamics, something that agrees with the behaviour observed in previous studies [94].

4.2.2 Pre-onset Conditions

The simulations in pre-onset conditions examine the effect of the excitation amplitude in a globally stable flow. Figure 4.7 shows the lift coefficient magnitude normalised by excitation amplitude as a function of amplitude factor, specifically $q_0 = 10^{-5}, 10^{-3}$

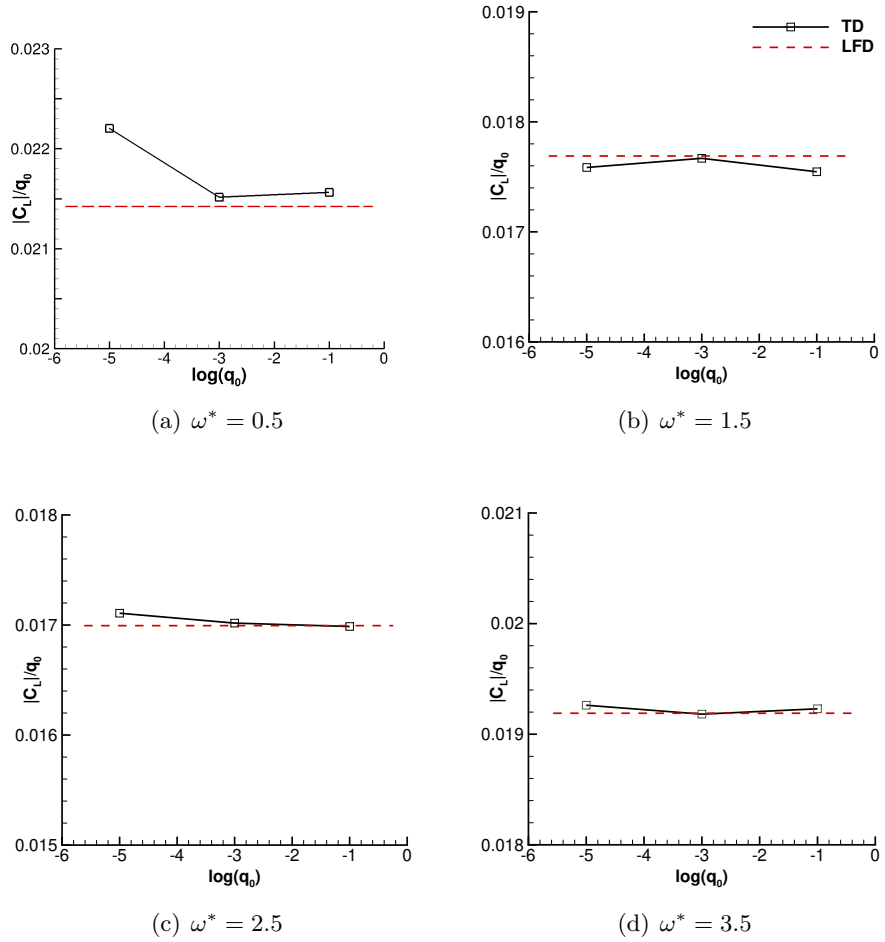

(a) $\omega^* = 0.5$ (b) $\omega^* = 1.5$

(c) $\omega^* = 2.5$ (d) $\omega^* = 3.5$

FIGURE 4.7. Comparison of lift coefficient magnitude from LFD results with time-marching simulations, normalised by excitation amplitude for amplitude factors $q_0 = 10^{-5}, 10^{-3}$ and 10^{-1} and different excitation frequencies ω^*.

and 10^{-1}, at four chosen frequencies. The frequency response from the time-marching simulations for the range of different q_0 agrees nicely with the LFD results. Nevertheless, errors that arise from the iterative numerical scheme result in a higher magnitude for the lowest amplitude factor of $q_0 = 10^{-5}$ as can be seen for $\omega^* = 0.5$, demonstrating that tighter convergence tolerances would be required at this excitation amplitude factor. Additionally, it can be seen that best agreement is obtained for an amplitude factor of $q_0 = 10^{-3}$. Figure 4.8 shows the corresponding sum of the higher harmonics of the fundamental excitation frequency over time periods. As the frequency increases towards the typical shock-buffet range, located around $\omega^* = 3$, higher harmonics of similar magnitude are excited for all excitation amplitudes. The summary of higher harmonics represents the amount of distortion present in the response of a system forced at a certain frequency. The distortion stems from the most dominant harmonic components whose frequency is a multiple of the fundamental frequency, and therefore the decreasing magnitude of their sum directly demonstrates that the system response

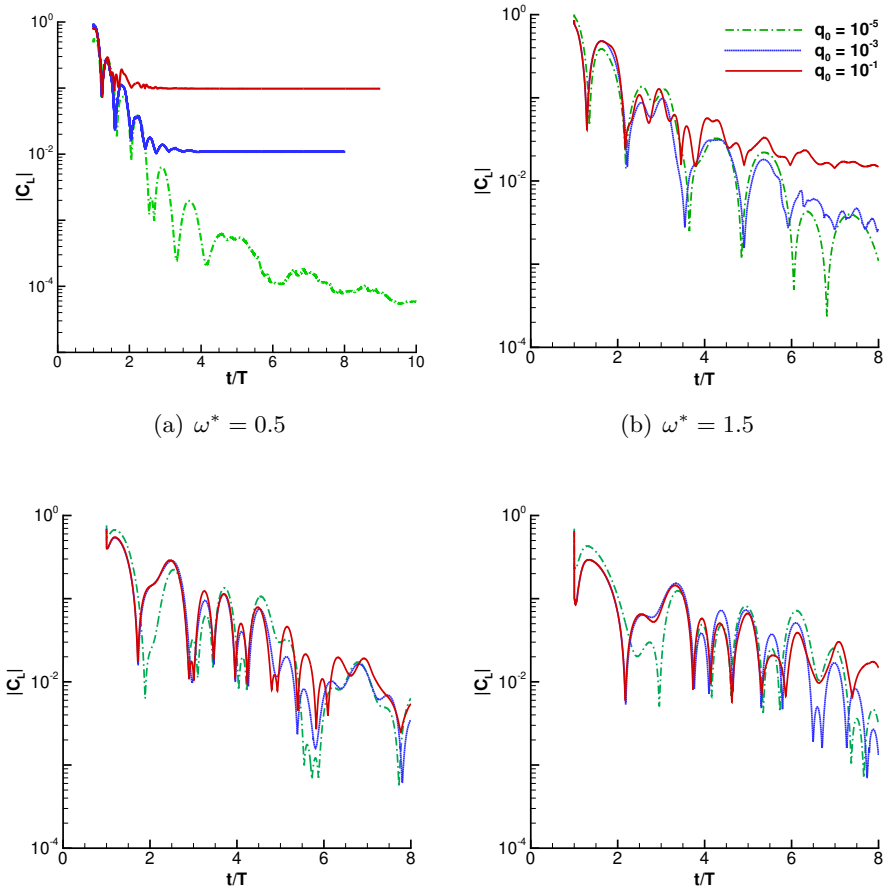

(a) $\omega^* = 0.5$ (b) $\omega^* = 1.5$

(c) $\omega^* = 2.5$ (d) $\omega^* = 3.5$

FIGURE 4.8. Comparison of the sum of higher harmonics of the excitation frequency over computational cycles.

settles around the fundamental forcing frequency. It is here worth pointing out that more iterations are required for the response to settle as we get closer to the shock-buffet range, even for small excitation amplitudes, since the system is forced close to the frequency of the imminent, and therefore weakly damped, unsteady response. Due to the computational cost of the simulations, a compromise between the highest accuracy and increasing computational cost was aimed for. The chosen simulation setup is such a robust compromise.

4.2.3 Buffeting Flow Conditions

The unsteady response to harmonic excitation, while the flow is globally unstable exhibiting shock buffet, for angles of attack higher than 3° is discussed next. Figure 4.10 shows the response of the lift coefficient following a harmonic forcing with increasing amplitude factor q_0. The left column presents the time histories of the raw data,

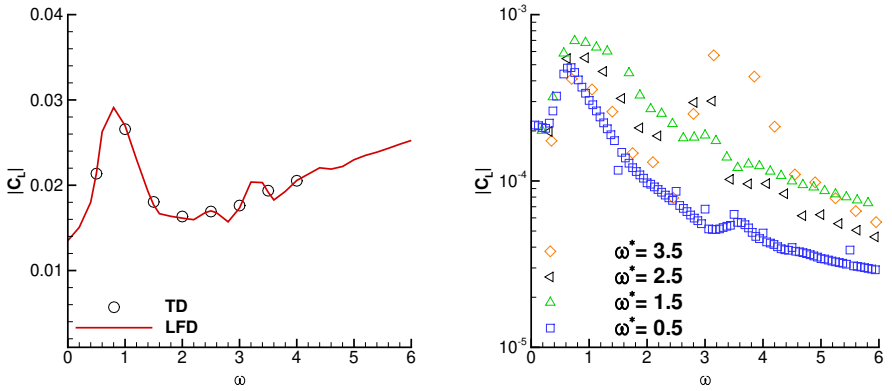

(a) Peaks at fundamental frequencies (b) Zoon in on lower amplitude response

FIGURE 4.9. Magnitude of unsteady lift coefficient C_L from Fourier analysis of time-domain (TD) simulations at pre-onset conditions at different excitation frequencies for an amplitude factor $q_0 = 0.001$. The solid line represents unsteady lift results computed previously using RANS LFD simulations. The amplitude peaks at the respective fundamental frequencies for different excitation frequencies are shown in (a) while (b) shows a closer view of the additional lower amplitude frequency content.

whereas the right column gives processed results, with the lift response scaled by q_0 and the time normalised by the period of oscillation. For $q_0 = 0.001$ the response follows that of the static shock-buffet simulation which in this case is the lift variation due to the shock-buffet unsteadiness shown in figure 4.10(a). With increasing amplitude factor, the lift response starts desynchronising from the buffet dynamics and follows the structural excitation instead. Initial synchronisation can be seen in figure 4.10(b) while distinctly different response compared to the static simulation signal is evident in figure 4.10(c). For the largest amplitude factors, $q_0 = 1.0$ and 5.0, the response is fully aligned with the forcing, as can be clearly seen in the scaled results.

Discrete Fourier analysis of the unsteady lift coefficient returns the frequency content for each combination of forcing amplitude factor and frequency. In the left column of figure 4.11, the frequency content of the lift coefficient (specifically its magnitude) for fixed amplitudes in increasing order is shown. It can be seen that for the two lower amplitude factors, $q_0 = 0.001$ and 0.01, the structural excitation increases the amplitude response of the existing buffet dynamics as seen by the strong similarity in frequency content with the static simulation results. As the amplitude factor is increased to 0.1, peaks at the respective excitation frequencies are present. Similarly as before, the underlying unsteady content is excited to higher amplitudes when compared with the static signal. As we further increase to an amplitude factor of $q_0 = 1.0$, the peaks at the respective excitation frequencies become more distinct and larger in magnitude whereas the amplitude of the unsteady content that is excited has the same magnitude as for $q_0 = 0.1$. The same behaviour follows for the largest amplitude factor of 5.0, except that additional peaks at the higher harmonics of the excitation frequencies are

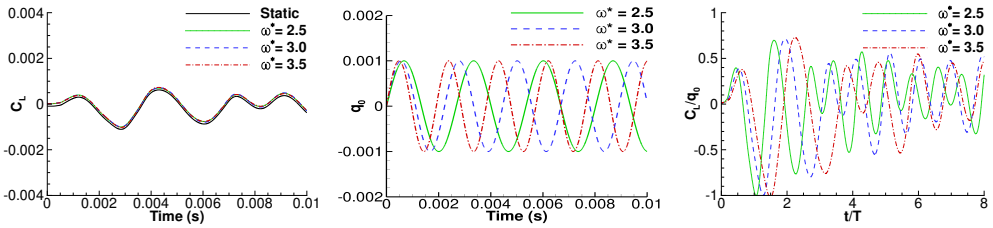

(a) $q_0 = 0.001$

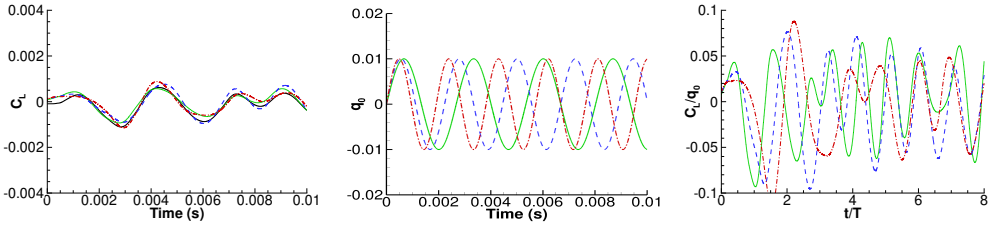

(b) $q_0 = 0.01$

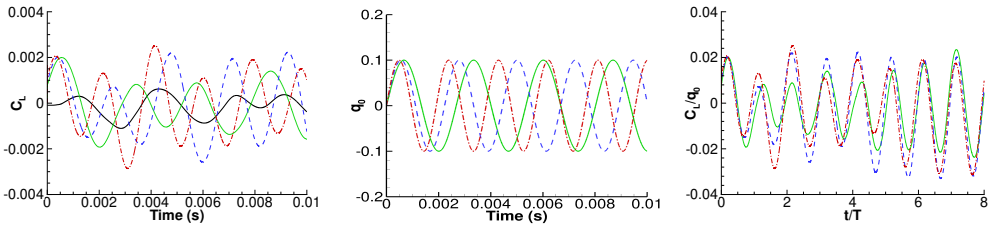

(c) $q_0 = 0.1$

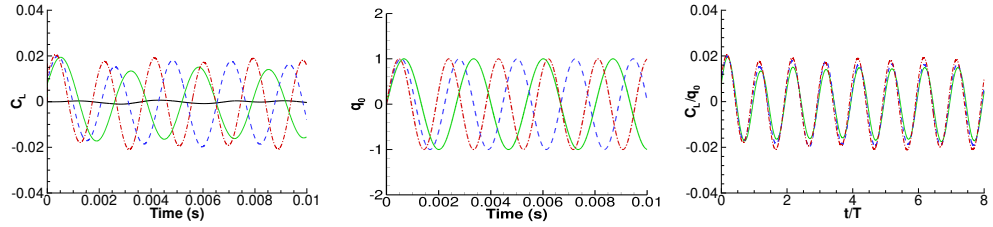

(d) $q_0 = 1.0$

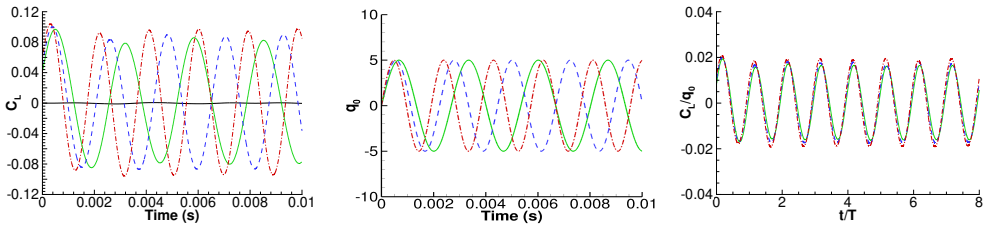

(e) $q_0 = 5.0$

FIGURE 4.10. Response of lift coefficient C_L to harmonic excitation over time (left column) and corresponding lift coefficient normalised by excitation amplitude over periods (right column) at different excitation frequencies at $\alpha = 3.1°$.

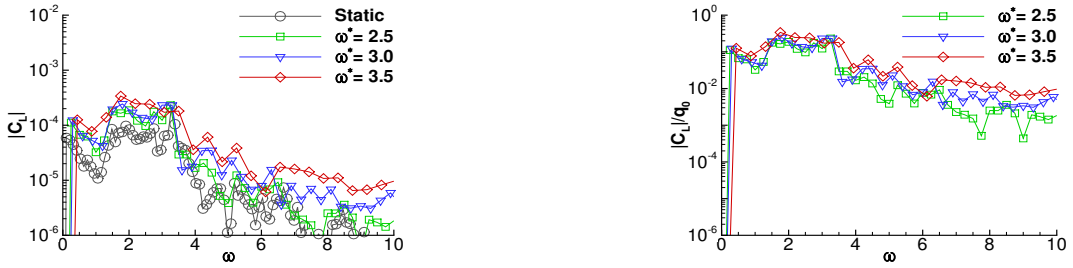

(a) $q_0 = 0.001$

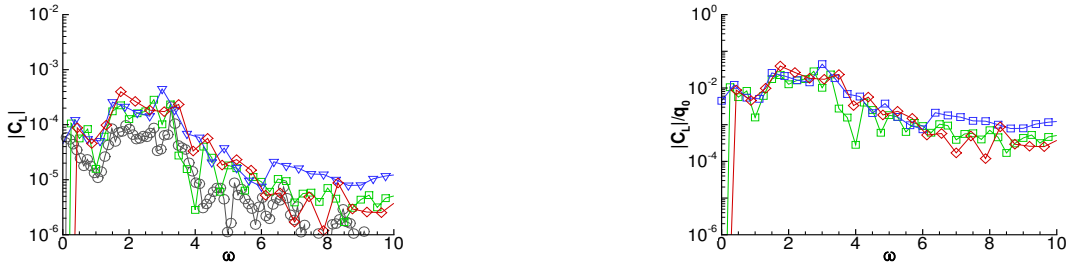

(b) $q_0 = 0.01$

(c) $q_0 = 0.1$

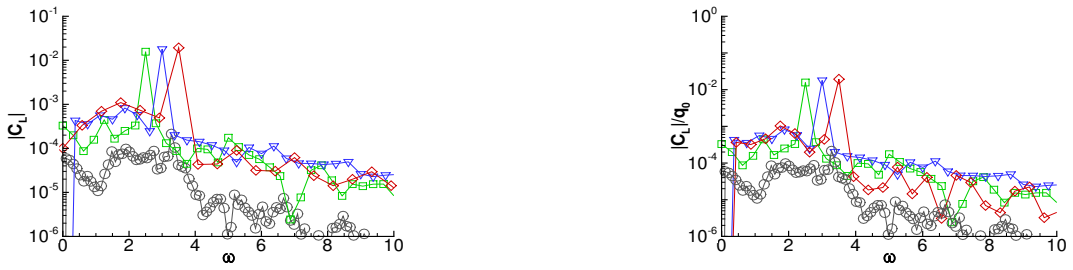

(d) $q_0 = 1.0$

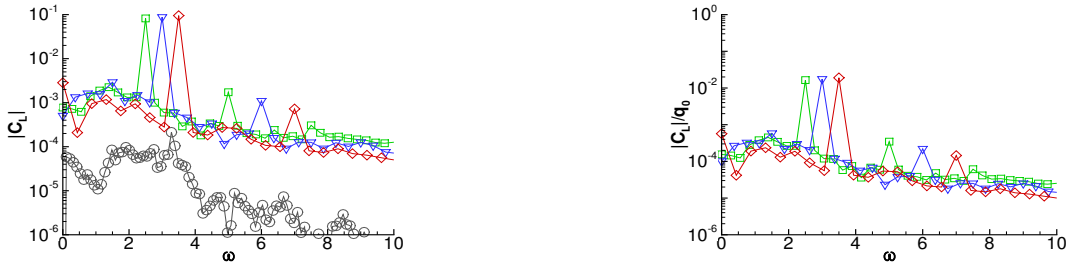

(e) $q_0 = 5.0$

FIGURE 4.11. Frequency response of lift coefficient C_L to harmonic excitation (left column) and corresponding frequency response of lift coefficient normalised by excitation amplitude (right column) at $\alpha = 3.1°$

present compared to $q_0 = 1.0$. In addition, the amplitude of the buffet content that is excited increases in magnitude. Fourier analysis of the scaled results allows similar conclusions. The peaks at the excitation frequencies approximate the dynamic derivatives for $q_0 \geq 0.1$, while the overall level of unsteadiness relative to the excitation at the other (non-excited) frequencies seems to be reduced with increasing forcing amplitude.

Lissajous [160] curves are commonly used to visualise the difference in the angular frequency and the phase of two simple harmonic motions, which herein are given by the harmonic excitation and the response, respectively. Specifically, for two signals where the ratio of their frequencies is irrational the curve will not retrace its own path and conversely, the curve will repeat itself if this ratio is rational [161]. This ratio also defines the number of lobes in the curve, therefore when the frequencies are matching (ratio of 1), the resulting curve is an ellipse. Indeed, in figure 4.12, it can be seen that for small amplitude excitation factors ($q_0 \leq 0.01$) the curve formed by the response of the lift coefficient does not retrace itself since it follows the broadband frequency response of shock buffet. A transitional stage is observed for an amplitude factor of $q_0 = 0.1$ and an elliptical curve can be seen for the two largest amplitude factors $q_0 = 1$ and 5 where the response follows the excitation. In addition, the eccentricity of the elliptical curve gives information about the phase difference of the two signals, which for the response of all excitation frequencies is $\frac{\pi}{4}$.

Figures 4.13 and 4.14 show contours of the instantaneous surface pressure coefficient along a harmonic excitation cycle. The surface friction coefficient isolines help visualise the areas of separated flow. Since the qualitative behaviour between the different forcing frequencies appears similar, a representative case for a reduced excitation frequency of $\omega^* = 3.0$ is shown for two different amplitude factors of $q_0 = 0.01$ and 1. These were chosen following the distinctly different frequency content responses seen in figures 4.11(c) and 4.11(d). Firstly, it can be seen that the unsteadiness location agrees both with the earlier LFD and eigenvalue analysis results. Secondly, for the lowest amplitude factor, the extent of the shockwave oscillation in the streamwise direction is smaller compared to the large amplitude factor case. Finally, for the smallest amplitude factor, the separated area observed for a steady state appears to remain constant in size while intermittent outboard convection of separated areas is observed. This results from the vortex shedding emanating from the location of the instability. A similar behaviour is observed for the largest amplitude factor, although in that case, the separated area is smaller than the one observed for a steady state and the vortex shedding causes larger separation areas moving towards the wingtip.

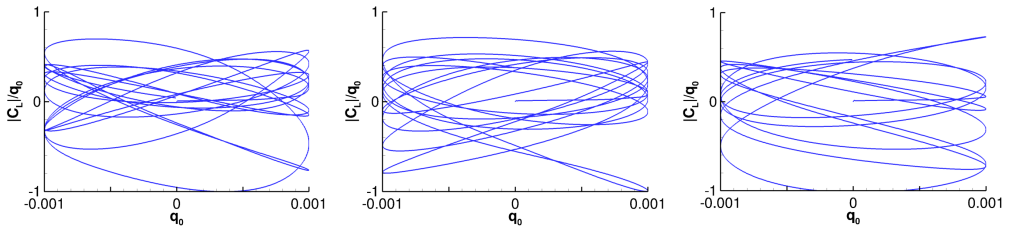

(a) $q_0 = 0.001$

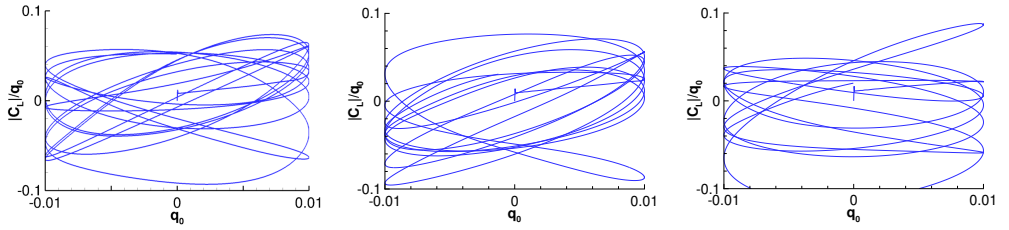

(b) $q_0 = 0.01$

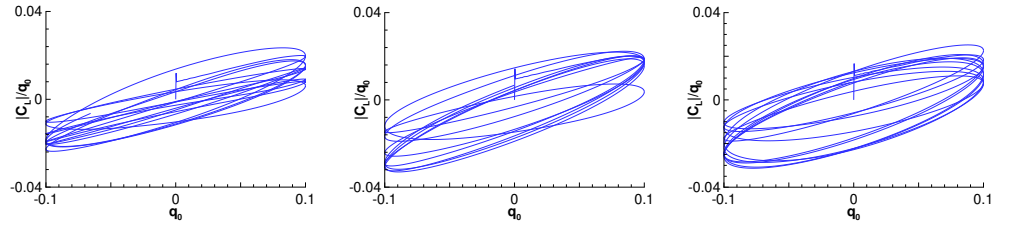

(c) $q_0 = 0.1$

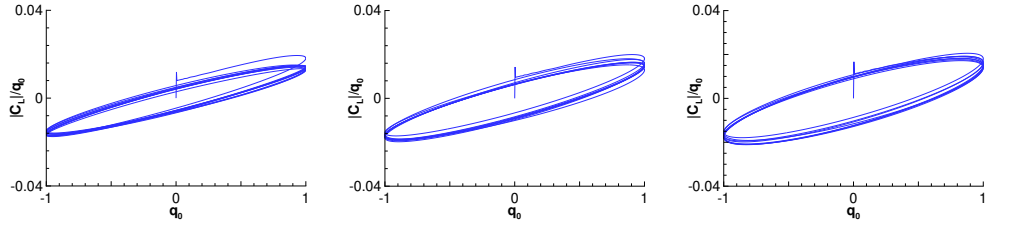

(d) $q_0 = 1.0$

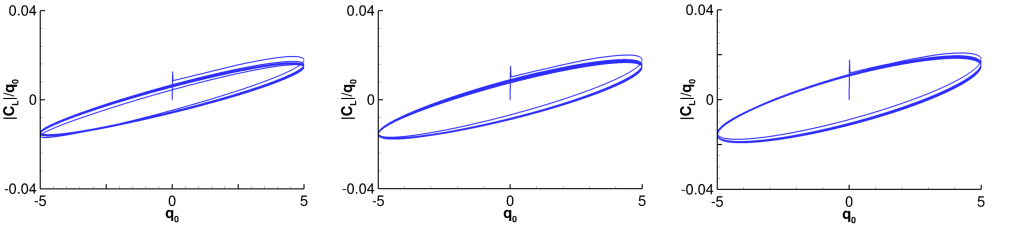

(e) $q_0 = 5.0$

FIGURE 4.12. Lissajous plots for lift coefficient response over structural excitation $q(t) = q_0 \sin(\omega^* t)$ for $\omega^* = 2.5$ (left column), $\omega^* = 3.0$ (middle column) and $\omega^* = 3.5$ (right column) at $\alpha = 3.1°$.

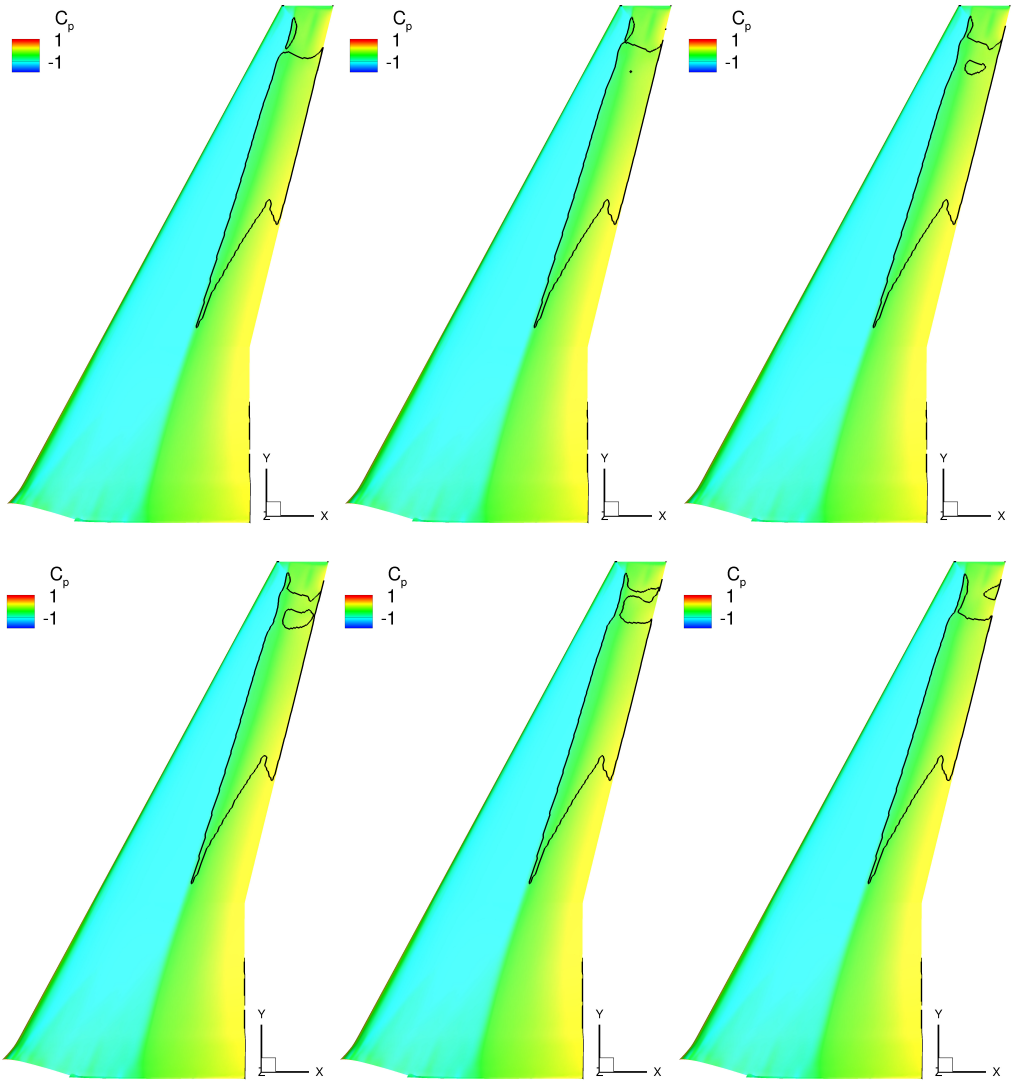

FIGURE 4.13. Time-accurate computed surface C_P for six timesteps over one cycle of harmonic excitation for an amplitude factor of $q_0 = 0.01$ and a reduced frequency of $\omega^* = 3.0$. Specifically snapshots at beggining of cycle, 25% of cycle, 37.5% of cycle, 50% of cycle, 75% of cycle and 87.5% of cycle. The C_F isolines indicate the separated area.

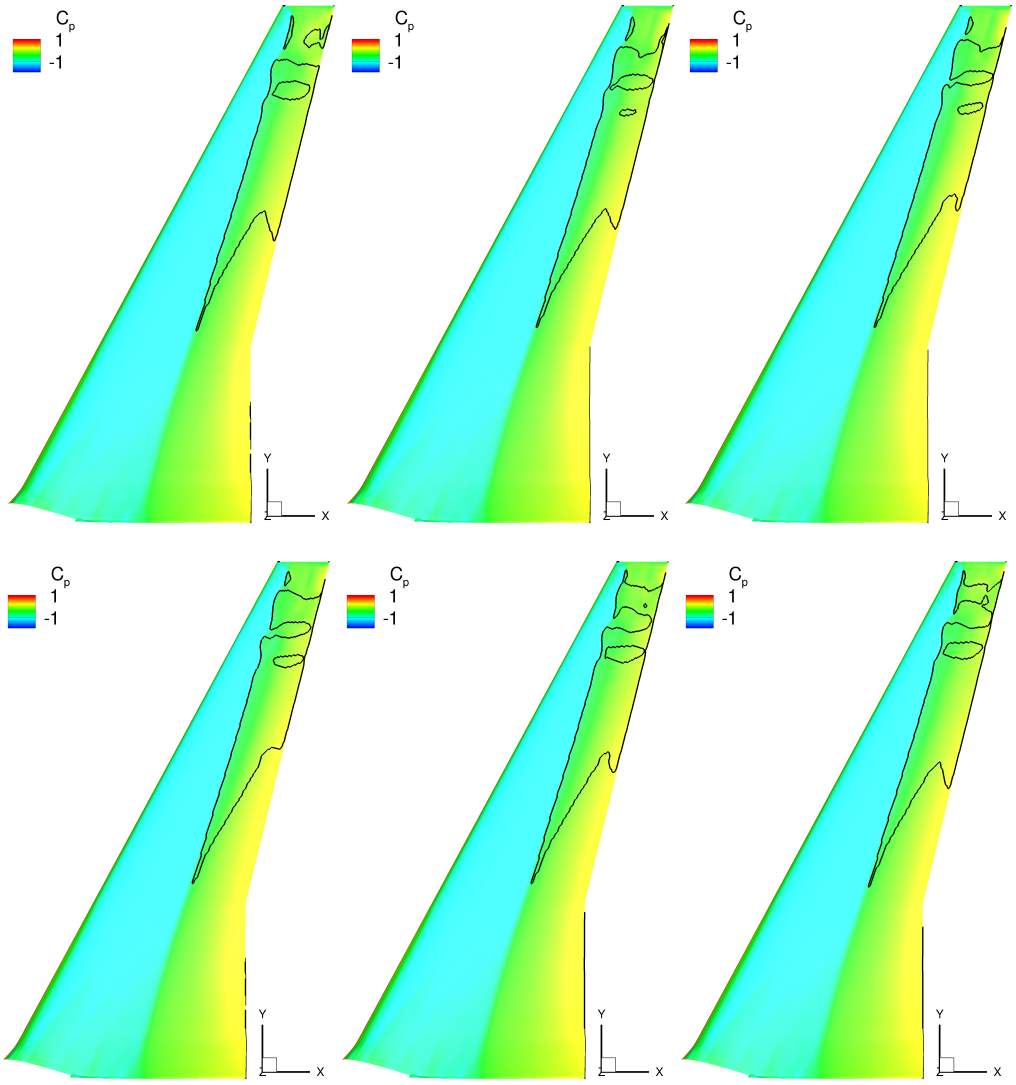

FIGURE 4.14. Time-accurate computed surface C_P for six timesteps over one cycle of harmonic excitation for an amplitude factor of $q_0 = 1.0$ and a reduced frequency of $\omega^* = 3.0$. Specifically snapshots at beggining of cycle, 25% of cycle, 37.5% of cycle, 50% of cycle, 75% of cycle and 87.5% of cycle. The C_F isolines indicate the separated area.

4.3 Summary of Harmonic Forcing Study

In this chapter the response of the flow to harmonic forcing using a synthetic torsion mode was examined for both pre-onset conditions and conditions where shock buffet exists using both linearised and time-accurate nonlinear methods. In the first part, a time-linearised numerical study of the transonic edge-of-the-envelope flow over two large civil aircraft wing models was presented. The purpose of this study was twofold. Firstly, to see how modern wing design has affected the phenomenon of shock buffet compared to older designs and secondly to draw further conclusions on the underlying physical mechanisms of shock buffet. This was achieved by performing a sweep of excitation frequencies covering the relevant range of frequencies to observe the frequency response behaviour of the integrated aerodynamic coefficients close to buffet onset. In addition to the results regarding the corresponding steady and unsteady distributed loads, pre-buffet global stability results, specifically emerging distinct eigenvalues and spatial structures of right-most eigenvalues were presented briefly and linked to the insight gained from the forced excitation simulations. RANS simulations revealed both similar and distinct characteristics of steady and unsteady flow features for the two wing models simulated at the respective design Mach numbers. The responses of the integrated aerodynamic loads for the two models show similar patterns. A low frequency resonant peak with a distinct phase lead of the aerodynamic coefficient with regard to the structural excitation is observed that reaches its local maximum as the angle of attack is increased. For the high-frequency behaviour, the structural excitation close to the buffet onset angle of attack seems to excite an absolute instability. Plots of unsteady distributed loads on the other hand correspond with the differences in steady flow field with an impact on the span-wise origin of the instability. The dynamic response of the linearised aerodynamic coefficients for high frequencies in combination with the three-dimensional structure of the pre-buffet mode and the migration of eigenvalues towards the unsteady half-plane suggests that incipient shock buffet can be treated as a linear stability problem, something that has been recently confirmed [95].

In the second part of the chapter, the harmonic forcing is extended to the non-linear regime, focusing on selected frequencies and a range of amplitude factors for the RBC12 test case. For a pre-buffet flow, results produced from time-domain simulations at different excitation frequencies are compared with LFD results from previous studies. Overall good agreement is found in predicting the dynamics derivatives. The weakly damped modal behaviour of shock buffet close to onset is translated into increased iteration counts for the response to converge to the periodic state. For the shock-buffet flow conditions, the wing is excited around the typical buffet frequencies. A comparison of the various lift responses showed that for lower amplitude forcing, shock buffet dominates the dynamics, whereas the aerodynamic response follows the excitation with

increasing forcing amplitude. By analysing the frequency content of the aforementioned responses it is revealed that lower frequency buffet content is present even for the larger amplitude factors where the lift coefficient response tracks that of the structural excitation. Instantaneous surface pressure coefficient snapshots at different stages of the excitation cycle reveal that the intermittent separation already present at shock buffet conditions increases in size for larger excitation amplitude factors accompanied by larger streamwise displacement of the shock at the region where the instability is located.

To summarize, the conclusions that can be drawn for shock buffet by imposing a harmonic excitation on the steady and unsteady flow are as follows. Firstly, different steady-states demonstrate similar underlying flow mechanisms, hinting the modal nature of the phenomenon, something that is further supported by the eigenvalue analysis of the fluid Jacobian and the weakly damped behaviour close to onset. Secondly, even though the time-accurate response of the lift coefficient appears to be synchronised with that of the excitation, a closer scrutiny of the frequency content reveals a different behaviour. While the high frequency broadband response of the phenomenon, that is associated with the unstable eigenvalue, is shifted to the excitation frequency above a certain amplitude factor threshold, the low frequency content located in the range of the resonant peak from the LFD analysis remains unaffected. Similar studies that focused on the harmonic excitation of aerofoils in transonic buffeting flows [63, 64, 153] demonstrated a complete lock-in of the shock buffet oscillation frequency to that of the excitation frequency for certain combinations of frequencies and excitation amplitudes. This absence of such lock-in in the case of harmonically excited wings presented herein further distinguishes two and three-dimensional shock buffet.

Chapter 5

Fluid-Structure Interaction

In this chapter, the interaction of transonic buffet with wing vibration is further investigated. The effect of aeroelastic coupling on the shock buffet dynamics is scrutinised by a fluid-structure interaction simulation using the NASA Common Research Model. Even though the majority of work dealing with shock-buffet on finite wings focuses on the analysis of the aerodynamics of the phenomenon on rigid geometries, real aircraft wings are flexible structures thus their interaction with the unsteady loads motivates such a multi-disciplinary study. A recent global stability analysis of the coupled system has identified unstable structural modes in addition to the unstable fluid modes for the conditions investigated in the current work [9]. Herein, two simulations, namely, a fluid-structure interaction simulation and an unsteady RANS simulation (fluid-only) are conducted at the same flow conditions to allow for direct comparison of the results. Steady-state pressure distribution and wing deformation is compared with experimental results. Power spectral density is used to represent the distribution of signal frequency components of the resulting lift coefficient signal whereas a discrete Fourier transformation allows for the closer examination of the frequency content for the structural modes response.

5.1 Numerical Setup

For the fluid-only unsteady simulation (starting from the static aeroelastic solution, described below, and imposing the frozen geometry at the equilibrium point), Courant–Friedrichs–Lewy (CFL) numbers of 20 for the finest grid level and 5 for the coarser grid levels are chosen. A physical time-step size of $\Delta t = 2$ μs was applied, sufficient

for the expected frequencies in the dynamic system. Typically, a convective time for the simulation can be defined by considering the ratio between a characteristic length (herein the aerodynamic mean chord) and a characteristic velocity (herein reference velocity). In the present case, the convective time is around 7×10^{-4}, which is considerably higher than the chosen time-step. The total physical time simulated is 0.81 s, something that is analogous to about 50 to 60 buffet cycles. The aerodynamic state is then evaluated for each real time step by iterating the pseudo residual to a steady state with a minimum of 50 inner iterations per time step and a relative Cauchy convergence criterion of 10^{-8} on the drag coefficient. For the static aeroelastic simulation that is performed to obtain the wing deformation by balancing the aerodynamic loads according to the given conditions, specifically solving $\Xi^T K \Xi \boldsymbol{q} = \Xi^T \boldsymbol{f}_a$, both fluid and structural system are converged to an equilibrium in a maximum of 40 outer coupling iterations, with up to 100 iterations of the flow solver per outer iteration. This solution is used as the starting point for the dynamic fluid-structure coupled simulation. For each real time step, up to five coupling iterations are allowed each with 50 inner iterations of the flow solver and the Newmark-beta integration scheme applied for the structural update. Convergence is assessed based on the norm of the relative change in the generalised aerodynamic force vector between iterations. The tolerance is set to 10^{-3} and a minimum of three coupling iterations is always performed. Consistent with the fluid-only simulation, a physical time-step size of $\Delta t = 2$ μs was chosen. Following previous work [95, 162], the focus in this study is on a free-stream Mach number of 0.85 and the Reynolds number (based on the mean aerodynamic chord) is 5×10^6. For the purpose of converting frequencies to and from non-dimensional form, the reference velocity is stated as $281.5\,\mathrm{ms}^{-1}$. The focus angle of attack herein is the supercritical $\alpha = 3.75°$. Reynolds-averaged Navier–Stokes simulations on a rigid (yet statically deformed according to data from the underlying test campaign in the European Transonic Windtunnel) geometry have shown that self-sustained flow unsteadiness occurred for angles of attack above (and including) $\alpha = 3.7°$. This unsteadiness was related to a global instability through an eigenvalue crossing into the unstable half plane for this critical angle of attack at a Strouhal number of approximately $St = 0.39$ (corresponding to a frequency of 580 Hz) [95]. The wind-off structural frequencies of the normal modes retained for the coupled simulation cover a range of 40 Hz to 680 Hz. For the highest structural mode, the chosen time-step size of $\Delta t = 2$ μs gives more than 700 physical time steps per oscillation cycle. Lastly, a grid convergence study is performed by conducting a LFD frequency sweep for three different grid sizes and is shown in figure 5.1. The grid used in the simulations was created by mirroring a half-model mesh of approximately 6×10^6 points and therefore consists of approximately 12×10^6 points.

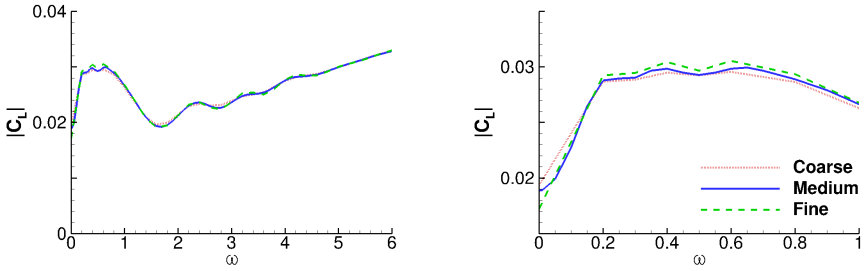

FIGURE 5.1. Grid convergence for the CRM half-wing model showing magnitude of lift coefficient (C_L) for a LFD analysis frequency sweep. The coarse, medium and fine denote mesh sizes of 3×10^6, 6×10^6 and 8×10^6 points, respectively.

5.2 Validation with Experimental Data

The results from the static deformation simulation are compared with measurements from the wind-tunnel campaign, including deformation and pressure data. Figure 5.2 shows deformation data, specifically wing bending and twist taken at 50% local chord along the non-dimensional span coordinate η (made dimensionless using the semi-span length), comparing experimental data, using stereo pattern tracking via markers distributed on the wing surface, and numerical data from both the static and dynamic aeroelastic simulations, whereby the latter are the time-averaged values from the non-linear regime of the signal (to be discussed below). Note that the experiment measured the deformation at angles of attack $\alpha = 3.0°$ and $4.0°$, hence interpolation was required as described in [8]. Three observations can easily be made. First, the numerical results reveal a minor asymmetry between the port and starboard wing, effectively resulting from the high-fidelity finite-element model of the actual wind-tunnel geometry which includes various details of asymmetric cut-outs for accommodating the instrumentation, etc. (note the subtle surface features in figure 2.3 in this regard). Second, there

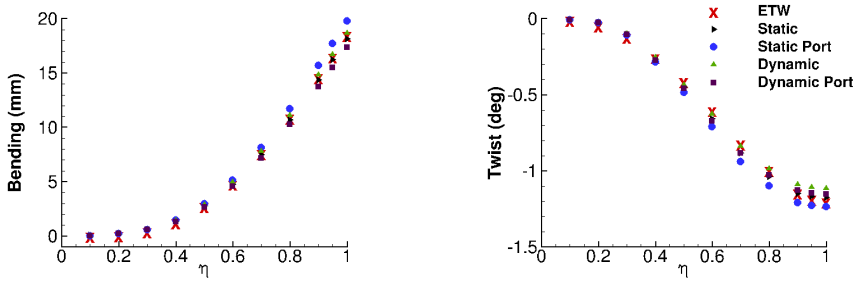

FIGURE 5.2. Bending and twist deformation plots at $\alpha = 3.75°$, comparing data from simulation and wind-tunnel measurements in European Transonic Windtunnel (ETW) for eleven non-dimensional spanwise stations η on both port and starboard wings. Experimental data were interpolated from angles of attack $\alpha = 3.0°$ and $4.0°$ [8].

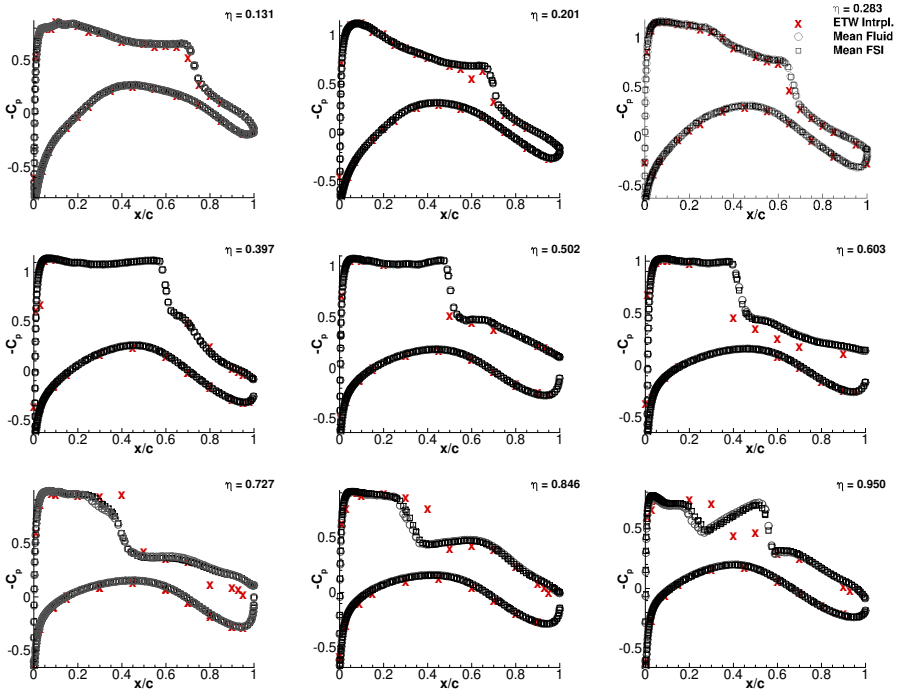

FIGURE 5.3. Surface pressure coefficient C_p at $\alpha = 3.75°$, comparing simulation and wind-tunnel test results for nine spanwise stations of starboard wing. Fluid-only and fluid-structure interaction (FSI) data are time-averaged signals from non-linear regime.

are clear differences between the static and time-averaged dynamic deformation. Third, the time-averaged dynamic deformation of the simulation agrees better with the experimental data overall, in particular for the port wing, which makes sense in that also the experimental data relate to some mean deformation. Figure 5.3 describes the corresponding surface pressure coefficient C_p at nine spanwise stations. The numerical data include results from both time-averaged fluid-only and fluid-structure interaction simulations. Again three observations can easily be made. First, the experimental pressure sensors are rather sparse in the mid semi-span stations. This has been discussed previously [95, 163]. Second, the differences in the time-averaged pressures from the fluid-only and fluid-structure coupled simulation are rather small, almost indistinguishable, which does not seem unreasonable considering the proximity of the simulations to the shock-buffet onset angle of attack. Third, while the level of agreement between simulation and experiment is acceptable overall, discrepancies are also noticeable, particularly for the stations outboard of approximately $\eta = 0.603$. As demonstrated in [95], this is the region where the shock-buffet unsteadiness was located, suggesting that better simulations, e.g. through more advanced turbulence modelling and eddy-resolving approaches, are needed in general. Having said this, these simulations are on a par with various other state-of-the-art solvers [163].

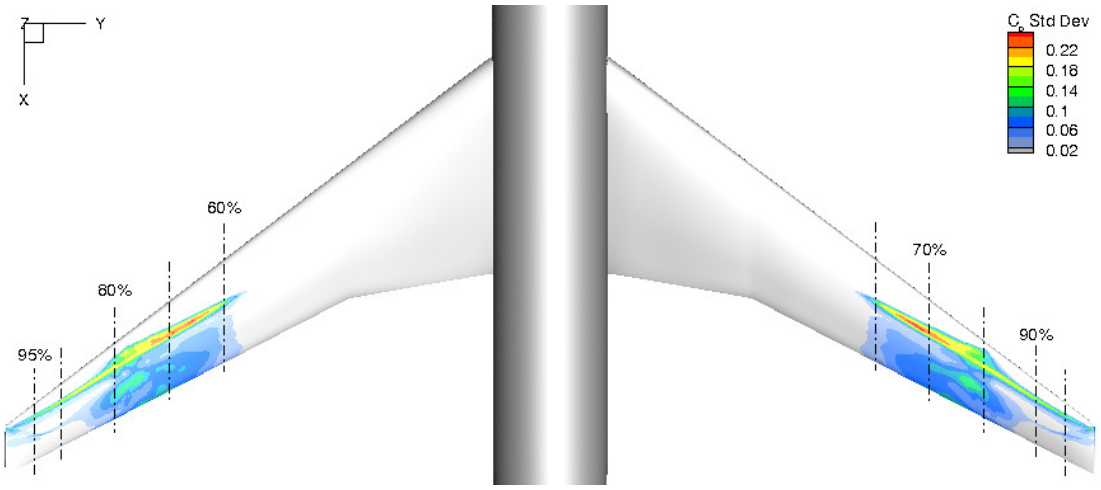

FIGURE 5.4. Standard deviation of surface pressure coefficient for rigid (yet statically deformed) (on the left) and flexible wing (right). Both wings depict the starboard wing (whereby the rigid wing has been mirrored for visualisation purposes).

5.3 Results

Figure 5.4 shows the standard deviation of the surface pressure coefficient. The figure presents the results on the starboard wing for both the fluid-only and fluid-structure coupled simulations. The fluid-only data have been mirrored for visualisation purposes only. High levels of an outboard-running (identified from instantaneous solution snapshots) shock unsteadiness can be observed outboard of approximately 60% semi-span. Fluctuations in the shear layer downstream of the shock front are obvious between approximately 60% and 80% semi-span, coinciding both with the highest fluctuation levels along the shock front in the figure and the coherent flow structures of shock buffet based on unstable global modes described in [9, 95]. Overall, the two simulations give similar spatial extent of flow activity with some subtle differences in the detail.

Figure 5.5 presents the time history of the lift and drag coefficient for both simulations along with the power spectral density estimates of the lift coefficient for both the linear and non-linear part of the signal. The fluid-only simulation was started from the deeply converged static aeroelastic solution with the statically deformed aircraft geometry kept frozen. During the initial linear stage (up until approximately 0.015 s), the integrated coefficients appear to be independent of the structural degrees-of-freedom, specifically the signals of fluid-only and fluid-structure coupled simulations are very similar, and effectively follow the shock-buffet dynamics as described by the dominating global instability. Indeed, this initial growth of the lift coefficient in the fluid-structure coupled simulation, compared with the signal reconstructed from the leading unstable global modes identified in [9], can be found on the left in figure 5.6. Note that the non-linear time-marching solution will start deviating from the flow-field reconstruction based on a linear eigenmode, when the amplitudes exceed some

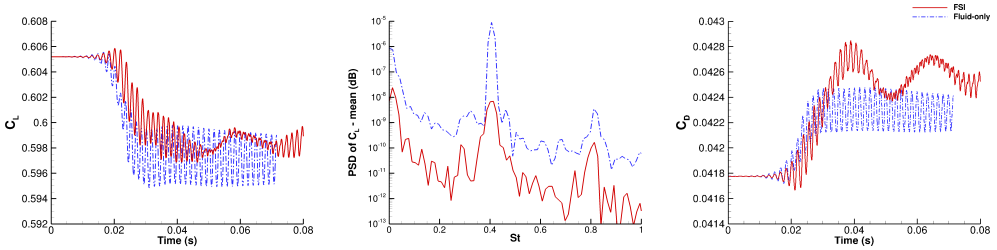

FIGURE 5.5. Time history of unsteady lift (left) and drag coefficient (right) for both fluid-structure interaction (FSI) and fluid-only simulations and power spectral density (PSD) over Strouhal number for non-linear part (> 0.0305 s) of lift coefficient (middle).

case-dependent threshold. A similar agreement was found between the time-accurate fluid-only simulation and corresponding signal reconstructed from the global modes. In fact, the entire coupled fluid-structure system initially responds to the aerodynamic global instability, which effectively agrees with the classical aeroelastic approach when dealing with self-excited and self-sustained flow unsteadiness, i.e. to regard the aerodynamic forcing function independent of the structural motion. The corresponding structural response is visualised for mode 20, arbitrarily chosen as a representative example, showing the modal amplitude factor, $q(t)$, of that mode on the right in figure 5.6. The same behaviour is observed in all structural modes, as can partly be seen in figure 5.7, including the first bending modes even though not visible therein due to the strong non-linear signal.Returning to figure 5.5, the non-linear part of the signal, here taken for time greater than 0.03 s, gives clear differences when including the flexible structure. First, the fluid-structure coupled solution results in lower-amplitude and more irregular instantaneous oscillations of the integrated coefficients. Second, the coupled results, besides the higher-frequency content, also reveal a low-frequency oscillation, possibly related to the dominant wing-bending deformation still present in the signal as visualised in figure 5.7. Third, the lift coefficient of the coupled simulation describes a slightly increased time-averaged response compared with the fluid-only simulation, as does the drag coefficient. The corresponding power spectral density estimates of the lift coefficient (with the corresponding frequency content for the drag coefficient appearing very similar) show strong peaks around the shock-buffet frequency range, as predicted by the global stability analyses [9, 95], and the first harmonic thereof. The fluid-structure coupled solution also gives a strong frequency activity, on a par with the magnitude of the shock-buffet peak, around the lowest structural modes.

Time histories of modal structural amplitudes for various different modes, corresponding to the modal shapes shown in figure 2.3, are presented in figure 5.7. Importantly, all structural modes that have been found to be unstable from the aeroelastic global stability analysis [9] are included, specifically modes 19, 20, 21, 27 and 28. The linear part of the signals has already been discussed and the shock-buffet dynamics drive the response. Concerning the (more visible) non-linear part and from the unsteady signals shown in the figure, it is evident that the lower-frequency structural modes show

FIGURE 5.6. Time response of lift coefficient for the coupled simulation (left) and modal amplitude of Mode 20 (right) along with signal based on leading unstable eigenvalue from global instability analysis in [9].

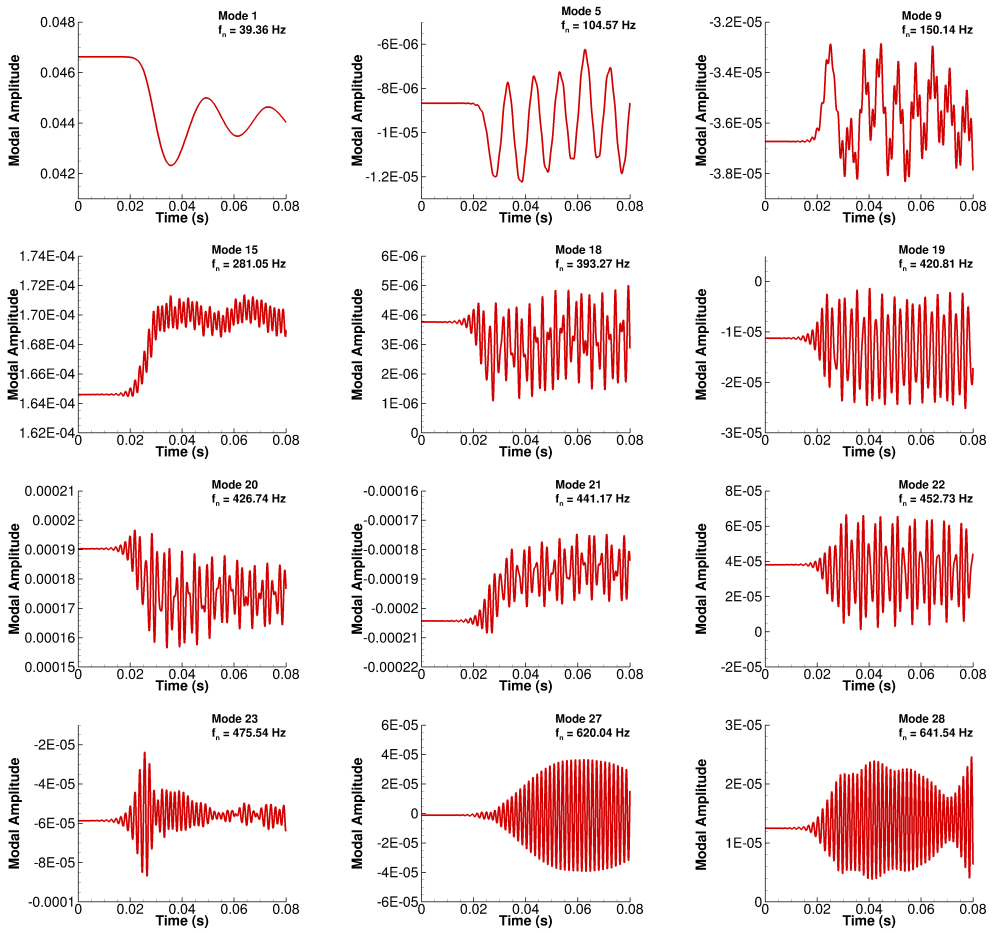

FIGURE 5.7. Modal amplitude response for a few select modes of interest. The wind-off structural frequency of each mode is indicated. Modes 19, 20, 21, 27 and 28 have been found to be unstable following the global stability analysis of [9].

little high-frequency content. The results of the characteristic higher-frequency shock-buffet forcing can be observed in the structural response for modes higher than, and including, mode 9 with a wind-off structural frequency of $f_n \geq 150.14\,\text{Hz}$ (corresponding to a Strouhal number of approximately $St = 0.1$). In combination with figure 5.8, which presents the frequency content of the modal structural amplitudes, the time-domain signals reveal some additional interesting features. In particular, modes 27 and

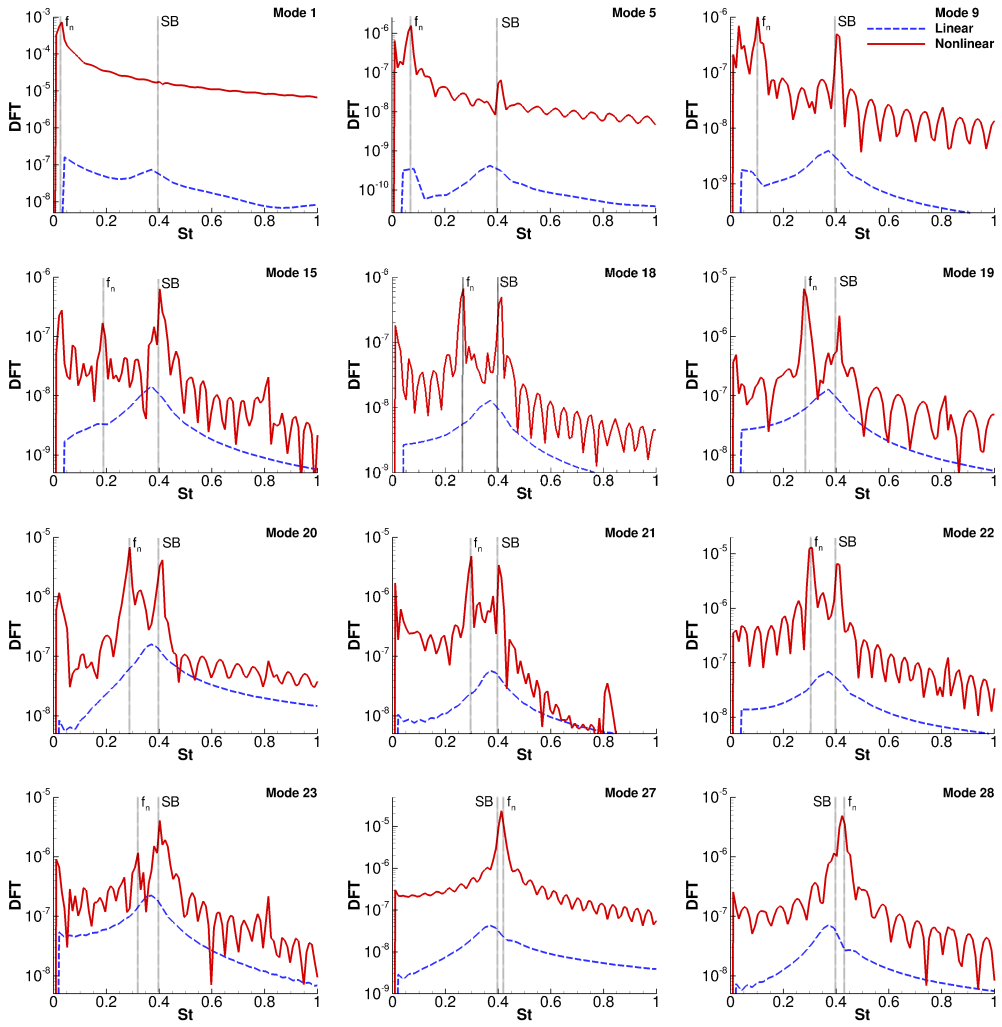

FIGURE 5.8. Discrete Fourier transforms (DFT) of modal amplitudes of selected structural modes of interest for both linear and non-linear part of signal. Linear and non-linear limits of the time signal are considered at $t \leq 0.015\,\mathrm{s}$ and $t \geq 0.03\,\mathrm{s}$, respectively. The frequency resolution for the linear and non-linear part is approximately $\Delta St = 0.03$ and 0.01, respectively. Vertical lines describe wind-off structural frequency, denoted f_n, and frequency of leading global shock-buffet mode (taken from [9]), denoted SB.

28, which were found to be strongly coupled with a marginally unstable fluid mode (indeed, including the flexible wing structure destabilised the otherwise stable fluid mode in the first place) seem to oscillate at a single frequency. This is confirmed in figure 5.8 through the frequency content. The remaining structural modes, besides those with lowest wind-off frequencies where the vibration close to structural eigenmode dominates, all suggest more than one dominant frequency in their response. Overall, irregular limit-cycle oscillations can be observed in most modal amplitudes, hinting at the intense structural buffeting response of the wind-tunnel model at those flow conditions.

Figure 5.8 shows the frequency content of the modal structural amplitudes for each of the selected representative modes. The figure gives results for both the linear and

non-linear part of the signal. Vertical lines indicate the Strouhal numbers of the respective wind-off structural frequencies (denoted $\mathbf{f_n}$) and the frequency of the shock-buffet mode (denoted **SB**), as predicted by global stability analysis of the coupled system. For the linear part, the signals show a single pronounced peak around the shock-buffet frequency. The relatively smaller number of time-steps of the linear part, compared to the longer signal of the nonlinear response, results in a wider frequency peak for the linear response.For the lower-frequency structural modes, activity can also be noted around the respective wind-off frequencies, which seems to be an artefact of choosing an appropriate time interval since the structural response will eventually kick in. A different behaviour is revealed for the non-linear part altogether. Starting at mode 1 from the structural system, a single peak near its natural frequency is observed. As the structural frequencies increase, a mild peak around the shock-buffet frequency first appears for mode 5 while becoming more pronounced for modes 9 and above. A single strong peak near the shock-buffet frequency can be seen for the two highest frequency modes 27 and 28, whose wind-off frequencies are close to that of the flow instability. In addition to the responses related to either wind-off modal vibration or shock buffet, a relatively large response at the first bending modes can also be observed for most modes.

The instantaneous steady surface pressure plots demonstrate the flow behaviour over one cycle at the frequency of the global instability. The latter is calculated to be 0.00168 s using the frequency of the global instability ($St \approx 0.4$). In both figures 5.10 and 5.9, eight timesteps over one period from 0.0600 s to 0.0616 s in steps of 0.0002 s are shown, making the first and last subfigures of each plot showing the same point of one cycle. Figure 5.9 gives the surface C_P along with isolines that mark C_F reversal and therefore enclose the separated areas. The contours reveal a typical transonic pressure distribution where the low pressure supersonic pocket of air is formed from the leading edge and is terminated with an abrupt pressure increase at the shock wave. The shock front moves in the chordwise direction throughout the cycle. This can be observed better by focusing on the separated area outboard of the yehudi break which grows in area, reaching the largest separated area for $t = 0.0610s$. At this point the shock front of the large separated area is the closest to the leading edge before the area breaking into smaller separated pockets that travel outboard and in return moving the shock front towards the leading edge again. Figure 5.10 shows contours of $C_P{}' = C_P - C_{Pmean}$. The alternating pressure along the shockwave translates to an upstream shock movement for a positive $+C_P{}'$ and a downstream movement for a negative $-C_P{}'$. Using this visualisation, buffet cells that emanate from the area outboard of the localised instability and their spanwise convection become easier to see. In addition, the alternating values of $C_P{}'$ behind the shock front show the periodic behaviour of the separation bubbles before they are shed from the trailing edge.

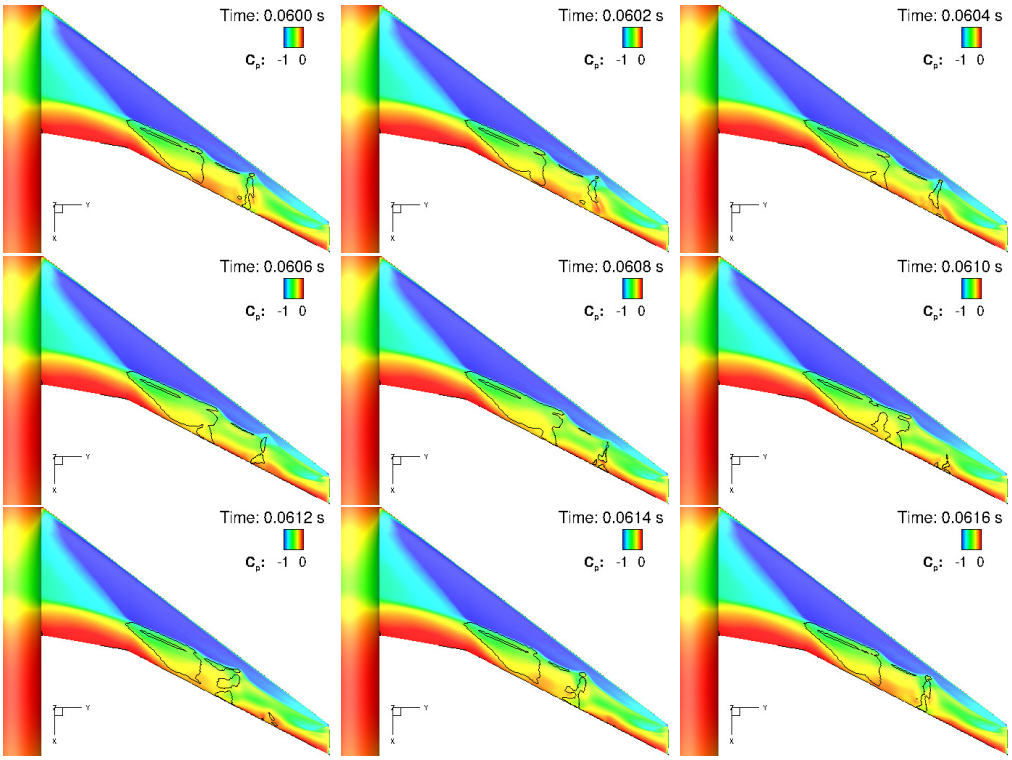

FIGURE 5.9. Time-accurate computed surface C_P for nine timesteps over one cycle of shock buffet. The C_F isolines indicate the separated area.

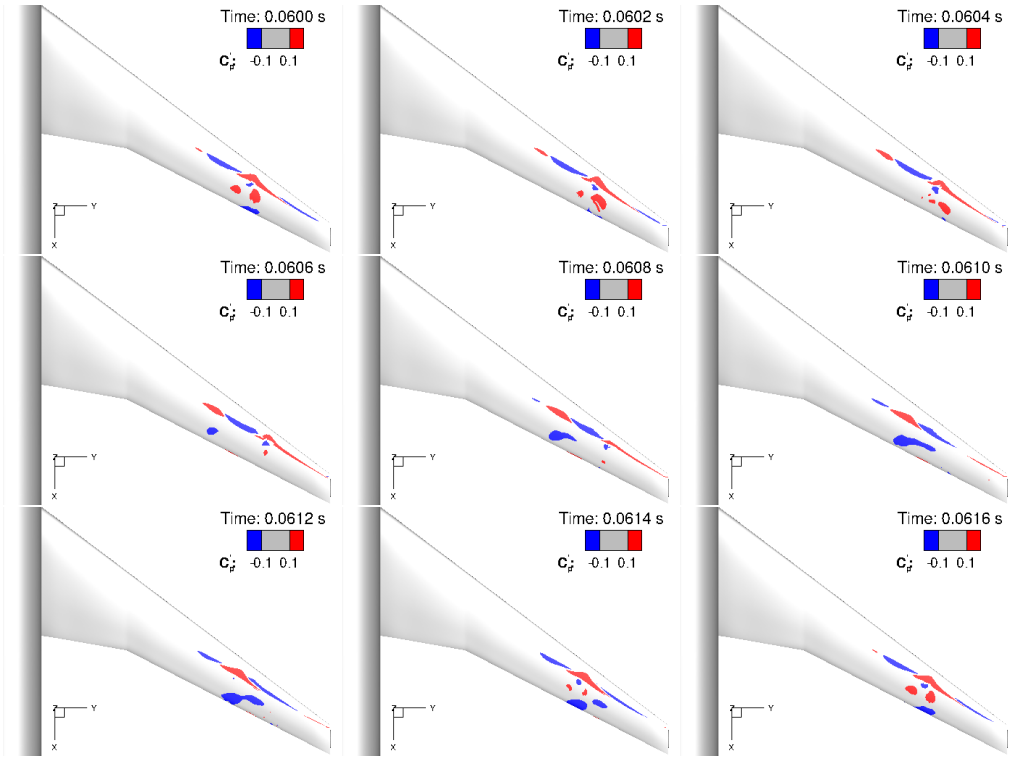

FIGURE 5.10. Time-accurate computed surface $C_P{}' = C_P - C_{Pmean}$ for nine timesteps over one cycle of shock buffet.

5.4 Summary of Fluid-Structure Interaction

The dynamic interaction of a flexible aircraft model and the self-sustained flow unsteadiness was investigated in this chapter. For this, unsteady fluid-structure coupled and fluid-only simulations were carried out using the NASA CRM for conditions beyond shock-buffet onset. Basic validation of the static and time-averaged dynamic simulations with experimental data from a wind-tunnel experiment revealed a good agreement overall. Scrutinising both integrated force coefficients of lift and drag and temporal amplitudes of the structural modes shows that the linear part of the signals is strongly dominated by the global shock-buffet instability, when started from a well converged static aeroelastic solution. In the non-linear regime, on the other hand, frequency content of the integrated coefficients becomes more broadband, revealing higher activity not only in the shock-buffet range but also near the first bending modes, with lower instantaneous oscillation amplitudes overall. The non-linear behaviour of the structural modes (strictly speaking, the interaction of the non-linear aerodynamic loads with the linear structural modes) strongly depends on their respective wind-off frequencies. For structural modes oscillating near the flow instability, a single strong peak is observed, in contrast to distinct peaks for structural vibration and flow instability for the more distant (in a frequency sense) structural modes. It is important to point out here that modes that have been found to be stable by a linear analysis of the coupled system, especially lower frequency modes, show responses at the shock buffet frequency in similar amplitudes to that of each structural frequency. Surface plots over one period of the high-frequency behaviour of shock buffet demonstrate the typical outboard running buffet cells creating waves along the shock front. The skin friction isolines capture the outboard growth of the separated flow area before it splits into smaller separation pockets that convect downstream.

Chapter 6

Transient Growth

In this chapter, a novel study on the amplification of linear optimal disturbances in steady turbulent flows for a supercritical aerofoil is presented. Unsteadiness observed in open-flows can be classified into two categories depending on the flow behaviour [164]. When the unsteadiness results from the intrinsic dynamics of the flow then that flow is referred to as an oscillator whereas when the unsteadiness is caused by the amplification of existing upstream noise, it is said to be behaving as a noise-amplifier. The instabilities that were introduced to describe the dynamics of oscillators and noise-amplifiers, are referred to as absolute and convective instabilities, respectively [164]. Modal stability analysis, namely the classification of the flow stability depending on the existence (or absence) of exponentially growing eigenmodes, has proven to be successful in identifying absolute instabilities depending on some critical parameters (e.g. Reynolds number or angle of attack). Yet, this type of analysis was only adequate to describe the asymptotic behaviour of the flow something that was also supported by discrepancies with modal stability analysis results observed experimentally for Poiseuille and Couette flows where unsteadiness would occur before the critical Reynolds number was reached. Therefore, in the late 1980s/early 1990s it was recognised that the superposition of the non-normal eigenmodes that characterise the discrete linearised Navier-Stokes operator could cause short time energy growth even for an asymptotically stable system [128]. Since noise-amplifier dynamics can be observed for such asymptotically stable flows, the analysis of the pseudospectra [123] of the linearised operator became vital in identifying convective instabilities and seeing the whole picture alongside modal stability analysis. Two different types of analyses pertaining to the pseudospectra of the linear operator exist and they comprise what is termed as nonmodal stability analysis. Conversely to modal stability analysis, that focuses on the behaviour of individual eigenmodes, the singular values and vectors of each formulation (to be explained shortly) of the linearised operator are at the forefront of nonmodal

stability analysis. The first type involves the external forcing of the system, something required to sustain the unsteadiness for an asymptotically stable system, and is used to scrutinise the flow response at selected forcing frequencies. This is referred to as resolvent analysis for which the resolvent operator is defined as $\mathcal{R} = (i\omega - \mathcal{A})^{-1}$ where ω is the forcing frequency and $\mathcal{A}$ the linearised operator [118]. The second type, focuses on the short-time behaviour of the system by solving the initial value problem

$$\frac{\partial}{\partial t}\boldsymbol{q}'_f = J\boldsymbol{q}'_f \tag{6.1}$$

This is referred to as transient growth or nonmodal analysis and it involves the propagator operator, a term used to refer to the linearised operator matrix exponential $e^{\mathcal{A}}$ [117]. Transient growth analysis is usually applied to laminar flows in order to assess if the superposition of decaying modes can cause transition to turbulent flow before eigenmodal growth dominates, a phenomenon referred to as bypass transition [165]. Transition prediction methods are based on linear stability theory which can predict the exponential growth of viscous instabilities in the form of travelling waves known as Tollmien–Schlichting (TS) waves [166, 167]. However this is only the initial stage of transition to turbulence because the growth of TS waves is followed by a secondary instability that will cause vortical structures to appear. These structures will eventually form turbulent spots [168]. Since the distance between the region where TS waves appear and the actual breakdown to turbulence can be small, methods based on linear stability theory are more practical when it comes to transition prediction. A method largely used in industry to define the onset of transition is the one suggested by Smith and Gamberoni [169] and Van Ingen [170] known as the e^N method. This is based on calculating the total growth of all unstable modes at different frequencies using linear stability theory. Once this growth is larger than a threshold e^N that is empirically defined using wind tunnel or flight test data, transition is considered to occur. The growth rate of an unstable perturbation can be determined when the perturbation amplitude is amplified when travelling downstream. For incompressible flows, N-factors range from 9 to 10 for TS waves [171] and 4 to 5 for crossflow instabilities [172]. Therefore, in transient growth analysis, a bypass transition scenario is considered possible when the maximum energy growth achieved at short times is large enough to yield a considerable N-factor.

In hydrodynamic stability studies, the term unsteadiness refers to high frequency disturbances at small spatial scales that are responsible for the flow transition from a laminar to a turbulent state at low to moderate Reynolds numbers. Generally, even though the perturbations that cause transition have various scales with varying degrees of spatial and temporal coherence, a clear separation between large-scale global structures resulting from external forcing and small scale instabilities originating in the shear

layer as sublayer streaks, is assumed [173]. This is summarised in the triple decomposition [174,175] that decomposes the flow into a mean state, a coherent fluctuation and an incoherent fluctuation i.e.

$$\boldsymbol{q}_f = \overline{\boldsymbol{q}}_f + \boldsymbol{q}'_f + \boldsymbol{q}''_f \tag{6.2}$$

Therefore, in conditions where steady yet turbulent states exist and the small scale disturbances are accounted for by the turbulence model, the resulting decoupling of scales allows to redefine the term unsteadiness to refer to low frequency self-sustained and self-excited oscillations of the large-scale coherent structures, as it has been demonstrated [11] in the case of transonic buffet. Since a similar steady turbulent equilibrium point is considered herein, the term unsteadiness is associated with the aforementioned definition. Lastly, it has been shown that these large-scale global structures in turbulent flows can also experience transient growth [176].

The next sections of this chapter are organised as follows. Firstly, the transient growth code is verified using a supplied Jacobian matrix for Plane Poiseuille flow. The verification is then extended to a cylinder flow. This is in order to compare the optimal transient modes in addition to the optimal energy growth by using a large and sparse linear operator. The literature results available for comparison for the cylinder case are for incompressible flow whereas the results presented herein are for a low Mach number of 0.2 due to limitations of the finite volume code employed. Finally, transient growth results along with optimal transient growth modes are presented for the supercritical aerofoil OAT15A. Modal stability results are presented along transient growth results for all tests cases.

6.1 Verification

6.1.1 Plane Poiseuille Flow

To verify the transient growth code, a Jacobian matrix of Plane Poiseuille Flow (PPF) along with the associated integral weights for the energy norm that was supplied by Dr. Helio Quintanilha Jr is used. By solving the Orr-Sommerfeld equation, the theoretical critical Reynolds number at which transition occurs for PPF is 5772 [177] but numerous experiments [178–180] have shown that finite-amplitude disturbances can drive transition to turbulence at Reynolds numbers as low as 1000. This was later attributed to short time energy growth due to the non-normality of the governing linear operator [10]. The linear operator used herein is for a subcritcal case for a Reynolds

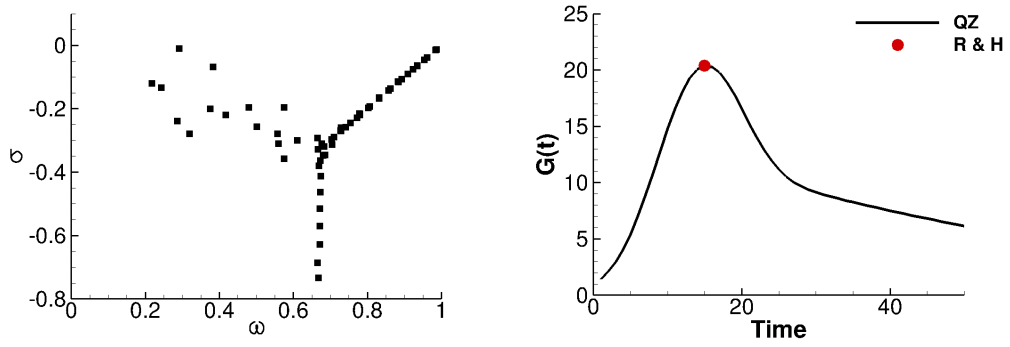

FIGURE 6.1. Eigenvalue spectra of plane Poiseuille flow for $Re = 3000$ (left) and associated energy growth curve (right). The red dot corresponds to the optimal value of $G(t) = 20.37$ computed by Reddy and Henningson [10].

number of 3000. The small size of the problem allows the use of direct methods for the eigenvalue computation. Specifically, the generalised Schur decomposition or QZ algorithm [181] is employed in MATLAB. Figure 6.1 shows the eigenspectrum of the linear operator and energy gain which is excellent agreement with the maximum energy gain of $G(t) = 20.37$ computed by Reddy and Henningson [10].

6.1.2 Cylinder Flow

Modal stability calculation

The flow around a cylinder is a commonly used test case for the verification of modal stability analysis results. Numerical studies demonstrate that a global instability arises above a critical Reynolds number of $Re \approx 47$ [11,12,182] something that is in agreement with experimental observations [183]. Figure 6.2 shows contours of the u-velocity base flow component compared to literature for a Mach number of 0.2 and a subcritical Reynolds number $Re = 45$.

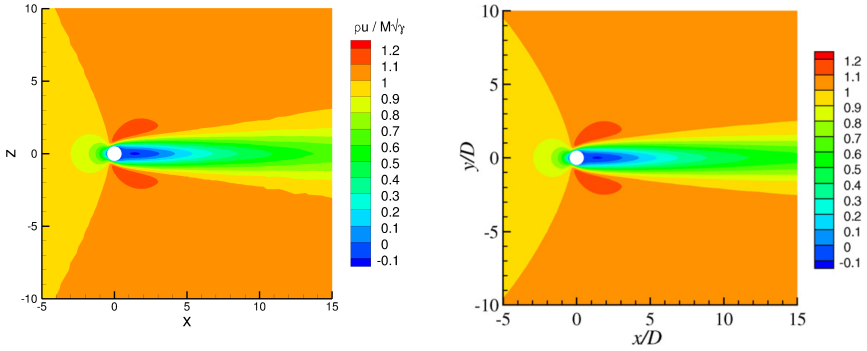

FIGURE 6.2. Contours of the momentum component in the x-direction normalised by the compressibility correction $\rho u/M\sqrt{\gamma}$ (left) using DLR-TAU and streamwise velocity from Crouch et al. [11] for conditions: $Re = 45$, $M_\infty = 0.2$

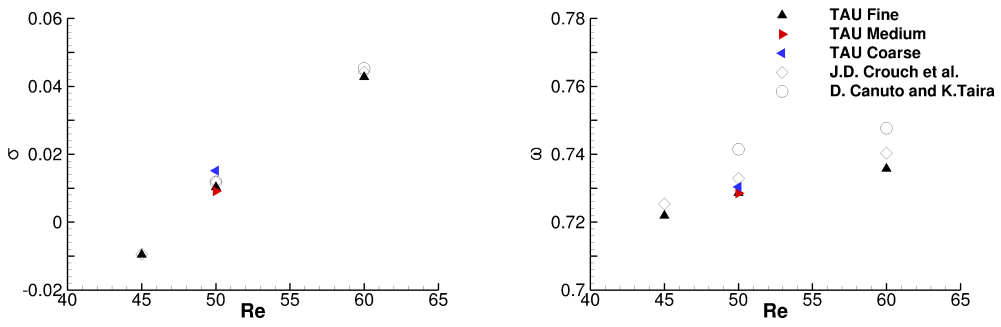

(a) Growth rate (b) Frequency

FIGURE 6.4. Reynolds number dependence of the growth rate and frequency of the critical eigenvalue for a Mach number of 0.2, compared with results from Crouch et al. [11] and Canuto and Taira (DNS) [12].The effects of varying the grid resolution are shown for $Re = 50$.

A comparison of the real and imaginary part of the critical eigenvalue compared to literature for different Reynolds numbers is shown in figure 6.4. In addition, the sensitivity of the eigenvalue on grid resolution is also presented for a Reynolds number $Re = 50$. The names fine, medium and coarse denote mesh sizes of 66×10^3, 45×10^3 and 10×10^3 points, respectively. Finally, the eigenmode associated with the unstable eigenvalue for a Reynolds number $Re = 60$ and a Mach number of 0.2, compared to literature is shown in figure 6.3. Since the systems used herein are large and sparse, the Shift-and-Invert Arnoldi method, presented in section 2, is used to focus at certain parts of the spectrum, close to the critical eigenvalue. It is important to point out here that the results in figures 6.2 and 6.3 have been normalised by a compressibility scaling factor defined as $M(\sqrt{\gamma})$ that was introduced in DLR-TAU. Results are in good agreement with literature.

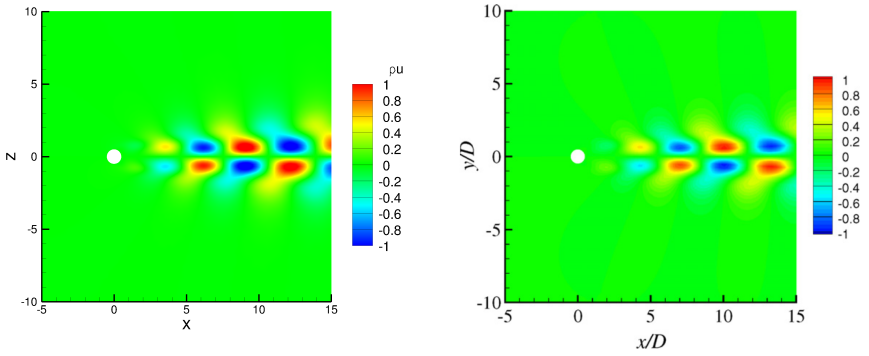

FIGURE 6.3. Contours of the real part of the perturbation momentum component in the x-direction ρu (left) using DLR-TAU and streamwise velocity (right) from Crouch et al. [11] for conditions: $Re = 60$, $M_\infty = 0.2$

Transient growth calculation

The energy gain and optimal transient growth modes are compared against literature next. Although the available results are for incompressible conditions, the use of such a setting poses a limitation on the solution accuracy of the finite volume code DLR-TAU, since the low Mach number preconditioner is not differentiated, hence the Jacobian matrix would not be correct. Therefore, results are compared for the lowest permissible Mach number of 0.2, where density can be assumed to be constant [144]. Figure 6.5 shows the variation of the energy gain over time along with literature results for steady and unsteady flow at Reynolds numbers of 45 and 50, respectively. A similar behaviour can be observed for the two conditions, although for a Mach number of 0.2, G_{max} is lower and is achieved at later times. Specifically, for incompressible flow, the maximum energy growth for the subcritical case of $Re = 45$ is $G_{max} = 3357$ achieved at $t = 102$ whereas for a Mach number of 0.2, $G_{max} = 191$ and is achieved at $t = 250$ for a Mach number of 0.2. This also holds for the unsteady condition of $Re = 50$ where higher energy gain can be seen for the incompressible case. This is due to the small yet non-negligible compressibility effects, since it has been shown that for a given Reynolds number, the growth rate decreases with increasing Mach number [12]. Nevertheless, transient growth dominates at short times in both cases. Similarly to the PPF case, it can be seen that at longer times the energy gain is governed by the growth (or decay) rate of the critical eigenvalue for both steady and unsteady conditions.

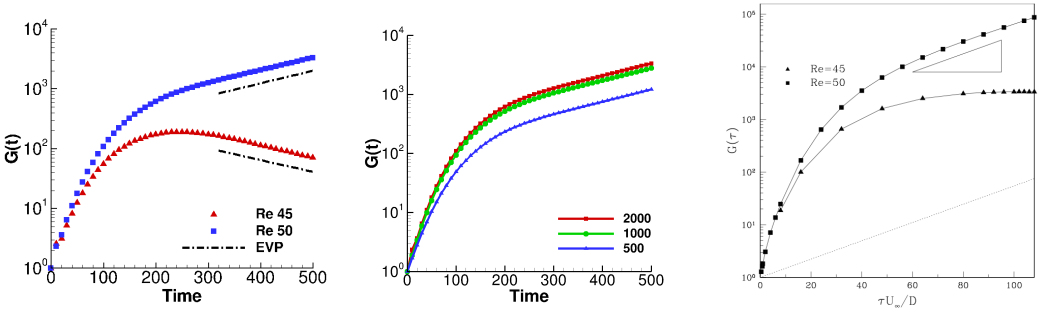

(a) Energy gain for $M_\infty = 0.2$ (b) Subspace convergence (c) Energy gain for incompressible flow

FIGURE 6.5. Comparison of energy gain for low compressibility conditions $M_\infty = 0.2$ (a) and incompressible flow (c) from Abdessemed et al. [13] at steady $Re = 45$ and unsteady $Re = 50$ conditions. The dashed line represents the slope of the most unstable eigenvalue calculated from the EVP analysis. Krylov subspace convergence is shown for three different subspace sizes in (b).

The slope of the asymptotic growth is related to the eigenvalue growth rate σ as

$$\lim_{t\to\infty} G(t) \propto e^{2\sigma t} \tag{6.3}$$

The factor of two (2) in the equation arises due to the squaring of the energy norm.

The rate of decay of the energy norm squared is twice the rate of decay of the energy norm itself. Therefore, the factor of two accounts for this relationship. In addition, as discussed in section 2, the computation of transient growth requires the evaluation of the matrix exponential that is based on the eigenvalue decomposition of the linear operator. Therefore, this calculation is restricted by the size of the Krylov subspace since a selected number of eigenmodes is used.

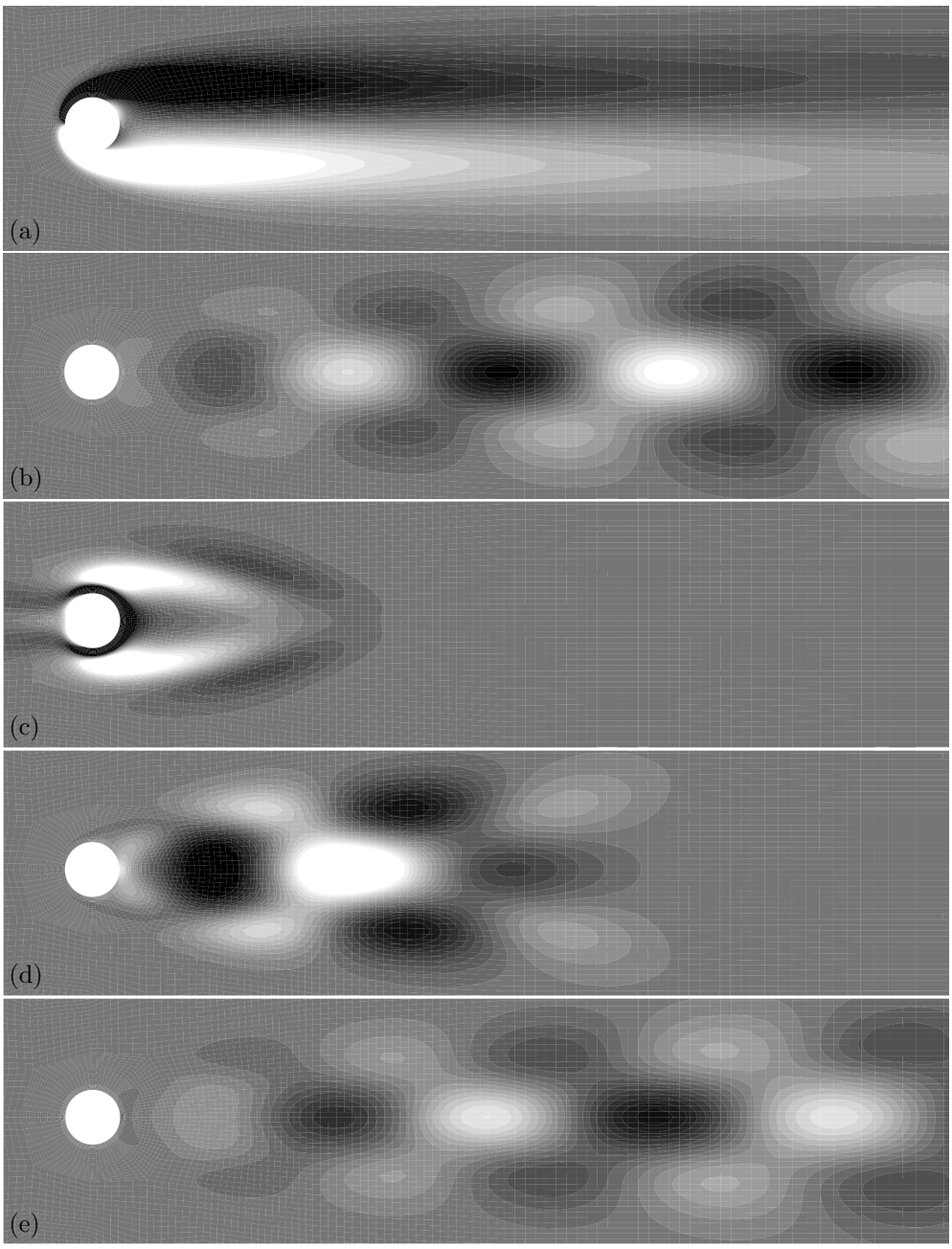

FIGURE 6.6. Spanwise vorticity contours for incompressible flow at $Re = 50$ taken from Abdessemed et al. [13] showing: (a) base flow, (b) leading eigenmode, (c) optimal initial condition at $t = 8$, (d) optimal response at $t = 8$ and (e) optimal response at $t = 32$.

The variation of the energy gain depending on the subspace size is shown in figure 6.5(b) for $Re = 50$. It can be seen that, while the response demonstrates similar behaviour, the energy gain is underpredicted for the smallest subspace size of 500 eigenmodes. Increasing the subspace size to 1000 eigenmodes a higher energy gain can be seen. Finally, a further subspace size increase by including another 1000 eigenmodes (total of 2000) seems to have a small effect, hinting that the correct value of the energy curve is recovered.

Figures 6.6 and 6.7 show spanwise vorticity contours comparing the modal and nonmodal stability analysis results at $Re = 50$ for incompressible flow from literature and the $M_\infty = 0.2$ case, respectively. Figures 6.6(a) and 6.7(a) show the base flow vorticity whereas the vorticity of the leading eigenmode of the linear operator that eventually evolves into the von Kàrmàn vortex street is shown in figures 6.6(b) and 6.7(b). Figures 6.6(c) and 6.7(c) show the vorticity of the optimal initial condition at $t = 8$ for incompressible flow and $t = 20$ for the $M_\infty = 0.2$ case. In both cases, the region around the boundary layer separation and near wake demonstrates high energy concentration something identified in the adjoint analysis of cylinder flow in previous studies [184, 185]. Even though both of these integration times are considered to be relatively short, the latter was chosen at a larger time since figure 6.5(a) shows that transient growth occurs at larger times for a Mach number of 0.2. Nevertheless, for each chosen time, these initial modes evolve into the optimal response modes shown in figures 6.6(d) and 6.7(d). Finally, figures 6.6(e) and 6.7(e) show the optimal response mode for larger integration times, specifically at $t = 32$ and $t = 80$ for incompressible flow and $M_\infty = 0.2$, respectively. As expected from the energy gain behaviour seen in figure 6.5(a), the optimal response modes evolve into the pattern associated with the leading eigenmode since at these times the response is governed by the leading eigenvalue. It is important to point out here that small spatial discrepancies observed are due to the wake elongation and separation delay caused for an increasing Mach number [12]. Overall, good agreement with literature can be seen.

6.2 Supercritical aerofoil OAT15A

After completing the code verification, transient growth analysis is applied to the supercritical aerofoil OAT15A at transonic conditions in the following section. Experimental [38] and numerical studies [14, 42, 55, 90] on that geometry have shown that shock buffet occurs for angles of attack higher and including 3.5°. The conditions are chosen according to the set up of the wind tunnel experiments and are a Reynolds number of 3.2×10^6 and a Mach number of 0.73. Herein, transient growth results are presented for a sweep of angles of attack at these conditions ranging from 2.75° to 4°.

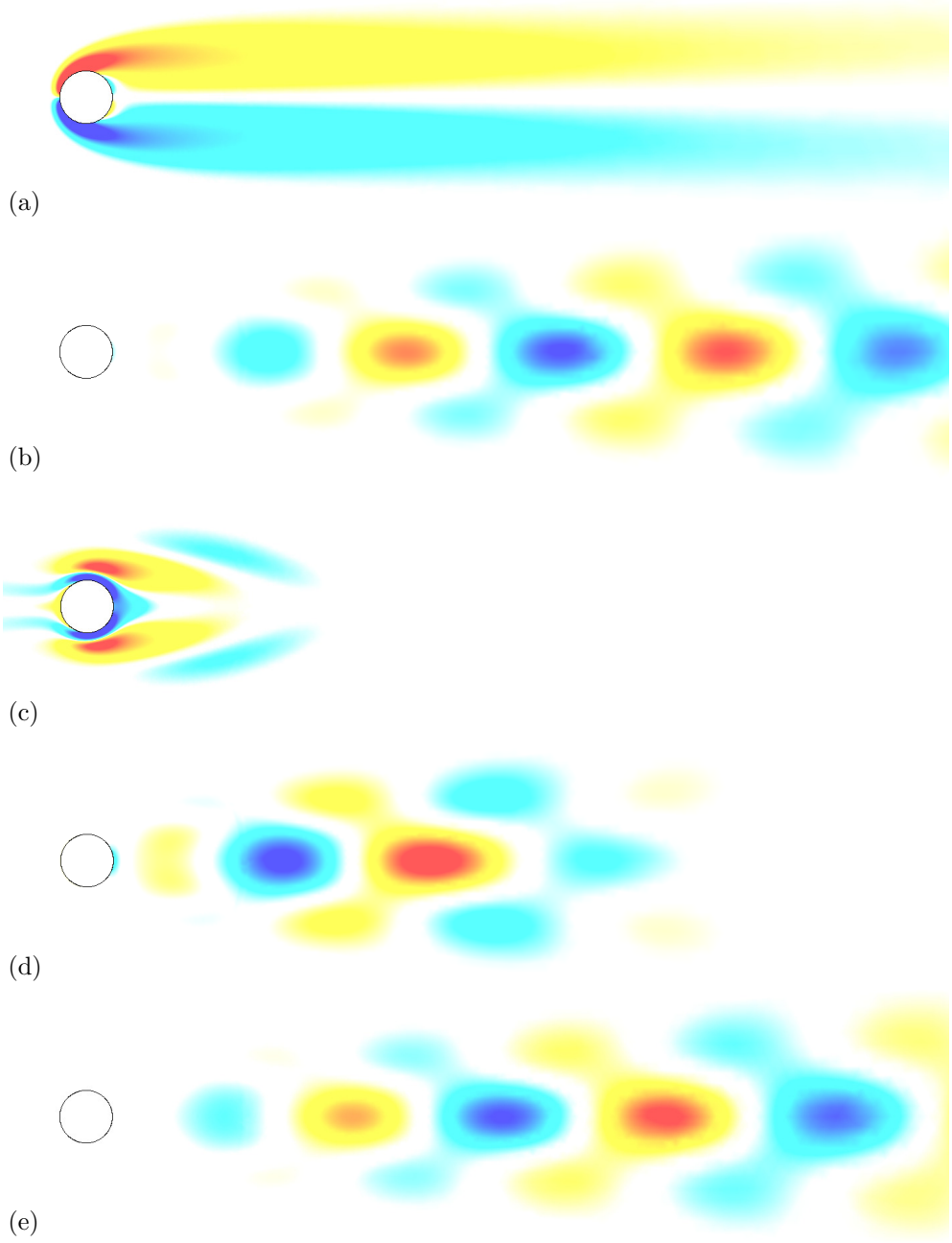

FIGURE 6.7. Spanwise vorticity contours for a Mach number of 0.2 at $Re = 50$ showing: (a) base flow, (b) leading eigenmode, (c) optimal initial condition at $t = 20$, (d) optimal response at $t = 20$ and (e) optimal response at $t = 80$.

Modal stability calculation

Modal stability results are shown in figure 6.9. There it can be seen that as the angle of attack is increased, only the eigenvalue in the shock buffet frequency range is migrating towards the unstable half plane. The flow is globally stable for angles of attack up to

$\alpha \approx 3.4°$, with the instability onset due to a Hopf bifurcation [11] occurring for angles higher and including $\alpha = 3.5°$. The associated direct and adjoint modes near buffet onset are in accordance with literature and are shown in figure 6.8.

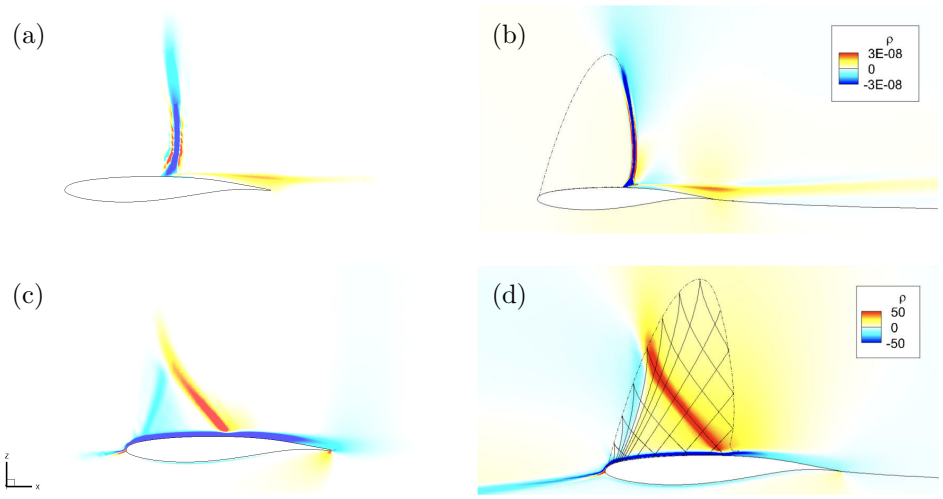

FIGURE 6.8. Real parts of density components for direct (a) and adjoint (c) unstable global modes for $\alpha = 3.5°$ using DLR-TAU, compared to results from Sartor et al. [14] (b) and (d),respectively at conditions: $Re = 3.2 \times 10^6$, $M_\infty = 0.73$.

The direct global mode appears to be most energetic within the shock along with a small contribution in the mixing layer. The inherent nonnormality of the Jacobian due to the presence of the convection operator in the governing equations, results in the downstream propagation of disturbances in the direct global mode and the upstream disturbance propagation in the adjoint global mode, respectively [186]. As a result, the adjoint mode indicates the region where the manipulation of the flow by harmonic forcing will have the strongest effect on the oscillation amplitude or frequency of the unstable global mode [187]. Herein, this region appears to be located on the suction side, specifically in the boundary layer and in the supersonic region. The mode has a triangular shape in the supersonic region, with the edges following the boundary layer on the lower part, the edge of the supersonic flow region on the upstream side while an oblique line starting from the shock foot where the boundary layer separation is located can be seen on the downstream side.

Transient growth calculation

The corresponding energy gain as a function of non-dimensional time for each angle of attack shown in figure 6.9 can be seen in figure 6.10(a). It is worth reiterating the physical interpretation of the energy gain $G(t)$ here, which is the factor by which the energy of an optimal initial perturbation (or right singular mode) will grow at a given

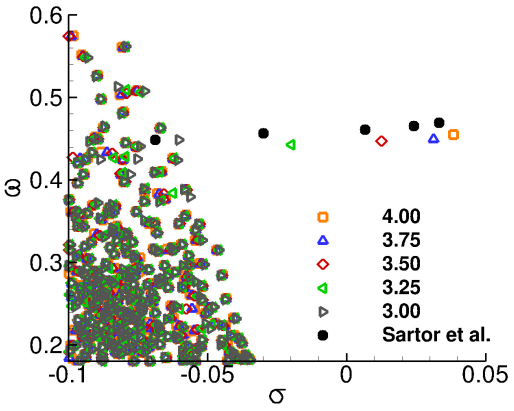

FIGURE 6.9. Eigenvalue spectra for increasing angle of attack for the OAT15A, compared with results from Sartor et al. [14] at conditions: $Re = 3.2 \times 10^6$, $M_\infty = 0.73$.

time t [13]. Similar to the cylinder case, we can observe that the singular value at $t \to 0$ is $\lim_{t\to 0} G(t) = 1$ and therefore no energy growth is recovered at $t = 0$ for all curves. For subcritical angles of attack ($\alpha < 3.5°$), the maximum transient growth G_{max} increases as the angle of attack is increased, reaching a maximum of $G_{max} = 50.4$ at $t = 46$ for the highest subcritical angle of attack $\alpha = 3.25°$ shown here. The critical eigenvalue governs the response in the modal limit ($t > 80$) with the latter increasing or decaying according to the growth rate accordingly, for angles above and including $\alpha = 3.25°$. As it can be seen in figure 6.9, for the two lowest angles of attack, namely $\alpha = 3.0°$ and $2.75°$, the critical eigenvalue is still located inside the cluster of eigenvalues, and therefore the decay rate of the gain is not governed by that of the critical eigenvalue. In addition, as incidence is increased, G_{max} occurs at later times. For angles of attack post shock buffet onset, the initial transient growth is overtaken by exponential growth according to the eigenvalue growth rate.

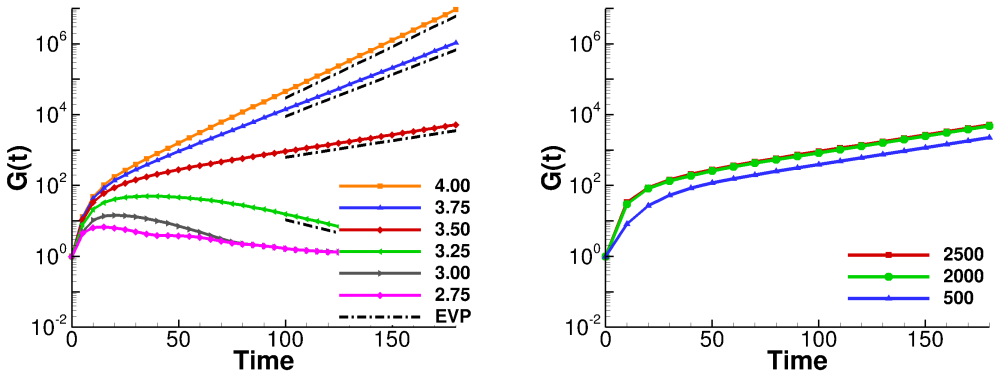

(a) Energy gain (b) Subspace convergence

FIGURE 6.10. Variation of optimal energy gain for a range of angles of attack for OAT15A at conditions: $Re = 3.2 \times 10^6$, $M_\infty = 0.73$. The dashed line represents the slope of the most unstable eigenvalue calculated from the EVP analysis.Krylov subspace convergence is shown for three different subspace sizes.

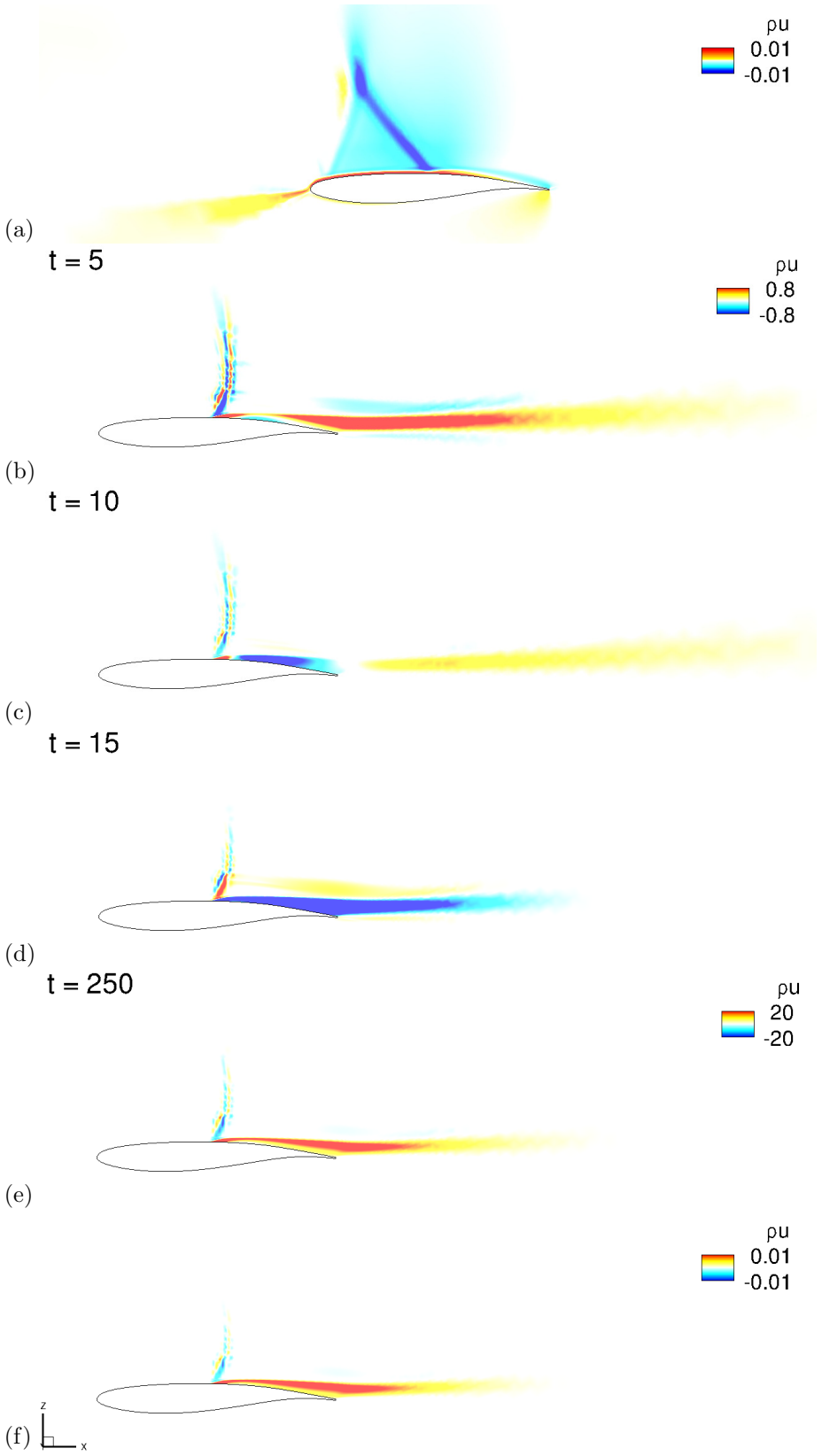

FIGURE 6.11. Contours of the real part of the momentum component ρu in the x-direction for $\alpha = 3.5°$ at conditions: $Re = 3.2 \times 10^6$, $M_\infty = 0.73$ showing: (a) optimal initial condition at $t = 5$, optimal responses at (b) $t = 5$, (c) $t = 10$, (d) $t = 15$, (e) $t = 250$ and (f) leading eigenmode. The minimum and maximum values of ρu are kept the same for $t = 5, 10$ and 15.

Figure 6.11 shows contours of the the real part of the horizontal momentum of optimal transient growth modes near buffet onset for $\alpha = 3.5°$. Specifically, figure 6.11(a) shows the initial optimal growth mode at $t = 5$, the spatial distribution of which, as expected, resembles that of the adjoint mode shown in figure 6.8, since perturbations affecting the areas of highest sensitivity will result in the largest energy growth. This is the only initial optimal growth mode shown as the same modes for the rest of the integration times presented demonstrate similar spatial distribution and only differ quantitatively. Figures 6.11(b)-6.11(d) show the optimal growth modes for different short integration times. Firstly, it can be seen that for all times the modes are most energetic within the shock wave and the recirculation bubble. As the time increases, the ripples seen for $t = 5$ above the shock foot fade as they cluster around the shock wave while the mode component present in the wake contracts towards the trailing edge. Additionally, the recirculation bubble component of the mode can be seen to grow in length from $t = 10$ to $t = 15$. Finally, figure 6.11(e) shows that for the longer time interval $t = 250$, where the response is governed by the modal exponential growth, the optimal growth mode has evolved into the pattern associated with the leading eigenmode shown in figure 6.11(f).

The dependence on angle of attack of the maximum value reached by $G(t)$ is examined next. The energy gain is computed for three additional subcritical angles of attack, namely $\alpha = 2.85°, 3.10°$ and $3.35°$, and is shown in figure 6.12 along with the subcritical $G(t)$ curves from figure 6.10(a).

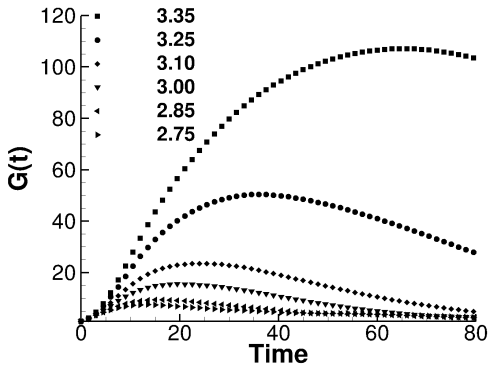

FIGURE 6.12. Variation of optimal energy gain for subcritical angles of attack at conditions: $Re = 3.2 \times 10^6$,$M_\infty = 0.73$.

For the highest angle of attack presented herein $\alpha = 3.35°$, initial transient growth of over two orders of magnitude occurs, reaching $G_{max} = 107.1$. As mentioned earlier, the e^N method is used to predict the onset of transition to turbulence, therefore calculating the N-factor would not be applicable in the steady turbulent conditions investigated in the present study. Nevertheless, it is still of interest to investigate transient growth behaviour in such conditions. Figure 6.13(a) shows the dependence of G_{max} on α for all

subcritical angles of attack. This dependence, for the transonic regime studied herein, is found to be quartic,

$$G_{max} \sim \alpha^4 \tag{6.4}$$

as can be seen in the curve fit. This result demonstrates that, even though nonmodal energy growth is moderate in the present regime, it becomes more significant as the angle of attack increases. Ultimately, since nonmodal analysis showcases the amplification of optimal perturbations, this could inform experimental campaigns conducted in wind tunnels, where high levels of environmental perturbations are present. Interestingly, this is similar to the quartic dependence of G_{max} on local Reynolds number found in the work of Quintanilha et al. [15] in laminar hypersonic flow conditions in contrast to the quadratic dependence of maximum energy gain on Reynolds number known from incompressible analysis [124].

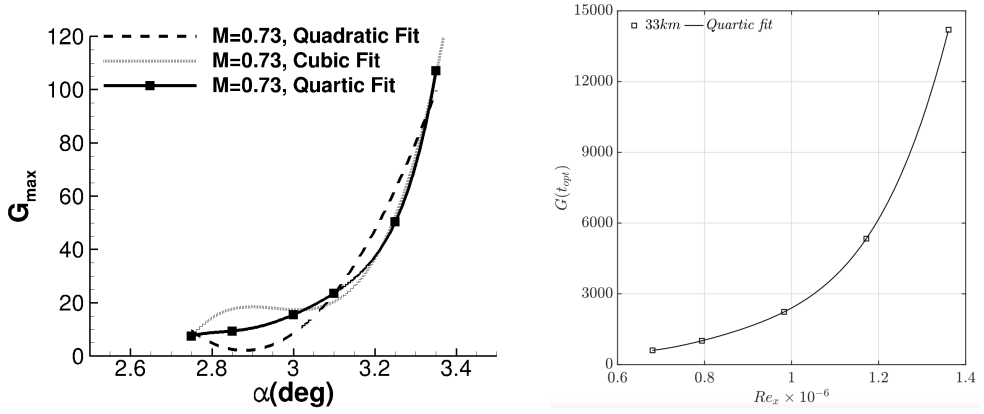

(a) Angle of attack dependence of G_{max}

(b) Reynolds number dependence of G_{max}

FIGURE 6.13. Comparison of best fit for the maximum gain G_{max} as function of angle of attack α for steady turbulent conditions and G_{max} as function of local Reynolds number Re_x at laminar conditions from Quintanilha et al. [15].

6.3 Summary of Transient Growth

In this chapter, transient growth analysis was applied to two-dimensional flows, the steady solutions (base flows) of which were obtained using an unstructured finite volume industrial solver. This was achieved by solving the initial value problem (IVP) and performing a Singular Value Decomposition of the Jacobian matrix exponential resulting from the discretization of the eigenvalue problem. The matrix exponential was formed by using a subset of the total eigenmodes, since the resulting linear operators

are large and sparse. The size of the subspace used is considerably larger than that used for modal analysis. The first case studied used for validation was that of a cylinder flow at low compressibility conditions for a Mach number of 0.2. When compared to the available literature results for incompressible flow, it was observed that the higher Mach number resulted in lower values of $G(t)$ achieved at larger times, while a good agreement was observed for the optimal transient modes. This is due to the stabilisation effects of compressibility as seen in DNS studies examining the effect of increasing Mach number on the same geometry [12]. Ultimately, this study aimed to investigate the amplification of optimal disturbances for a supercritical airfoil at steady turbulent conditions around shock buffet onset at a Mach number of 0.73 and a Reynolds number of 3.2×10^6 for a range of angles of attack. For this test case, self-sustained oscillations occur for angles of attack higher than and including $\alpha = 3.5°$. The angles of attack studied herein ranged from pre-onset conditions at $\alpha = 2.75°$ to post-onset at $\alpha = 4.0°$. In all cases, the initial optimal growth was followed by exponential eigenmodal decay for subcritical angles of attack and growth for angles of attack post-onset, respectively. The maximum energy gain found for the highest subcritical angle of attack $\alpha = 3.35°$ was $G_{max} = 107.1$. Lastly, a scrutiny of the dependence of G_{max} on angle of attack for the subcritical cases revealed that there is a quartic dependence $G_{max} \sim \alpha^4$, similar to the quartic dependence of maximum gain on the local Reynolds number $G_{max} \sim {Re_x}^4$ observed for hypersonic laminar flow [15].

Chapter 7

Conclusions and Future Work

A study aiming to further advance the understanding of the mechanisms governing transonic shock-buffet using linearised and non-linear Reynolds-averaged Navier–Stokes based methods has been presented herein. The shock-buffet phenomenon is an unsteady shock-wave/boundary-layer interaction characterised by self-excited, self-sustained periodic oscillations which demonstrate a broadband frequency signature for swept-wings and a distinct frequency for aerofoils. The phenomenon is of industrial relevance, since these oscillations, apart from the degradation of passenger comfort, fuel consumption and handling qualities, pose the risk of structural failure when they excite the inherently elastic wings of the aircraft. This is reflected in the restrictions posed on manufacturers by regulatory authorities to ensure that these airframe vibrations (buffeting) due to shock-buffet will not occur within the design flight envelope of each aircraft.

Although a plethora of research has focused on aerofoil and infinite wing shock-buffet, the literature dealing with finite swept-wings around onset conditions is quite limited, especially when it comes to the interaction of the phenomenon with wing vibration. Similarly, in the case of aerofoil shock-buffet, most stability studies in steady turbulent conditions focus on the onset of the global instability based on eigenvalue analysis or on optimal response to optimal forcing (resolvent) based on pseudospectrum analysis. This thesis has aimed to fill these gaps in the literature by investigating the interaction of transonic buffet with harmonic forcing and an elastic structure in the case of finite swept-wings and the short-time amplification of optimal disturbances in the case of aerofoils.

As a result, this project was divided into three key investigations:

1. **Chapter 4. Flow Response to Harmonic Forcing:** Harmonic forcing simulations at a range of frequencies were carried out for small excitation amplitudes

using linearised methods for the RBC12 and the NASA CRM around buffet onset which were then extended to time-accurate simulations with larger excitation amplitudes for the RBC12 geometry at pre and post-onset conditions

2. **Chapter 5. Fluid-Structure Interaction:** Unsteady RANS and fluid-structure interaction simulations were carried out for the NASA CRM at shock buffet conditions

3. **Chapter 6. Transient Growth:** Nonmodal stability analysis was carried out for the supercritical aerofoil OAT15A for incidences ranging from pre-onset to post-onset conditions

Firstly, the linearised part of the harmonic forcing study, focused on the response to small amplitude excitations at a range of frequencies of two large civil aircraft, namely the RBC12 and the NASA Common Research Model, the wings of which have been designed decades apart. The angles of attack examined, ranged from 2° to 3.01° for the RBC12, for which buffet onset occurs at approximately 3°, and from 3° to 3.6° for the NASA CRM, for which buffet onset occurs at approximately 3.5°. A linearised frequency-domain analysis for a range of frequencies showed a similar behaviour of the dynamic derivatives when excited with the same synthetic torsion mode. Specifically, an amplified response of the dynamic derivatives was found for excitation frequencies in the shock buffet range ($\omega^* = 3.1$ for the RBC12 and $\omega^* = 2.4$ for the NASA CRM) that got further amplified for small incidence increments. Furthermore, a low frequency resonant peak ($\omega^* = 0.8$ for the RBC12 and $\omega^* = 0.6$ for the NASA CRM) that was present even for pre-onset angles of attack, did not get further amplified as incidence was increased to onset conditions. The eigenvalue analysis of the fluid Jacobian hinted that the high frequency behaviour was linked to an absolute instability, something that was later confirmed in the work of Timme [95], in contrast to the low frequency behaviour which has been observed experimentally as inboard propagating waves along the shock front [96] but its source remains elusive. Spatially, the high frequency behaviour revealed localised unsteadiness starting at the most outboard region of the separated area while the low frequency behaviour was mostly energetic along the shock front. The same synthetic mode was used on the RBC12 geometry for the second part of the harmonic forcing study, which involved time-accurate simulations that allowed larger excitation amplitudes. The frequency content of the response for each combination of excitation frequency and forcing amplitude factor was recovered using a discrete Fourier transform. Different combinations of frequencies and excitation amplitude factors were examined at pre-onset and post-onset conditions. The pre-onset simulations that were used for validation showed that while the primary frequency response was at that of the excitation, lower amplitude response around the frequency of the resonant peak was present for all excitation frequencies, regardless of their proximity to

the shock buffet frequency range. Two different behaviours were found at shock buffet conditions. For small amplitude factors ($q_0 \leq 0.001$) the effect of forcing was negligible as the response followed that of shock buffet something that was also evident in the frequency content, demonstrating a broadband response around the shock-buffet frequency range. As the amplitude factor was increased ($q_0 > 0.001$) the flow response synchronised with that of the excitation. At these conditions, instantaneous plots of the friction coefficient showed that the increase in the excitation amplitude factor results in the outboard running separated areas to grow in size. A closer look of the frequency content revealed that only the high frequency response, associated with the absolute instability, was shifted to the excitation frequency while the lower frequency response was unaffected. This result shows that the three-dimensional effects present in swept-wing shock-buffet prohibit a complete synchronisation (or "lock-in") of the phenomenon response to the excitation, something observed for aerofoils. The immediate next step in the work related to harmonic forcing would be the use of different excitation modes as well as the excitation of the flow at the frequency of the resonant peak observed in the LFD results but in time-accurate simulations.

The effect of the interaction of shock buffet with an elastic wing structure, was investigated by carrying out a fluid-structure (FSI) interaction simulation alongside a URANS simulation for the NASA CRM. The flow conditions were similar to these used in the harmonic forcing study although a higher supercritical angle of attack $\alpha = 3.75^\circ$ was used.The time-averaged pressure distributions were similar for both simulations and agreed nicely with the available wind tunnel data. Good agreement with experimental data was also seen for wing deformation from the coupled simulation. Additionally, both simulations were able to accurately capture the outboard running buffet cells as well as the shock front movement associated with the high frequency behaviour of shock buffet. A scrutiny of the lift coefficient frequency content, showed that the response was at the shock buffet frequency range for both simulations, albeit with a lower amplitude in the case of the coupled simulation. The resulting signal of the modal amplitude displayed two behaviours, a linear and a nonlinear, respectively. In the linear part, the response of all modes was at the shock buffet frequency range around $St = 0.38$ ($\omega^* = 2.4$), with an exception of the lower frequency modes where a response at their respective natural frequencies was present. Conversely, in the nonlinear part of the response, modes whose natural frequency was lower than that of the shock buffet range revealed an additional frequency peak at their wind-off frequency. Finally, modes with natural frequencies close to the shock buffet range demonstrated a singular peak at that respective frequency. A peak at the natural frequency of the first bending mode was evident for all modes in the nonlinear part. This shows that the shock-buffet instability dominates the structural response in the linear regime, although in the nonlinear part it mainly affects higher modes with natural frequencies in the shock-

buffet range. The response of lower frequency modes in the nonlinear part depends on their respective wind-off frequencies and the first bending mode frequency. Lastly, no frequency content was found in the range of the resonant peak, observed in the results of the LFD study for the same geometry, suggesting that the low frequency behaviour of the phenomenon is not linked to aeroelastic coupling. Future work would primarily involve a longer simulation. Secondly, the employment of passive control devices such as vortex generators would provide useful insight for the efficacy of shock-buffet control in a coupled aeroelastic setting.

Finally, modal and nonmodal stability analysis results were presented for the supercritical aerofoil OAT15A at steady turbulent conditions. Shock-buffet onset for this geometry occurs for angles of attack higher than and including $\alpha = 3.5°$. The incidences studied ranged from subcritical $\alpha = 2.75°$ to supercritical $\alpha = 4°$. The initial energy gain at short times is followed by the exponential growth or decay, according to the corresponding leading eigenmode from the modal analysis. Spatially, the optimal transient modes were most energetic in the same region as the global adjoint mode for the initial optimal growth modes and the global leading mode for optimal response modes. By further scrutinising the gain response for additional subcritical angles of attack, a quartic dependence of the maximum gain on the angle of attack was found. The next step would firstly aim to perform Floquet analysis in the time-periodic unstable flow at post-onset conditions. Secondly, nonmodal stability analysis would be extended to unswept infinite wings of different aspect ratios and ultimately to infinite swept wings to assess how three-dimensional effects influence transient growth of transonic buffet.

Bibliography

[1] Konz, C., Happel, C. C., Turano, D., Daniel, G., Bigger, M., Design), O. R. C., and Leishman, J. G., "Level-Flight Performance Envelopes," `https://eaglepubs.erau.edu/introductiontoaerospaceflightvehicles/chapter/performance-envelopes/`, Jan 2023.

[2] Abbas-Bayoumi, A. and Becker, K., "An industrial view on numerical simulation for aircraft aerodynamic design," *Journal of Mathematics in Industry*, Vol. 1, No. 1, 2011, pp. 1–14.

[3] Pearcey, H., Osborne, J., and Haines, A., "The interaction between local effects at the shock and rear separation-a source of significant scale effects in wind-tunnel tests on aerofoils and wings," Tech. Rep. AGARD CP-35, National Physics Laboratory, 1968.

[4] Masini, L., *On Transonic Wing Shock Unsteadiness*, Ph.D. thesis, University of Liverpool, 2021.

[5] Lee, B., "Oscillatory shock motion caused by transonic shock boundary-layer interaction," *AIAA journal*, Vol. 28, No. 5, 1990, pp. 942–944.

[6] Sartor, F. and Timme, S., "Delayed detached–eddy simulation of shock buffet on half wing–body configuration," *AIAA Journal*, Vol. 55, No. 4, 2017, pp. 1230–1240.

[7] Schmid, P. J. and Brandt, L., "Analysis of fluid systems: Stability, receptivity, sensitivitylecture notes from the flow-nordita summer school on advanced instability methods for complex flows, stockholm, sweden, 2013," *Applied Mechanics Reviews*, Vol. 66, No. 2, 2014.

[8] Keye, S. and Gammon, M. R., "Development of Deformed Computer-Aided Design Geometries for the Sixth Drag Prediction Workshop," *Journal of Aircraft*, Vol. 55, No. 4, 2018, pp. 1401–1405.

[9] Houtman, J. and Timme, S., "Towards Global Stability Analysis of Flexible Aircraft in Edge-of-the-Envelope Flow," *AIAA SciTech 2021 Forum*, 2021, AIAA 2021-xxxx.

[10] Reddy, S. C. and Henningson, D. S., "Energy growth in viscous channel flows," *Journal of Fluid Mechanics*, Vol. 252, 1993, pp. 209–238.

[11] Crouch, J., Garbaruk, A., and Magidov, D., "Predicting the onset of flow unsteadiness based on global instability," *Journal of Computational Physics*, Vol. 224, No. 2, 2007, pp. 924–940.

[12] Canuto, D. and Taira, K., "Two-dimensional compressible viscous flow around a circular cylinder," *Journal of fluid mechanics*, Vol. 785, 2015, pp. 349–371.

[13] Abdessemed, N., Sharma, A. S., Sherwin, S., and Theofilis, V., "Transient growth analysis of the flow past a circular cylinder," *Physics of Fluids*, Vol. 21, No. 4, 2009, pp. 044103.

[14] Sartor, F., Mettot, C., and Sipp, D., "Stability, receptivity, and sensitivity analyses of buffeting transonic flow over a profile," *AIAA Journal*, Vol. 53, No. 7, 2015, pp. 1980–1993.

[15] Quintanilha, H., Paredes, P., Hanifi, A., and Theofilis, V., "Transient growth analysis of hypersonic flow over an elliptic cone," *Journal of Fluid Mechanics*, Vol. 935, 2022.

[16] Seen, W. M., Gobithaasan, R., and Miura, K. T., "GPU acceleration of Runge Kutta-Fehlberg and its comparison with Dormand-Prince method," *AIP Conference Proceedings*, Vol. 1605, American Institute of Physics, 2014, pp. 16–21.

[17] Gudmundsson, S., *General aviation aircraft design: Applied Methods and Procedures*, Butterworth-Heinemann, 2013.

[18] Sandham, N., "Shock-wave/boundary-layer interactions," *NATO Research and Technology Organization (RTO)–Educational Notes Paper, RTO-EN-AVT-195*, Vol. 5, 2011, pp. 1–18.

[19] Dolling, D. S., "Fifty years of shock-wave/boundary-layer interaction research: what next?" *AIAA journal*, Vol. 39, No. 8, 2001, pp. 1517–1531.

[20] Babinsky, H. and Harvey, J. K., *Shock wave-boundary-layer interactions*, Vol. 32, Cambridge University Press, 2011.

[21] EASA, "Certification Specifications for Large Aeroplanes CS25," February 2009.

[22] Giannelis, N. F., Vio, G. A., and Levinski, O., "A Review of Recent Developments in the Understanding of Transonic Shock Buffet," *Progress in Aerospace Sciences*, Vol. 92, 2017, pp. 39–84.

[23] Hilton, W. F. and Fowler, R., "Photographs of shock wave movement," Reports and Memoranda 2692, National Aeronautical Establishment, 1947.

[24] McDevitt, J. B., "Supercritical flow about a thick circular-arc airfoil," NASA Technical Memorandum 78549, NASA, 1979.

[25] Mabey, D., "Oscillatory flows from shock induced separations on biconvex aerofoils of varying thickness in ventilated wind tunnels," Tech. Rep. AGARD CP-296, NATO, 1981.

[26] Mabey, D., Welsh, B., and Cripps, B., "Periodic flows on a rigid 14 % thick biconvex wing at transonic speeds," Technical Report 81059, Royal Aircraft Establishment, 1981.

[27] Gibb, J., *The cause and cure of periodic flows at transonic speeds*, Ph.D. thesis, Cranfield Institute of Technology, 1990.

[28] Tijdeman, H., "Investigations of the transonic flow around oscillating airfoils," *NLR-TR 77090 U*, 1977.

[29] Pearcey, H., "Some effects of shock-induced separation of turbulent boundary layers in transonic flow past aerofoils," Tech. Rep. ARC R & M-3108, Aeronautical Research Council, 1955.

[30] Pearcey, H., "A method for the prediction of the onset of buffeting and other separation effects from wind tunnel tests on rigid models," Tech. Rep. AGARD TR 223, National Physics Laboratory, 1958.

[31] Pearcey, H. and Holder, D., "Simple methods for the prediction of wing buffeting resulting from bubble type separation," Tech. Rep. NPL AERO-REP-1024, National Physics Laboratory, 1962.

[32] Roos, F. W., "Some features of the unsteady pressure field in transonic airfoil buffeting," *Journal of Aircraft*, Vol. 17, No. 11, 1980, pp. 781–788.

[33] Lee, B. H. and Ohman, L., "Unsteady pressures and forces during transonic buffeting of a supercritical airfoil," *Journal of aircraft*, Vol. 21, No. 6, 1984, pp. 439–441.

[34] Lee, B., Ellis, F., and Bureau, J., "Investigation of the buffet characteristics of two supercritical airfoils," *Journal of aircraft*, Vol. 26, No. 8, 1989, pp. 731–736.

[35] Feldhusen-Hoffmann, A., Statnikov, V., Klaas, M., and Schröder, W., "Investigation of shock–acoustic-wave interaction in transonic flow," *Experiments in Fluids*, Vol. 59, No. 1, 2018, pp. 1–13.

[36] Hartmann, A., Klaas, M., and Schröder, W., "Time-resolved stereo PIV measurements of shock–boundary layer interaction on a supercritical airfoil," *Experiments in fluids*, Vol. 52, No. 3, 2012, pp. 591–604.

[37] Hartmann, A., Klaas, M., and Schröder, W., "Coupled airfoil heave/pitch oscillations at buffet flow," *AIAA journal*, Vol. 51, No. 7, 2013, pp. 1542–1552.

[38] Jacquin, L., Molton, P., Deck, S., Maury, B., and Soulevant, D., "Experimental study of shock oscillation over a transonic supercritical profile," *AIAA journal*, Vol. 47, No. 9, 2009, pp. 1985–1994.

[39] Hartmann, A., Feldhusen, A., and Schröder, W., "On the interaction of shock waves and sound waves in transonic buffet flow," *Physics of Fluids*, Vol. 25, No. 2, 2013, pp. 026101.

[40] Deck, S., "Recent improvements in the zonal detached eddy simulation (ZDES) formulation," *Theoretical and Computational Fluid Dynamics*, Vol. 26, No. 6, 2012, pp. 523–550.

[41] Xiao, Q., Tsai, H.-M., and Liu, F., "Numerical study of transonic buffet on a supercritical airfoil," *AIAA journal*, Vol. 44, No. 3, 2006, pp. 620–628.

[42] Garnier, E. and Deck, S., "Large-eddy simulation of transonic buffet over a supercritical airfoil," *Turbulence and interactions*, Springer, 2010, pp. 135–141.

[43] Crouch, J., Garbaruk, A., Magidov, D., and Travin, A., "Origin of transonic buffet on aerofoils," *Journal of fluid mechanics*, Vol. 628, 2009, pp. 357–369.

[44] Crouch, J., Garbaruk, A., Magidov, D., and Jacquin, L., "Global structure of buffeting flow on transonic airfoils," *IUTAM symposium on unsteady separated flows and their control*, Springer, 2009, pp. 297–306.

[45] McDevitt, J. B. and Okuno, A. F., "Static and dynamic pressure measurements on a NACA 0012 airfoil in the Ames high Reynolds number facility," Technical Paper 2485, NASA, 1985.

[46] Levy Jr, L. L., "Experimental and computational steady and unsteady transonic flows about a thick airfoil," *AIAA Journal*, Vol. 16, No. 6, 1978, pp. 564–572.

[47] Edwards, J. and Thomas, J., "Computational methods for unsteady transonic flows," Technical Memorandum 89106, NASA, 1987.

[48] Maksymiuk, C. and Pulliam, T., "Viscous transonic airfoil workshop results using ARC2D," 25th AIAA Aerospace Sciences Meeting, AIAA, 1987.

[49] Brunet, V., "Computational study of buffet phenomenon with unsteady RANS equations," 21st AIAA Applied Aerodynamics Conference, AIAA, 2003, p. 3679.

[50] Iovnovich, M. and Raveh, D. E., "Reynolds-averaged Navier-Stokes study of the shock-buffet instability mechanism," *AIAA journal*, Vol. 50, No. 4, 2012, pp. 880–890.

[51] Goncalves, E. and Houdeville, R., "Turbulence model and numerical scheme assessment for buffet computations," *International Journal for Numerical Methods in Fluids*, Vol. 46, No. 11, 2004, pp. 1127–1152.

[52] Barakos, G. and Drikakis, D., "Numerical simulation of transonic buffet flows using various turbulence closures," *International Journal of Heat and Fluid Flow*, Vol. 21, No. 5, 2000, pp. 620–626.

[53] Rouzaud, O., Plot, S., and Couaillier, V., "Numerical simulation of buffeting over airfoil using dual time stepping method," *Office National D' Etudes et De Recherches Aerospatiales ONERA-Publications-TP*, , No. 231, 2000.

[54] Rumsey, C. L., Sanetrik, M. D., Biedron, R. T., Melson, N. D., and Parlette, E. B., "Efficiency and accuracy of time-accurate turbulent Navier-Stokes computations," *Computers & Fluids*, Vol. 25, No. 2, 1996, pp. 217–236.

[55] Deck, S., "Numerical simulation of transonic buffet over a supercritical airfoil," *AIAA journal*, Vol. 43, No. 7, 2005, pp. 1556–1566.

[56] Grossi, F., Braza, M., and Hoarau, Y., "Prediction of transonic buffet by delayed detached-eddy simulation," *AIAA Journal*, Vol. 52, No. 10, 2014, pp. 2300–2312.

[57] Fukushima, Y. and Kawai, S., "Wall-modeled large-eddy simulation of transonic airfoil buffet at high Reynolds number," *AIAA journal*, Vol. 56, No. 6, 2018, pp. 2372–2388.

[58] Zauner, M., De Tullio, N., and Sandham, N. D., "Direct numerical simulations of transonic flow around an airfoil at moderate Reynolds numbers," *AIAA Journal*, Vol. 57, No. 2, 2019, pp. 597–607.

[59] Brion, V., Dandois, J., Abart, J.-C., and Paillart, P., "Experimental analysis of the shock dynamics on a transonic laminar airfoil," *Progress in Flight Physics–Volume 9*, Vol. 9, 2017, pp. 365–386.

[60] Dandois, J., Mary, I., and Brion, V., "Large-eddy simulation of laminar transonic buffet," *Journal of Fluid Mechanics*, Vol. 850, 2018, pp. 156–178.

[61] Blevins, R., *Flow-induced Vibration*, Van Nostrand Reinhold, 1990.

[62] Govardhan, R. and Williamson, C., "Resonance forever: existence of a critical mass and an infinite regime of resonance in vortex-induced vibration," *Journal of Fluid Mechanics*, Vol. 473, 2002, pp. 147–166.

[63] Raveh, D. and Dowell, E., "Frequency lock-in phenomenon for oscillating airfoils in buffeting flows," *Journal of Fluids and Structures*, Vol. 27, No. 1, 2011, pp. 89–104.

[64] Raveh, D. E. and Dowell, E. H., "Aeroelastic responses of elastically suspended airfoil systems in transonic buffeting flows," *AIAA journal*, Vol. 52, No. 5, 2014, pp. 926–934.

[65] Quan, J., Zhang, W., Gao, C., and Ye, Z., "Characteristic analysis of lock-in for an elastically suspended airfoil in transonic buffet flow," *Chinese Journal of Aeronautics*, Vol. 29, No. 1, 2016, pp. 129–143.

[66] Steimle, P. C., Karhoff, D.-C., and Schröder, W., "Unsteady transonic flow over a transport-type swept wing," *AIAA journal*, Vol. 50, No. 2, 2012, pp. 399–415.

[67] Jones, D., Roberts, I., and Gaitonde, A., "Identification of limit cycles for piecewise nonlinear aeroelastic systems," *Journal of Fluids and Structures*, Vol. 23, No. 7, 2007, pp. 1012–1028.

[68] Gao, C., Zhang, W., Li, X., Liu, Y., Quan, J., Ye, Z., and Jiang, Y., "Mechanism of frequency lock-in in transonic buffeting flow," *Journal of Fluid Mechanics*, Vol. 818, 2017, pp. 528–561.

[69] Nitzsche, J., Ringel, L. M., Kaiser, C., and Hennings, H., "Fluid-Mode Flutter in Plane Transonic Flows," No. 6 in International Forum on Aeroelasticity and Structural Dynamics, IFASD, 2019.

[70] Hwang, C. and Pi, W., "Northrop F-5A aircraft transonic buffet pressure data acquisition and response analysis," *Journal of Aircraft*, Vol. 12, No. 9, 1975, pp. 714–720.

[71] Riddle, D., "Wind-tunnel investigation of surface-pressure fluctuations associated with aircraft buffet," *13th Aerospace Sciences Meeting*, 1975, p. 67.

[72] Roos, F., "The buffeting pressure field of a high-aspect-ratio swept wing," *18th Fluid Dynamics and Plasmadynamics and Lasers Conference*, 1985, p. 1609.

[73] Benoit, B. and Legrain, I., "Buffeting prediction for transport aircraft applications based on unsteady pressure measurements," *5th Applied Aerodynamics Conference*, 1987, p. 2356.

[74] Dandois, J., "Experimental study of transonic buffet phenomenon on a 3D swept wing," *Physics of Fluids*, Vol. 28, No. 1, 2016, pp. 016101.

[75] Koike, S., Ueno, M., Nakakita, K., and Hashimoto, A., "Unsteady pressure measurement of transonic buffet on NASA common research model," *34th AIAA Applied Aerodynamics Conference*, 2016, p. 4044.

[76] Merienne, M.-C., Le Sant, Y., Lebrun, F., Deleglise, B., and Sonnet, D., "Transonic buffeting investigation using unsteady pressure-sensitive paint in a large wind tunnel," *51st AIAA Aerospace Sciences Meeting including the New Horizons Forum and Aerospace Exposition*, 2013, p. 1136.

[77] Lawson, S., Greenwell, D., and Quinn, M. K., "Characterisation of buffet on a civil aircraft wing," 54th AIAA Aerospace Sciences Meeting, AIAA, American Institute of Aeronautics and Astronautics, 2016, p. 1309.

[78] Sugioka, Y., Koike, S., Nakakita, K., Numata, D., Nonomura, T., and Asai, K., "Experimental analysis of transonic buffet on a 3D swept wing using fast-response pressure-sensitive paint," *Experiments in Fluids*, Vol. 59, No. 6, 2018, pp. 1–20.

[79] "An introduction to aircraft buffet and buffeting," Tech. Rep. 87012, Engineering Sciences Data Unit, 1987.

[80] Paladini, E., Dandois, J., Sipp, D., and Robinet, J.-C., "Analysis and comparison of transonic buffet phenomenon over several three-dimensional wings," *AIAA Journal*, Vol. 57, No. 1, 2019, pp. 379–396.

[81] Brunet, V. and Deck, S., "Zonal-detached eddy simulation of transonic buffet on a civil aircraft type configuration," *Advances in Hybrid RANS-LES Modelling*, Springer, 2008, pp. 182–191.

[82] Caruana, D., Mignosi, A., Corrège, M., Le Pourhiet, A., and Rodde, A., "Buffet and buffeting control in transonic flow," *Aerospace Science and Technology*, Vol. 9, No. 7, 2005, pp. 605–616.

[83] Ishida, T., Hashimoto, A., Ohmichi, Y., Aoyama, T., and Takekawa, K., "Transonic Buffet Simulation over NASA-CRM by Unsteady-FaSTAR Code," 55th AIAA Aerospace Sciences Meeting, AIAA.

[84] Sartor, F. and Timme, S., "Reynolds-averaged Navier-Stokes simulations of shock buffet on half wing-body configuration," 53rd AIAA Aerospace Sciences Meeting, AIAA, 2015, p. 1939.

[85] Sartor, F. and Timme, S., "Mach number effects on buffeting flow on a half wing-body configuration," *International Journal of Numerical Methods for Heat & Fluid Flow*, 2016.

[86] Iovnovich, M. and Raveh, D. E., "Numerical study of shock buffet on three-dimensional wings," *AIAA Journal*, Vol. 53, No. 2, 2015, pp. 449–463.

[87] Plante, F., Dandois, J., and Laurendeau, É., "Similarities between cellular patterns occurring in transonic buffet and subsonic stall," *AIAA Journal*, Vol. 58, No. 1, 2020, pp. 71–84.

[88] Theofilis, V., "Global linear instability," *Annual Review of Fluid Mechanics*, Vol. 43, 2011, pp. 319–352.

[89] Crouch, J., Garbaruk, A., and Strelets, M., "Global instability in the onset of transonic-wing buffet," *Journal of Fluid Mechanics*, Vol. 881, 2019, pp. 3–22.

[90] Paladini, E., Beneddine, S., Dandois, J., Sipp, D., and Robinet, J.-C., "Transonic buffet instability: From two-dimensional airfoils to three-dimensional swept wings," *Physical Review Fluids*, Vol. 4, No. 10, 2019, pp. 103906.

[91] Plante, F. and Laurendeau, É., "Simulation of transonic buffet using a time-spectral method," *AIAA Journal*, Vol. 57, No. 3, 2019, pp. 1275–1287.

[92] He, W. and Timme, S., "Triglobal shock buffet instability study on infinite wings," AIAA Scitech 2020 Forum, AIAA, 2020, p. 1986.

[93] He, W. and Timme, S., "Resolvent Analysis of Shock Buffet on Infinite Wings," AIAA Aviation 2020 Forum, AIAA, 2020, p. 2727.

[94] Timme, S. and Thormann, R., "Towards three-dimensional global stability analysis of transonic shock buffet," AIAA Atmospheric Flight Mechanics Conference, AIAA, 2016, p. 3848.

[95] Timme, S., "Global instability of wing shock-buffet onset," *Journal of Fluid Mechanics*, Vol. 885, 2020, pp. A37.

[96] Masini, L., Timme, S., and Peace, A., "Analysis of a civil aircraft wing transonic shock buffet experiment," *Journal of Fluid Mechanics*, Vol. 884, 2020.

[97] Masini, L., Timme, S., and Peace, A. J., "Scale-resolving simulations of a civil aircraft wing transonic shock-buffet experiment," *AIAA Journal*, Vol. 58, No. 10, 2020, pp. 4322–4338.

[98] Ohmichi, Y., Ishida, T., and Hashimoto, A., "Modal decomposition analysis of three-dimensional transonic buffet phenomenon on a swept wing," *AIAA Journal*, Vol. 56, No. 10, 2018, pp. 3938–3950.

[99] Houtman, J., Timme, S., and Sharma, A., "Resolvent Analysis of Large Aircraft Wings in Edge-of-the-Envelope Transonic Flow," AIAA SCITECH 2022 Forum, AIAA, 2022, p. 1329.

[100] Sartor, F., Mettot, C., Bur, R., and Sipp, D., "Unsteadiness in transonic shock-wave/boundary-layer interactions: experimental investigation and global stability analysis," *Journal of Fluid Mechanics*, Vol. 781, 2015, pp. 550–577.

[101] Stokes, G., "On the Theories of Internal Friction of Fluids in Motion, Translated by Cambridge Phil," *Soc., UK*, Vol. 8, 1845, pp. 287–305.

[102] Blazek, J., *Computational fluid dynamics: principles and applications*, Butterworth-Heinemann, 2015.

[103] Reynolds, O., "On the dynamical theory of incompressible viscous fluids and the determination of the criterion, Cambridge Phil," *Trans*, 1895, pp. 123–164.

[104] Wilcox, D. C. et al., *Turbulence modeling for CFD*, Vol. 2, DCW industries La Canada, CA, 1998.

[105] Boussinesq, J. V., "Essai sur la théorie des eaux courantes," Mémoires Tome XXIII, 1, Institut National de France, 1877.

[106] Spalart, P. and Allmaras, S., "A One-Equation Turbulence Model for Aerodynamic Flows," *AIAA*, Vol. 439, 01 1992.

[107] Kalitzin, G., Medic, G., Iaccarino, G., and Durbin, P., "Near-wall behavior of RANS turbulence models and implications for wall functions," *Journal of Computational Physics*, Vol. 204, No. 1, 2005, pp. 265–291.

[108] Allmaras, S. R. and Johnson, F. T., "Modifications and Clarifications for the Implementation of the Spalart-Allmaras Turbulence Model," Vol. 1902 of *Seventh International Conference on Computational Fluid Dynamics (ICCFD7)*, 2012.

[109] Shur, M., Strelets, M., Zajkov, L., Gulyaev, A., Kozlov, V., and Sekundov, A., *Comparative numerical testing of one- and two-equation turbulence models for flows with separation and reattachment*.

[110] Thormann, R. and Widhalm, M., "Linear-frequency-domain predictions of dynamic-response data for viscous transonic flows," *AIAA journal*, Vol. 51, No. 11, 2013, pp. 2540–2557.

[111] Dwight, R., Brezillon, J., and Vollmer, D., "Efficient algorithms for solution of the adjoint compressible Navier-Stokes equations with applications," *ODAS 2006*, 2006.

[112] Arnoldi, W. E., "The principle of minimized iterations in the solution of the matrix eigenvalue problem," *Quarterly of applied mathematics*, Vol. 9, No. 1, 1951, pp. 17–29.

[113] Sorensen, D. C., "Implicitly restarted Arnoldi/Lanczos methods for large scale eigenvalue calculations," *Parallel Numerical Algorithms*, Springer, 1997, pp. 119–165.

[114] Saad, Y., *Iterative methods for sparse linear systems*, SIAM, 2003.

[115] Moler, C. and Van Loan, C., "Nineteen dubious ways to compute the exponential of a matrix," *SIAM review*, Vol. 20, No. 4, 1978, pp. 801–836.

[116] Moler, C. and Van Loan, C., "Nineteen dubious ways to compute the exponential of a matrix, twenty-five years later," *SIAM review*, Vol. 45, No. 1, 2003, pp. 3–49.

[117] Farrell, B. F. and Ioannou, P. J., "Generalized stability theory. Part I: Autonomous operators," *Journal of Atmospheric Sciences*, Vol. 53, No. 14, 1996, pp. 2025–2040.

[118] Schmid, P. J., "Nonmodal stability theory," *Annu. Rev. Fluid Mech.*, Vol. 39, 2007, pp. 129–162.

[119] Hanifi, A., Schmid, P. J., and Henningson, D. S., "Transient growth in compressible boundary layer flow," *Physics of Fluids*, Vol. 8, No. 3, 1996, pp. 826–837.

[120] Mack, L., "Boundary-layer stability theory. JPL Report 900-277 Rev. A," *Jet Propulsion Laboratory, Pasadena, USA*, 1969.

[121] Chu, B.-T., "On the energy transfer to small disturbances in fluid flow (Part I)," *Acta Mechanica*, Vol. 1, No. 3, 1965, pp. 215–234.

[122] Paredes, P., Gosse, R., Theofilis, V., and Kimmel, R., "Linear modal instabilities of hypersonic flow over an elliptic cone," *Journal of Fluid Mechanics*, Vol. 804, 2016, pp. 442–466.

[123] Trefethen, L. N., "Spectra and pseudospectra," *The Graduate Student's Guide to Numerical Analysis' 98*, Springer, 1999, pp. 217–250.

[124] Schmid, P. J. and Henningson, D. S., *Stability and Transition in Shear Flows*, Springer New York, 2001.

[125] Taira, K., Brunton, S. L., Dawson, S. T., Rowley, C. W., Colonius, T., McKeon, B. J., Schmidt, O. T., Gordeyev, S., Theofilis, V., and Ukeiley, L. S., "Modal analysis of fluid flows: An overview," *Aiaa Journal*, Vol. 55, No. 12, 2017, pp. 4013–4041.

[126] Barkley, D., Blackburn, H. M., and Sherwin, S. J., "Direct optimal growth analysis for timesteppers," *International journal for numerical methods in fluids*, Vol. 57, No. 9, 2008, pp. 1435–1458.

[127] Monokrousos, A., Åkervik, E., Brandt, L., and Henningson, D. S., "Global three-dimensional optimal disturbances in the Blasius boundary-layer flow using time-steppers," *Journal of Fluid Mechanics*, Vol. 650, 2010, pp. 181–214.

[128] Sipp, D., Marquet, O., Meliga, P., and Barbagallo, A., "Dynamics and control of global instabilities in open-flows: a linearized approach," *Applied Mechanics Reviews*, Vol. 63, No. 3, 2010.

[129] Cullen, C. G., *Matrices and linear transformations*, Courier Corporation, 2012.

[130] Schwamborn, D., Gerhold, T., and Heinrich, R., "The DLR TAU-code: recent applications in research and industry," ECCOMAS CFD 2006 CONFERENCE, ECCOMAS, 2006.

[131] Gerhold, T. and Neumann, J., "The parallel mesh deformation of the DLR TAU-code," *New results in numerical and experimental fluid mechanics VI*, Springer, 2007, pp. 162–169.

[132] Neumann, J. and Mai, H., "Gust response: Simulation of an aeroelastic experiment by a fluid–structure interaction method," *Journal of Fluids and Structures*, Vol. 38, 2013, pp. 290–302.

[133] Spalart, P., "Trends in Turbulence Treatments," Fluids 2000 Conference and Exhibit, AIAA, 2000, p. 2306.

[134] He, W. and Timme, S., "Triglobal infinite-wing shock-buffet study," *Journal of Fluid Mechanics*, Vol. 925, 2021, pp. A27.

[135] Dwight, R., "An implicit LU-SGS scheme for finite-volume discretizations of the Navier-Stokes equations on hybrid grids," Tech. Rep. FB-2005-05, DLR, 2006.

[136] Xu, S., Timme, S., and Badcock, K. J., "Enabling off-design linearised aerodynamics analysis using Krylov subspace recycling technique," *Computers & Fluids*, Vol. 140, 2016, pp. 385–396.

[137] Thormann, R. and Timme, S., "Efficient aerodynamic derivative calculation in three-dimensional transonic flow," *The Aeronautical Journal*, Vol. 121, No. 1244, 2017, pp. 1464–1478.

[138] DLR, "FlowSimulator DataManager (FSDM)," `https://www.dlr.de/sc/en/desktopdefault.aspx/tabid-12766/22301_read-51273/`.

[139] Meinel, M. and Einarsson, G. O., "The FlowSimulator framework for massively parallel CFD applications," PARA 2010: Conference on state of the Art in Scientific and Parallel Computing, Springer, 2010.

[140] Ritter, M., "Static and forced motion aeroelastic simulations of the HIRENASD wind tunnel model," *53rd AIAA/ASME/ASCE/AHS/ASC Structures, Structural Dynamics and Materials Conference 20th AIAA/ASME/AHS Adaptive Structures Conference 14th AIAA*, 2012, p. 1633.

[141] NASA, "NASA Common Research Model: FEM files," `https://commonresearchmodel.larc.nasa.gov/fem-file/`.

[142] Newmark, N. M., "A method of computation for structural dynamics," *Journal of the engineering mechanics division*, Vol. 85, No. 3, 1959, pp. 67–94.

[143] Harris, C. D., "NASA supercritical airfoils: A Matrix of Family-Related Airfoils," Technical Paper 2969, NASA, 1990.

[144] Anderson, J., *EBOOK: Fundamentals of Aerodynamics (SI units)*, McGraw Hill, 2011.

[145] Brunet, V., Deck, S., Molton, P., and Thiery, M., "A complete experimental and numerical study of the buffet phenomenon over the oat 15 a airfoil," *ONERA: Tire a Part*, Vol. 35, 2005, pp. 1–9.

[146] Dandois, J., Molton, P., Lepage, A., Geeraert, A., Brunet, V., Dor, J., and Coustols, E., "Buffet characterization and control for turbulent wings," *Aerospace Lab*, , No. 6, 2013, pp. p–1.

[147] Brunet, V., "Numerical investigation of buffet phenomenon with URANS equations," *ONERA: Tire a Part*, , No. 192, 2005, pp. 1.

[148] Masini, L., Timme, S., Ciarella, A., and Peace, A., "Influence of Vane Vortex Generators on Transonic Wing Buffet: Further Analysis of the BUCOLIC Experimental Dataset," No. FP14 in 52nd 3AF International Conference on Applied Aerodynamics, 3AF, 2017.

[149] Sartor, F. and Timme, S., "Delayed detached–eddy simulation of shock buffet on half wing–body configuration," *AIAA Journal*, Vol. 55, No. 4, 2016, pp. 1230–1240.

[150] Keye, S., Brodersen, O., and Rivers, M. B., "Investigation of aeroelastic effects on the NASA common research model," *Journal of Aircraft*, Vol. 51, No. 4, 2014, pp. 1323–1330.

[151] NASA, "NASA Common Research Model: Publications," `https://commonresearchmodel.larc.nasa.gov/publications/`.

[152] Vassberg, J., Dehaan, M., Rivers, M., and Wahls, R., "Development of a Common Research Model for Applied CFD Validation Studies," 26th AIAA applied aerodynamics conference, AIAA, 2008, p. 6919.

[153] Raveh, D. E., "Numerical study of an oscillating airfoil in transonic buffeting flows," *AIAA journal*, Vol. 47, No. 3, 2009, pp. 505–515.

[154] Giannelis, N. F. and Vio, G. A., "Investigation of Frequency Lock-In Phenomena on a Supercritical Aerofoil in the Presence of Transonic Shock Oscillations," No. 74 in International Forum on Aeroelasticity and Structural Dynamics, IFASD, 2017.

[155] Giannelis, N. and Vio, G., "A Modal Approach to Shock Buffet Lock-In Analysis," *Proceedings of 29th International Conference on Noise and Vibration Engineering, Leuven, Belgium*, 2020, pp. 247–260.

[156] Lehoucq, R. B., Sorensen, D. C., and Yang, C., *ARPACK users' guide: solution of large-scale eigenvalue problems with implicitly restarted Arnoldi methods*, SIAM, 1998.

[157] Maschhoff, K. J. and Sorensen, D. C., "P_ARPACK: An efficient portable large scale eigenvalue package for distributed memory parallel architectures," *Lecture Notes in Computer Science*, Vol. 1184, 1996, pp. 478–486.

[158] Nitzsche, J., "A Numerical Study on Aerodynamic Resonance in Transonic Separated Flow," No. 126 in International Forum on Aeroelasticity and Structural Dynamics, IFASD, 2009.

[159] Gagliardi, F. and Giannakoglou, K. C., "A two–step radial basis function-based CFD mesh displacement tool," *Advances in Engineering Software*, Vol. 128, 2019, pp. 86–97.

[160] Lissajous, J., "Mémoire stir l'étude optique des mouvements vibratoires," *Annales de Chimie et de Physique 3e*, Vol. 51, 1849, pp. 140–231.

[161] Maor, E., "Jules Lissajous and His Figures," *Trigonometric Delights*, 2020.

[162] Belesiotis-Kataras, P. and Timme, S., "Numerical Study of Incipient Transonic Shock Buffet on Large Civil Aircraft Wings," Applied Aerodynamics Conference, Royal Aeronautical Society, 2018.

[163] Tinoco, E. N., Brodersen, O. P., Keye, S., Laflin, K. R., Feltrop, E., Vassberg, J. C., Mani, M., Rider, B., Wahls, R. A., Morrison, J. H., Hue, D., Roy, C. J., Mavriplis, D. J., and Murayama, M., "Summary Data from the Sixth AIAA CFD Drag Prediction Workshop: CRM Cases," *Journal of Aircraft*, Vol. 55, No. 4, 2018, pp. 1352–1379.

[164] Huerre, P. and Rossi, M. J., *Hydrodynamic Instabilities in Open Flows*, Collection Alea-Saclay: Monographs and Texts in Statistical Physics, 1998, pp. 81–294.

[165] Reshotko, E., "Transient growth: a factor in bypass transition," *Physics of Fluids*, Vol. 13, No. 5, 2001, pp. 1067–1075.

[166] Tollmien, W., "Über die entstehung der turbulenz," *Vorträge aus dem Gebiete der Aerodynamik und verwandter Gebiete*, Springer, 1930, pp. 18–21.

[167] Schlichting, H., "Berechnung ebener periodischer Grenzschichtstromungen," *Phys. z.*, Vol. 33, 1932, pp. 327–335.

[168] Herbert, T., "Secondary instability of boundary layers," *Annual review of fluid mechanics*, Vol. 20, No. 1, 1988, pp. 487–526.

[169] Smith, A. and Gamberoni, N., *Transition, Pressure Gradient and Stability Theory*, ARC-19322, Douglas Aircraft Company, El Segundo Division, 1956.

[170] Van Ingen, J., "A suggested semi-empirical method for the calculation of the boundary layer transition region," *Technische Hogeschool Delft, Vliegtuigbouwkunde, Rapport VTH-74*, 1956.

[171] Spall, R. E. and Malik, M. R., "Linear stability theory and three-dimensional boundary layer transition," *NASA. Langley Research Center, First Annual High-Speed Research Workshop, Part 4*, 1992.

[172] Eppink, J. L., Wlezien, R. W., King, R. A., and Choudhari, M., "Interaction of a backward-facing step and crossflow instabilities in boundary-layer transition," *AIAA Journal*, Vol. 56, No. 2, 2018, pp. 497–509.

[173] Yim, E., Meliga, P., and Gallaire, F., "Self-consistent triple decomposition of the turbulent flow over a backward-facing step under finite amplitude harmonic forcing," *Proceedings of the Royal Society A*, Vol. 475, No. 2225, 2019, pp. 20190018.

[174] Hussain, A. K. M. F. and Reynolds, W. C., "The mechanics of an organized wave in turbulent shear flow," *Journal of Fluid mechanics*, Vol. 41, No. 2, 1970, pp. 241–258.

[175] Reynolds, W. and Hussain, A., "The mechanics of an organized wave in turbulent shear flow. Part 3. Theoretical models and comparisons with experiments," *Journal of Fluid Mechanics*, Vol. 54, No. 2, 1972, pp. 263–288.

[176] Del Alamo, J. C. and Jimenez, J., "Linear energy amplification in turbulent channels," *Journal of Fluid Mechanics*, Vol. 559, 2006, pp. 205–213.

[177] Orszag, S. A. and Kells, L. C., "Transition to turbulence in plane Poiseuille and plane Couette flow," *Journal of Fluid Mechanics*, Vol. 96, No. 1, 1980, pp. 159–205.

[178] Kao, T. W. and Park, C., "Experimental investigations of the stability of channel flows. Part 1. Flow of a single liquid in a rectangular channel," *Journal of Fluid Mechanics*, Vol. 43, No. 1, 1970, pp. 145–164.

[179] Davies, S. and White, C., "An experimental study of the flow of water in pipes of rectangular section," *Proceedings of the Royal Society of London. Series A, Containing Papers of a Mathematical and Physical Character*, Vol. 119, No. 781, 1928, pp. 92–107.

[180] Patel, V. and Head, M., "Some observations on skin friction and velocity profiles in fully developed pipe and channel flows," *Journal of Fluid Mechanics*, Vol. 38, No. 1, 1969, pp. 181–201.

[181] Golub, G. H. and Van Loan, C. F., *Matrix computations*, JHU press, 2013.

[182] Barkley, D. and Henderson, R. D., "Three-dimensional Floquet stability analysis of the wake of a circular cylinder," *Journal of Fluid Mechanics*, Vol. 322, 1996, pp. 215–241.

[183] Hammache, M. and Gharib, M., "An experimental study of the parallel and oblique vortex shedding from circular cylinders," *Journal of Fluid Mechanics*, Vol. 232, 1991, pp. 567–590.

[184] Hill, D., "A Theoretical Approach for Analyzing the Restabilization of Wakes," Technical Memorandum 103858, 1992.

[185] Giannetti, F. and Luchini, P., "Structural sensitivity of the first instability of the cylinder wake," *Journal of Fluid Mechanics*, Vol. 581, 2007, pp. 167–197.

[186] Marquet, O., Lombardi, M., Chomaz, J.-M., Sipp, D., and Jacquin, L., "Direct and adjoint global modes of a recirculation bubble: lift-up and convective non-normalities," *Journal of Fluid Mechanics*, Vol. 622, 2009, pp. 1–21.

[187] Sipp, D., "Open-loop control of cavity oscillations with harmonic forcings," *Journal of Fluid Mechanics*, Vol. 708, 2012, pp. 439–468.

[188] Lam, S. K., Pitrou, A., and Seibert, S., "Numba: A LLVM-Based Python JIT Compiler," *Proceedings of the Second Workshop on the LLVM Compiler Infrastructure in HPC*, Association for Computing Machinery, New York, NY, USA, 2015.

[189] NVIDIA Corporation Deep Learning Institute, "Fundamentals of Accelerated Computing with CUDA Python," Online Course.

[190] Fehlberg, E., "Classical fifth-, sixth-, seventh-, and eighth-order Runge-Kutta formulas with stepsize control," Tech. Rep. R-287, NASA, 1968.

[191] Fehlberg, E., "Some Experimental Results Concerning the Error Propagation in Runge-Kutta Type Integration Formulas," Tech. Rep. R-352, 1970.

[192] Daniel, J. W., Gragg, W. B., Kaufman, L., and Stewart, G. W., "Reorthogonalization and stable algorithms for updating the Gram-Schmidt QR factorization," *Mathematics of Computation*, Vol. 30, No. 136, 1976, pp. 772–795.

[193] Lezar, E. and Davidson, D., "GPU-based Arnoldi factorisation for accelerating finite element eigenanalysis," *2009 International Conference on Electromagnetics in Advanced Applications*, IEEE, 2009, pp. 380–383.

Appendix

Appendix A: Tensor Notation

Tensor notation (also referred to as index, indicial or Einstein notation) provides a convenient and compact notation to describe physical quantities in the governing equations when written in differential form [102]. The form of the tensor follows from its rank. Tensors of rank 0 have only one component and represent scalars. Expressions such as coordinate x_i or velocity components u_i in three dimensions are tensors of rank 1 (or first-order tensors) and have three components such as

$$\begin{aligned} x_i &= [x_1, x_2, x_3] = [x, y, z] = \mathbf{r} \\ u_i &= [u_1, u_2, u_3] = [u, v, w] = \mathbf{u} \end{aligned} \tag{1}$$

Tensors of rank 2 have nine components and correspond to 3×3 matrices e.g.,

$$u_i u_j \equiv \begin{bmatrix} u_1u_1 & u_1u_2 & u_1u_3 \\ u_2u_1 & u_2u_2 & u_2u_3 \\ u_3u_1 & u_3u_2 & u_3u_3 \end{bmatrix} \tag{2}$$

In a similar manner, the viscous stress tensor is

$$\tau_{ij} \equiv \begin{bmatrix} \tau_{11} & \tau_{12} & \tau_{13} \\ \tau_{12} & \tau_{22} & \tau_{23} \\ \tau_{12} & \tau_{32} & \tau_{33} \end{bmatrix} \tag{3}$$

A second-order tensor that provides important utility is the Kronecker delta. It is defines as

$$\delta_{ij} = \begin{cases} 1 & if i = j \\ 0 & if i \neq j \end{cases} \tag{4}$$

Finally, tensor notation uses the Einstein summation convention. This states that when two identical indexes occur in an expression, a summation over all three coordinates is implied, hence the scaler product between two vectors $\mathbf{u}$ and $\mathbf{v}$ is expressed as

$$u_i v_i = u_1 v_1 + u_2 v_2 + u_3 v_3 = \mathbf{u} \cdot \mathbf{v} \tag{5}$$

Consequently, the divergence of a vector $\mathbf{u}$ reads

$$\frac{\partial u_i}{\partial x_i} = \frac{\partial u_1}{\partial x_1} + \frac{\partial u_2}{\partial x_2} + \frac{\partial u_3}{\partial x_3} = \nabla \mathbf{u} \tag{6}$$

Appendix B: Timestepper GPU Implementation

The most straightforward approach to evaluate the matrix exponential for a given final time would be to evaluate equation (6.1) using time-stepping. It can be shown that the maximum energy growth at a given time is related to the largest eigenvalue of $\Psi^*(t)\Psi(t)$. In a time-stepping context, this is achieved by a forward marching in time using the linear operator J followed by a backwards in time integration using the adjoint J^* until convergence [126, 127]. For this purpose a timestepper running on Graphics Processing Units (GPUs) was developed and is presented next. Specifically, the algorithms and device functions shown below have been developed in Python and executed on the GPU using the Numba compiler. Numba is a just-in-time, type-specializing, function compiler for accelerating numerically-focused Python for either a CPU or GPU. It supports CUDA GPU programming by directly compiling a restricted subset of Python code into CUDA kernels and device functions following the CUDA execution model [188].

In order to carry out these computations, some basic algebraic operations developed to run on the GPU had to be defined. Frequently, when operating with large datasets, the number of data elements outnumbers that of threads on the GPU. To overcome this, a technique called grid striding is used to allow each thread to work on more than one data element. By using grid stride loops, kernels that can be easily switched between serial and parallel execution can be developed while incurring the benefits of global memory coalescing, which allows parallel threads to access memory in contiguous

chunks, a scenario which the GPU can leverage to reduce the total number of memory operations [189].

The operations implemented herein using grid striding are the sparse and dense matrix-vector product, matrix transpose and vector multiplication and addition. To demonstrate the main differences between striding for one and two-dimensional datasets, only the matrix vector products are shown in this section. The COO format, that explicitly stores both row and column index of every non-zero entry, is used in the sparse matrix-vector (SpMV) product in the code snippet shown in listing 1.

Listing 1. CUDA algorithm for SpMV on COO format

```
@cuda.jit
def spmv_coo_stride(rowidx, colidx, data, x, y):

  start = cuda.blockIdx.x*cuda.blockDim.x + cuda.threadIdx.x
  stride = cuda.blockDim.x*cuda.gridDim.x

  for i in range(start,data.shape[0],stride):
    cuda.atomic.add(y,rowidx[i],data[i]*x[colidx[i]])
```

Since the non-zero entries of the sparse matrix and the vector are one dimensional datasets, one grid stride loop is used. The `cuda.atomic.add` command is used for synchronised summation in order to avoid race conditions. The calculation in line 4 of listing 1 gives a unique thread index within the entire grid. In the case of the dense matrix-2D-vector product, essentially a matrix multiplication, striding is performed in two dimensions for the rows and columns respectively, with `cuda.grid(2)` used for the thread indexing of a two-dimensional grid. This is shown in listing 2 for matrices of arbitrary size denoted as `A,B`.

Listing 2. CUDA algorithm for 2D Dataset Multiplication

```
@cuda.jit
def mv_stride(A, B, C):

    grid_row, grid_column = cuda.grid(2)
    stride_row, stride_column = cuda.gridsize(2)

    for data_row in range(grid_row, A.shape[0], stride_row):
        for data_column in range(grid_column, B.shape[1], stride_column):
            sum = 0
            for i in range(A.shape[1]):
                sum += A[data_row][i] * B[i][data_column]

            C[data_row][data_column] = sum
```

At the inner most level, an algorithm responsible for the forward and backward integration is required. The Runge-Kutta Fehlberg (RKF) method was chosen for implementation. This method of order $O(h^5)$ uses five stage evaluations for one step with an additional stage that is used as an error estimator, of order $O(h^6)$ as shown in figure 1. Depending on the error, the next time-step is adjusted accordingly to allow for larger steps if it is small and finer steps if it is larger than a given tolerance [190]. For an initial value problem, such as equation (2.42), the numerical solution of the RKF has the form

$$\boldsymbol{q}_{n+1} = \boldsymbol{q}_n + h\sum_{i=1}^{S} b_i k_i \quad where \quad \boldsymbol{q}(t_n) = \boldsymbol{q}_n \tag{7}$$

where k_i is the RKF stage evaluation for a function f, defined as

$$k_1 = f(t, \boldsymbol{q}(t)) \tag{8}$$

$$k_i = f(t_n + c_i h, h\sum_{j=1}^{i-1} a_{i,j} k_j), \quad \text{i=2,3,4,5,6} \tag{9}$$

where n, h and S represent the iteration number, stepsize and number of stages respectively. The coefficients $a_{i,j}, b_i$ and c_i are arranged in a tableau known as the Butcher Tableau and are [191]

0						
$\frac{1}{4}$	$\frac{1}{4}$					
$\frac{3}{8}$	$\frac{3}{32}$	$\frac{9}{32}$				
$\frac{12}{13}$	$\frac{1932}{2197}$	$-\frac{7200}{2197}$	$\frac{7296}{2197}$			
1	$\frac{439}{216}$	-8	$\frac{3680}{513}$	$-\frac{845}{4104}$		
$\frac{1}{2}$	$-\frac{8}{27}$	-2	$-\frac{3544}{2565}$	$\frac{1859}{4104}$	$-\frac{11}{40}$	
	$\frac{16}{135}$	0	$\frac{6656}{12825}$	$\frac{28561}{56430}$	$-\frac{9}{50}$	$\frac{2}{55}$
	$\frac{1}{360}$	0	$-\frac{128}{4275}$	$-\frac{2197}{75240}$	$\frac{1}{50}$	$\frac{2}{55}$

Finally, the next stepsize at the end of each iteration is adapted considering the error according to the equation

$$h_{n+1} = 0.8\ h_n \left(\frac{tol}{\| TE \|} \right)^{\frac{1}{7}} \tag{10}$$

were tol is the user-defined tolerance and TE the truncation error.

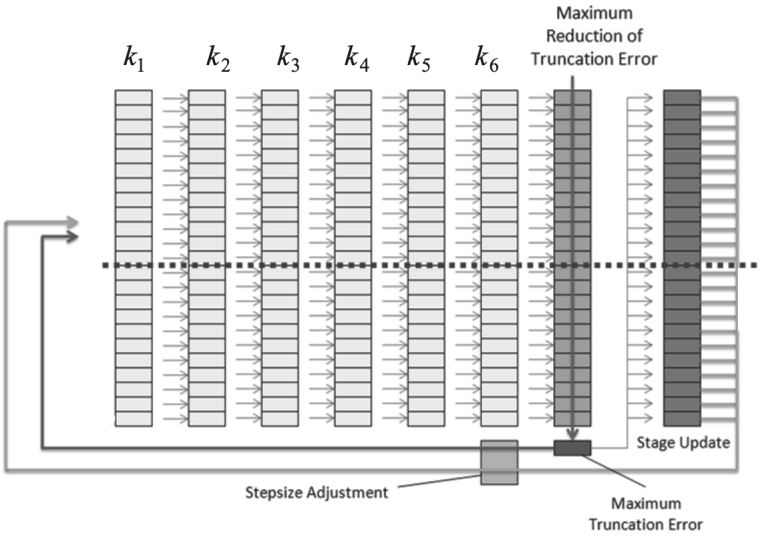

FIGURE 1. GPU Implementation of Runge-Kutta Methods taken from [16].

In order to optimise the RKF method for GPU use, the most computationally demanding calculations were singled out to be developed as device functions. RKF requires one function evaluation followed by a summation per stage and the final error calculation. In the case of equation (2.42) this translates to one sparse matrix-vector product (listing 1) per function evaluation. Lastly, by evaluating the function with the negative adjoint operator and a negative stepsize, backwards integration is achieved. To calculate the first k largest eigenvalues of the operator $\Psi^*(t)\Psi(t)$, the Arnoldi procedure, based on the modified Gram-Schmidt process with an iterative refinement technique suggested by Daniel, Gragg, Kaufman, and Stewart [192] (DGKS) to maintain orthogonality, is adapted from [193]. By replacing the matrix to be factorised with the operator $\Psi^*(t)\Psi(t)$, we construct a Krylov subspace of size $k \times N$ with the orthogonal projections of the action of $\Psi(t)$ followed by $\Psi^*(t)$. The points where calls to the GPU functions and the timestepper are made, are denoted in algorithm 1. Once the Hessenberg matrix H has been constructed, the eigenvalues of the significantly smaller system can by computed by direct methods.

Algorithm 1 Implementation of the Arnoldi iteration combined with the RKF timestepper

1: **procedure** ARNOLDI FACTORISATION RKF($A, k, v_0, t_0, t_{end}, h, tol$)
2: $v_0 \leftarrow v_0/\|v_0\|$ ▷ Normalise initial guess
3: $v_{end} \leftarrow \Psi(t)v_0$ ▷ Forward RKF
4: $v_{end} \leftarrow v_{end}/\langle v_{end}, v_{end}\rangle$
5: $v_0 \leftarrow -\Psi^*(t)v_{end}$ ▷ Backward RKF
6: $d \leftarrow v_{end}^T w$
7: $f \leftarrow v_0 - d \times v_0$
8: $V[:, 0] \leftarrow v_0[:, 0]$
9: $H[0, 0] \leftarrow f[0, 0]$ ▷ Update Hessenberg matrix
10: **for** $j \rightarrow k - 1$ **do**
11: $\beta(j) \leftarrow \|f\|$
12: $v_0 \leftarrow f/\beta(j)$
13: $V[:, j + 1] \leftarrow v_0[:, 0]$
14: $H[j + 1, j] \leftarrow \beta(j)$ ▷ Update Hessenberg matrix
15: $v_{end} \leftarrow \Psi(t)v_0$ ▷ Forward RKF
16: $v_{end} \leftarrow v_{end}/\langle v_{end}, v_{end}\rangle$
17: $v_0 \leftarrow -\Psi^*(t)v_{end}$ ▷ Backward RKF
18: $d \leftarrow V^T w$ ▷ Transpose then Dense Matrix Product
19: $f \leftarrow v_0 - V \times d$ ▷ Dense Matrix Product
20: **if** $\|f\| < \sqrt{0.5} \times \|d\|$ **then** ▷ DGKS correction
21: $s \leftarrow V^T f$ ▷ Dense Matrix Product
22: $f \leftarrow f - Vs$ ▷ Dense Matrix Product
23: $d \leftarrow d + s$
24: $H[: j + 2, j + 1] \leftarrow d[:, 0]$
25: **return** V, H